

---

# **Hybrid simulations of Titan's plasma interaction: Case studies of Cassini's T9, T63 and T96 flybys**

---

Inaugural-Dissertation  
zur  
Erlangung des Doktorgrades  
der Mathematisch-Naturwissenschaftlichen Fakultät  
der Universität zu Köln

vorgelegt von  
von Moritz Feyerabend  
aus Wedelheine

Köln, 2016

---

Berichtersteller: Prof. Dr. Sven Simon  
(Gutacher) Prof. Dr. Bülent Tezkan  
Tag der mündlichen Prüfung: 31.05.2016





# Summary

In this thesis, we apply numerical simulations by means of the hybrid code A.I.K.E.F. (Adaptive Ion-Kinetic Electron-Fluid) to study the interaction of Saturn's magnetospheric plasma as well as the solar wind with Titan's ionosphere. The composition of Titan's ionosphere is represented by a 7-species model. The ionosphere is generated by a realistic wavelength dependent photoionization model of the main neutral species  $N_2$ ,  $CH_4$  and  $H_2$ . We also included elastic ion-neutral collisions of the impinging plasma with Titan's neutral atmosphere to our model as well as a network of the most important chemical reactions of the ionosphere that converts between the ion species.

In the first part of the thesis we investigate the physical processes that lead to the detection of 'split signatures' in the ion densities during several crossings of the Cassini spacecraft through Titan's mid-range plasma tail (T9, T63, and T75). During each of these flybys, the Cassini Plasma Spectrometer observed Titan's ionospheric ion population twice; i.e., the spacecraft passed through two spatially separated regions where cold ions were detected. Our simulation results show that the filamentation of Titan's tail is a common feature of the moon's plasma interaction. The transport of ionospheric ions of all species from the ramside to the moon's wakeside generates a cone-like structure on the downstream side, that contains a region of reduced density. In addition, light (mass 1-2 amu) ionospheric species are driven radially outwards by pressure gradients in the ionosphere and escape along draped magnetic field lines, forming a parabolically shaped filament structure which is mainly seen in planes that contain the upstream magnetospheric magnetic field and the upstream flow direction. Our results imply that the detections of split signatures during T9, T63 and T75 are consistent by Cassini penetrating through parts of these filament structures.

In the second part of the thesis we study Titan's plasma interaction with the solar wind during the Cassini T96 flyby. The T96 encounter marks the only observed event of the entire Cassini mission where Titan was located in the supersonic solar wind in front of Saturn's bow shock. We show that the large-scale features of Titan's induced magnetosphere during T96 can be described in terms of a steady-state interaction with a high-pressure solar wind flow. About 40 minutes before the encounter, Cassini observed a rotation of the incident solar wind magnetic field by almost 90 degrees. We provide strong evidence that this rotation left a bundle of fossilized magnetic field lines in Titan's ionosphere that was subsequently detected by the spacecraft.



# Zusammenfassung

In dieser Arbeit benutzen wir numerische Simulationen auf Basis des Hybrid Codes A.I.K.E.F. (Adaptive Ion-Kinetic Electron-Fluid), um die Plasma Wechselwirkung von Titans Ionosphäre mit Saturns magnetosphärischem Plasma als auch dem Sonnenwind zu untersuchen. Die Zusammensetzung von Titans Ionosphäre wird durch ein Modell mit 7 Spezies repräsentiert. Die Ionosphäre wird durch ein realistisches, wellenlängenabhängiges Photoionisationsmodell der neutralen Hauptspezies  $N_2$ ,  $CH_4$  und  $H_2$  generiert. Desweiteren haben wir elastische Ionen-Neutral Kollisionen des anströmenden Plasmas mit Titans Neutralatmosphäre zu unserem Modell hinzugefügt sowie ein Netzwerk der wichtigsten chemischen Reaktionen der Ionosphäre welches für die Umwandlung der Spezies untereinander sorgt.

Im ersten Teil dieser Arbeit untersuchen wir die physikalischen Prozesse die zur Beobachtung sogenannter 'split signatures' in den Ionendichten von mehreren Vorbeiflügen (T9, T63, T75) der Cassini Sonde durch Titans mittel-entfernten Magnetosphärenschweif führten. Während jedem dieser Vorbeiflüge registrierte das Cassini Plasma Spektrometer Titans Ionenpopulation zwei mal: i.e., das Raumfahrzeug passierte zwei räumlich getrennte Regionen in denen kalte Ionen beobachtet wurden. Unsere Simulationsergebnisse zeigen, dass die Filamentierung von Titans Magnetosphärenschweif eine allgemeine Eigenschaft von Titans Plasmawechselwirkung ist. Der Transport von ionosphärischen Ionen aller Spezies von der Anströmseite zur stromabgewandten Seite erschafft eine zylinderartige Struktur stromabwärts, die eine Region reduzierter Dichte umschliesst. Ausserdem werden leichte Ionen in der Ionosphäre (Masse 1-2 amu) durch Druckgradienten radial auswärts gerichtet beschleunigt und bewegen sich dann entlang drapierter Magnetfeldlinien. Dies führt zur Ausbildung von parabolisch geformten Filamenten, welche hauptsächlich in Ebenen gesehen werden können die den Magnetfeldvektor und die Richtung des Anströmplasmas enthalten.

Im zweiten Teil der Arbeit untersuchen wir Titans Plasmawechselwirkung mit dem Sonnenwind während des T96 Vorbeifluges von Cassini. Die T96 Begegnung stellt den einzigen Zeitpunkt der gesamten Cassini Mission dar, in dem Titan im überschall schnellen Sonnenwind vor Saturns Bugstossstelle eingebettet war. Wir zeigen, dass die grossskaligen Eigenschaften von Titans induzierter Magnetosphäre während T96 konsistent sind mit dem Bild einer quasi-stationären Wechselwirkung Titans mit einem Sonnenwind der einen hohen dynamischen Druck hat. Ungefähr 40 Minuten vor seinem Vorbeiflug detektierte Cassini dabei eine Rotation des anströmenden Sonnenwindmagnetfeldes um fast 90 Grad. Wir liefern starke Hinweise, dass diese Rotation ein Bündel von fossilisierten Magnetfeldlinien in Titans Ionosphäre hinterlassen hat, welche in der Folge von der Sonde beobachtet wurden.



# Contents

<b>Summary</b>	<b>v</b>
<b>Zusammenfassung</b>	<b>vii</b>
<b>1 Introduction</b>	<b>1</b>
<b>2 Titan's Plasma Environment</b>	<b>7</b>
2.1 Saturn's Magnetospheric Structure . . . . .	7
2.1.1 Coordinate System . . . . .	11
2.1.2 Dynamics of the Magnetodisk . . . . .	12
2.2 Titan's Atmosphere . . . . .	21
2.3 Titan's Plasma Interaction . . . . .	23
2.4 Fossilized Magnetic Fields at Titan . . . . .	28
<b>3 Simulation Model</b>	<b>33</b>
3.1 Hybrid Model A.I.K.E.F. . . . .	33
3.2 Numerical Implementation . . . . .	36
3.3 Titan ionosphere model . . . . .	38
3.4 Other Titan simulation models . . . . .	42
<b>4 Split Signatures in Titan's tail</b>	<b>45</b>
4.1 Introduction . . . . .	45
4.2 Simulation Setup and Numerical Parameters . . . . .	49
4.3 Run #1: Voyager-type upstream conditions . . . . .	52
4.3.1 Run #1: Collisions and $\nabla P_e$ removed . . . . .	54
4.4 Run #2: T9-type upstream conditions . . . . .	56
4.5 Run #3: T63-type upstream conditions . . . . .	62
4.5.1 T75 split signatures . . . . .	63
4.6 Summary . . . . .	64
<b>5 Titan in the Supersonic Solar Wind</b>	<b>67</b>
5.1 Introduction . . . . .	67
5.2 Simulation Parameters . . . . .	72
5.3 Model Results and Discussion . . . . .	75
5.4 Concluding Remarks . . . . .	80

<b>6 Summary and Outlook</b>	<b>81</b>
6.1 Outlook . . . . .	83
<b>Bibliography</b>	<b>85</b>
<b>Acknowledgements</b>	<b>97</b>
<b>Erklärung</b>	<b>99</b>

# 1 Introduction

Saturn's moon Titan has been in the spotlight of scientific interest ever since its discovery by Christiaan Huygens in 1655. One of the reasons for that lies in its thick neutral atmosphere, the presence of which has been known from earthbound spectral observations since the early 1940s. The flybys of Pioneer 1 and Voyager 1 in the late 1970s and early 1980s further sparked the interest in the moon, as they confirmed that Titan's atmosphere is mainly composed of nitrogen. Titan is the only other body in the Solar system except Earth, that has a nitrogen-based atmosphere. It is also the second-largest moon (after Ganymede) in the entire Solar system with a radius of  $R_T=2575$  km, which puts it even before Mercury regarding the size. The exploration of Titan has been declared one of the major scientific aims of the NASA/ESA Cassini mission that was launched in 1997. Since its arrival in the Saturnian system on 01 July 2004, the Cassini spacecraft has performed

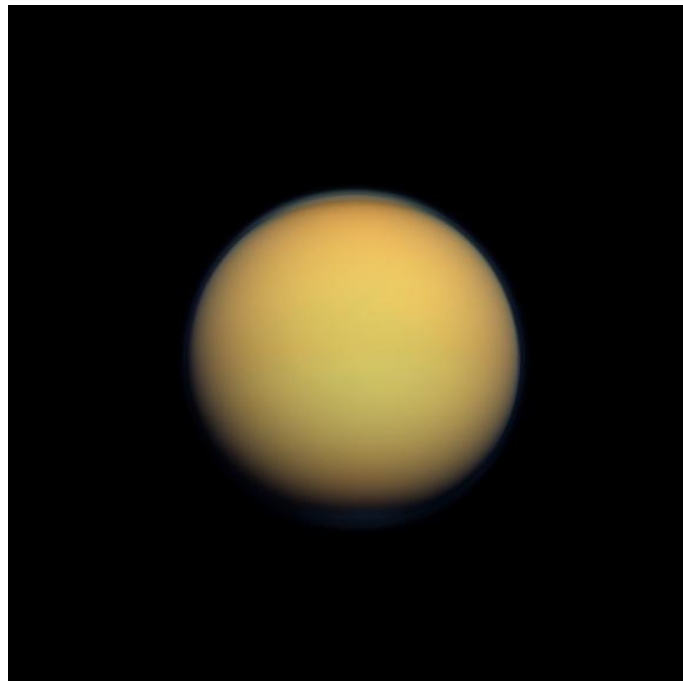


**Figure 1.1:** Natural color view on Titan from a distance of 191000 km. The picture was taken by Cassini's Imaging Science Subsystem (ISS) on 30 January, 2012. A thick haze layer of organic compounds in the lower atmosphere gives Titan a yellow-orange color. Credit: NASA webpage.

117 visits to Titan at the time of writing<sup>1</sup>. One of the prime moments of the Cassini mission was the landing of the Huygens landing probe, that provided in-situ measurements of Titan's atmosphere during its decent on 14 January 2005. Titan therefore states the most distant celestial body where a human-made object has landed. A summary of Titan's main physical and orbital parameters is provided in table 1.1.

The data gathered by Cassini has revealed that Titan's atmosphere is the host of a very complex chemistry network which is fueled by nitrogen and methane. The organic compounds that are created by this chemistry network are found in a very broad mass range from 1 to  $\sim 10000$  amu all over Titan's atmosphere. At low altitudes, the heaviest species are found as aerosols that form a thick haze layer which gives Titan its characteristic yellow-orange appearance (see figure 1.1). Titan's surface is covered with a crust of frozen water ice and lakes of liquid methane that condensates as a result of the atmospheric climate processes. Solar radiation and energetic particles create ionize the neutral atmosphere at high altitudes, which leads to the formation of an extended ionosphere around the moon. Titan is therefore very similar in its atmospheric structure to Earth.

Parameter	Value
Radius ( $R_T$ )	2575 km
Mass	$1.345 \cdot 10^{23}$ kg
Mean density	$1.88 \text{ g/cm}^3$
Surface temperature	94 K (-179°C)
Surface pressure	1.44 bar
Surface gravity	$1.35 \text{ m/s}^2$
Escape velocity	2.65 km/s
Semi-major axis	122.18 million km (=20.3 $R_S$ )
Orbital period	15.945 days
Spin period	15.945 days (synchronous)
Orbital velocity	5.57 km/s

**Table 1.1:** Main physical and orbital parameters of Saturn's largest moon, Titan.

While Titan's atmospheric and surface processes are already scientifically very interesting, the plasma interaction between Titan and Saturn's magnetospheric plasma has also been a major topic of the Cassini mission. Since the moon's orbital velocity is much smaller than the ambient plasma flow, Titan gets constantly overtaken by Saturn's magnetospheric plasma. Similar to Mars and Venus, Titan does not possess a noticeable intrinsic or induction-generated magnetic field (Wei et al. 2010) so that the moon's atmosphere and ionosphere acts as an obstacle to the impinging plasma flow. As a result, the magnetic field lines drape around the moon's ionosphere which leads to the formation of a characteristic perturbation pattern of the magnetic field and plasma flow on the ram side and downstream of the moon (called induced magnetosphere). However, Titan's plasma interaction is unique among that of other non-magnetized bodies in the solar system due to its highly variable plasma environment. Over ten years of observations from Cassini have established the picture of a highly dynamic structure of Saturn's magnetosphere (see figure 1.2) that is defined by the influences of the solar wind and its internal rotation. The

---

<sup>1</sup>The T118 flyby is scheduled for 04 April 2016

mass loading of Saturn's magnetosphere with particles originating from Enceladus water plumes leads to the formation of a sub-corotating equatorial plasma sheet that distorts Saturn's dipolar magnetic field structure over the scale of the magnetosphere. In addition, the plasma sheet has been observed to show an oscillatory vertical motion. As a result, the local plasma and magnetic environment of the magnetosphere changes as a function of the distance to the equatorial plasma sheet. Titan orbits around Saturn at a distance of about 20.3 Saturn radii, which puts it in the outer regions of Saturn's magnetosphere. In this region the dynamical effects and the distorted structure of Saturn's magnetosphere are most pronounced. If the solar wind dynamic pressure is large enough it is even possible that Titan is located in Saturn's magnetosheath region or outside of Saturn's magnetosphere in the solar wind. Titan is therefore extremely susceptible to changes in its ambient plasma environments at its location which in turn is reflected by Titan's plasma interaction with the ambient magnetosphere.

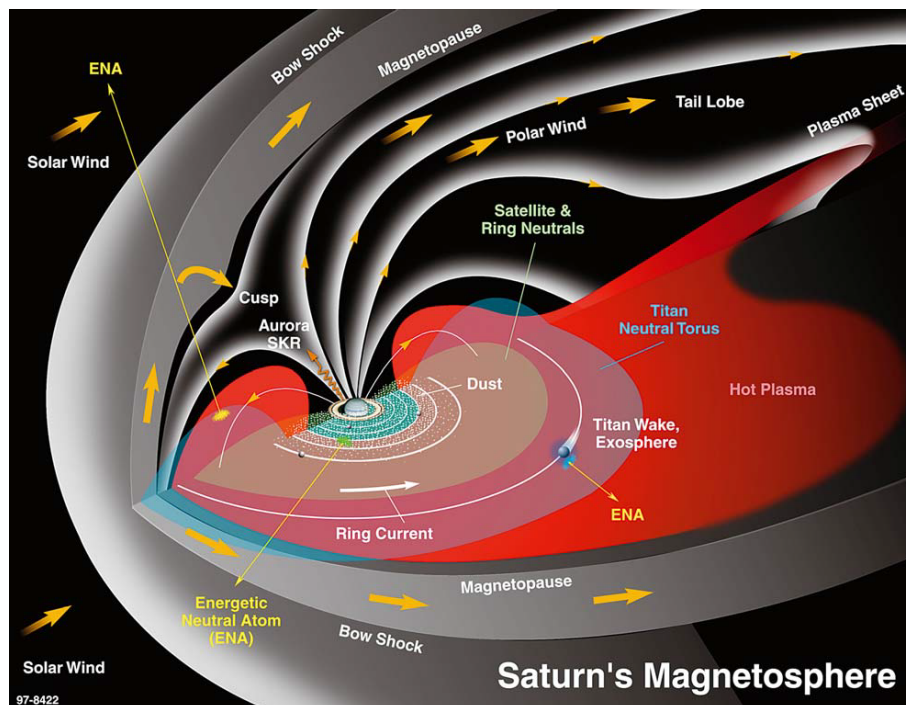


**Figure 1.2:** Schematic of the large scale structure of Saturn's magnetosphere in the solar wind. Figure from Krimigis et al. (2004).

At the nearing end of the Cassini mission in 2017, culminating into the controlled descent of the spacecraft into Saturn's upper atmosphere during its final phase, a tremendous amount of research has been devoted and published towards many aspects of Titan's surface, atmosphere, ionosphere, chemistry and plasma interaction. The general structure of Titan's plasma interaction under the variable nature of its plasma environment is known to the most part and many numerical models have been developed that verified this knowledge by reproducing observational data with computer simulation.

In this study we therefore focus on some of the unique observations and flybys made by Cassini that have not yet been explained at all or in a satisfactory manner. In particular we focus on the T9, T63, T75 and T96 Titan flybys of Cassini, which were all exceptional

in a certain way. The T9, T63 and T75 flybys were encounters where Cassini crossed at a great distance through Titan's downstream magnetotail region. A remarkable observation that was only made during these encounters was the detection of a 'split' tail: a spatially separated double observation of a cold ion population that originated from Titan's ionosphere. Our goal in this thesis is to get a better understanding of the physical processes that lead to the detection of these 'split signatures' and whether or not this is an omnipresent feature of Titan's plasma interaction that might have been missed during other flybys.

The T96 flyby is a truly unique encounter as it constitutes the only time of the entire Cassini era where Titan was embedded in the supersonic solar wind in front of Saturn's bow shock during a time of extreme solar wind dynamic pressure. This encounter has not yet been subject to any modeling attempt so far. We examine if the large-scale observations of Titan's induced magnetosphere can be described in terms of a steady state interaction with the high pressure solar wind. Since the dynamic pressure of the solar wind is loaded with some uncertainty for this encounter, we use it as a free parameter to find a setting that produces numerical results which are in agreement with magnetic field and electron density measurements. In addition we investigate the effects of the variable magnetic environment on Titan's magnetic signature during this encounter. We also analyze the contribution of fossilized magnetic field lines from an upstream magnetic regime prior to the encounter to the small scale magnetic pattern inside Titan's ionosphere. Fossilized magnetic field lines can be understood as the imprint of a varying upstream magnetic configuration on Titan's ionosphere, in some analogy to the growth-rings of trees.

To address these problems we perform numerical simulations of Titan's plasma interaction using a hybrid model. A hybrid model treats ions as kinetic particles and electrons acts as a massless charge neutralizing fluid. The hybrid approach is able to resolve effects that arise due to the gyrating motion of ions in a magnetized plasma flow. At Titan these effects cannot be neglected since the local gyro radius is always at least comparable to the moons radius, which leads to a noticeable asymmetrization of its induced magnetosphere. Fluid models that treat ions as a fluid as well are therefore limited in their ability to correctly represent the relevant physics near Titan. The model of Titan's ionosphere that is used in this thesis has been significantly improved compared to previous studies (Simon et al. 2006b). We have included a realistic model of the photoionization of Titan's neutral atmosphere and represent the relevant ion species of Titan's ionosphere with a 7-species model that also includes elastic collisions and the most important chemical reactions.

This thesis is structured as follows: in chapter 2 we give the theoretical background that is needed to understand the complex nature of Titan's interaction with the highly variable plasma environment of Saturn's magnetosphere. We continue with a brief description of the hybrid code A.I.K.E.F. (**A**daptive-**I**on-**K**inetic-**E**lectron-**F**luid) and the representation of Titan's ionosphere and chemistry network in chapter 3. Our results are presented in chapter 4 and 5:

- In chapter 4 we use our model to study the fine structure of the density distribution in Titan's downstream magnetotail region. We study the ion transport mechanisms that lead to the formation of this fine structure as well as the spatial restrictions that are placed on them by the relative orientation of the upstream flow direction and background magnetic field. We use our findings to compare hybrid model results of the T9 and T63 flyby against density measurements obtained by Cassini and give

reasons for the unexpected spatially separated detection of cold ionospheric ions during those encounters.

- Chapter 5 focuses on Titan's interaction with the supersonic solar wind during Cassini's unique T96 flyby. We investigate the impact of the variable solar wind environment on Titan's induced magnetosphere structure as well as the contribution of fossilized magnetic fields to the magnetic observations around closest approach of the spacecraft.

Finally, we summarize the major findings of this thesis and give a brief outlook on future projects in chapter 6.



## 2 Titan's Plasma Environment

In this chapter we give the theoretical background and current knowledge of Titan's plasma environment and its interaction with Saturn's magnetospheric plasma. The general structure and dynamic behavior of Saturn's outer magnetosphere near Titan is described in section 2.1. In section 2.2 we describe the unique features of Titan's atmosphere and its rich nitrogen fueled chemistry. Finally we explain the general aspects of Titan's plasma interaction in section 2.3 and give further insight into the phenomenon of fossilized magnetic fields in Titan's ionosphere in section 2.4.

### 2.1 Saturn's Magnetospheric Structure

Saturn's magnetosphere is generated by its intrinsic dipolar magnetic field. A peculiarity of Saturn's dipole moment compared to other planets is that it is almost perfectly aligned with the planet's rotation axis with a tilt of less than  $0.1^\circ$  and an offset of  $0.036 R_S$  (Burton et al. 2010). The planet's magnetic field has a surface strength of 21136 nT (Burton et al. 2010). Saturn's magnetosphere is filled with neutral particles that emanate from the planet itself, its icy moons (e.g. Enceladus, Rhea, Dione) and the ring system via sputtering and atmospheric losses (Arridge et al. 2011c). The neutral particles then become ionized through photoionization, electron impact and charge exchange processes. Overall, Saturn's magnetosphere is dominated by neutral particles, which have been found to outnumber ions by a factor of 10-100 (Arridge et al. 2011). The major source of particles in the magnetosphere are the water plumes of Saturn's moon Enceladus (Hansen et al. 2006). The dominant ion species in Saturn's magnetospheric plasma thus consists of water group ions ( $O^+$ ,  $OH^+$ ,  $H_2O^+$ ,  $H_3O^+$ ) and protons  $H^+$ .

Enceladus is located in the inner magnetosphere at a distance of 3.95 Saturn radii (equatorial radius  $R_S = 60.268$  km). This has severe consequences on the general structure of Saturn's magnetosphere. The magnetospheric plasma corotates with the planet and contains the frozen-in magnetic field. Ions that are inserted into the system near Enceladus move at least with the speed of Enceladus orbital velocity, which is 12.6 km/s and slower than the corotational velocity of  $\sim 26$  km/s. The ions are then accelerated by the convective electric field until their guiding center reaches nearly corotational velocity (also known as 'pick-up' process). However, the distance at which the centrifugal forces acting on the corotating plasma and Saturn's gravitational force cancel each other lies at a distance much lower than Enceladus orbit. Therefore, the plasma that is generated by the plumes of Enceladus is driven radially outward from Saturn due to the outwards pointing centrifugal force and the arising plasma pressure gradients. This outwards pointing plasma flow leads to a large scale deformation of the magnetic field in the outer region of

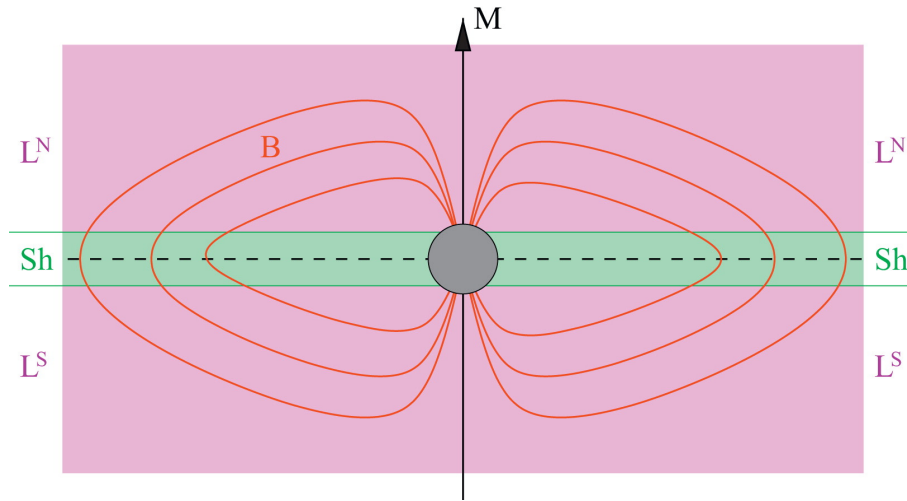


**Figure 2.1:** Side-on view of Saturn's magnetodisk structure. The figure illustrates Saturn's (grey circle) magnetic field configuration (red lines) when the observer-Saturn line is perpendicular to Saturn's magnetic moment  $\underline{M}$ . In the northern (labeled  $L^N$ ) and southern (labeled  $L^S$ ) magnetic lobes the field lines are highly stretched and possess strong radial components. In the narrow current sheet region of the magnetodisk around the magnetic equator (labeled Sh, green area), the magnetic field is still quasi-dipolar and nearly antiparallel to Saturn's rotation axis. Titan's orbit in this idealized picture is indicated by the dashed black line. Figure from Simon et al. (2010).

Saturn's magnetosphere. The azimuthal current system that is associated with the corotating plasma stretches Saturn's magnetic field from a dipolar shape to a deformed shape that is characterized by highly stretched magnetic field lines above and below the magnetic equator. This structure of the magnetosphere is referred to as the 'magnetodisk' (Arridge et al. 2007) of Saturn's magnetosphere. The extent of the magnetodisk is balanced by the inwards pointing  $\underline{j} \times \underline{B}$  forces exerted on the azimuthal currents of the corotating plasma. The azimuthal currents become stronger with increasing distance to the planet, due to the increasing azimuthal velocity of the corotating plasma. The general structure of Saturn's magnetosphere can be separated into three main parts: a dipolar field region in the inner magnetosphere until  $5 R_S$ , a quasi-dipolar field region with a weak current sheet in the middle magnetosphere from about 5 to 12-15  $R_S$ , and finally the disk-like region with highly stretched field lines and a strong current sheet in the outer part of the magnetosphere (Arridge et al. 2007).

A sketch of the magnetodisk structure is provided in figure 2.1. In the northern magnetic lobe, the magnetic field is mainly pointing radially away from Saturn, whereas in the southern lobe the field is oriented mainly towards the planet. The degree of how much the field lines are stretched towards/away from the planet can be calculated by means of the *stretch angle*

$$\text{Str} = \arctan\left(\frac{B_y}{B_z}\right) \quad , \quad (2.1)$$

where  $B_y$  and  $B_z$  are the magnetic field components in TIIS coordinates (see section 2.1.1). A positive stretch angle is therefore an indication of a location in the northern magnetic lobe, while a negative stretch angle indicates a position in the southern magnetic lobe.

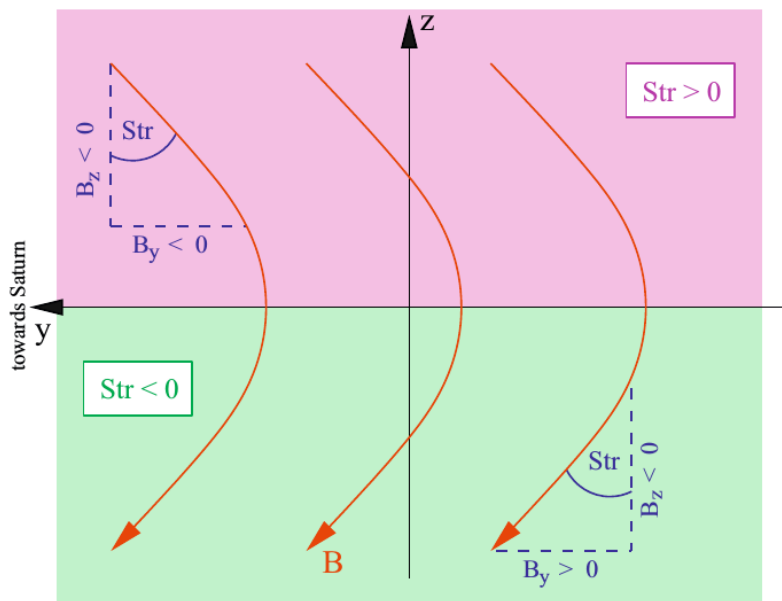


**Figure 2.2:** Illustration of the stretch angle. The figure shows Saturn's stretched magnetic field lines of the magnetodisk in a meridional plane (=  $yz$ -plane of the TIS system). The  $y$  axis points towards Saturn and the  $z$  axis is parallel to Saturn's magnetic moment. The  $B_y$  component of the magnetic field is negative above the magnetic equator and positive below the magnetic equator. Therefore the stretch angle  $\text{Str} = \arctan(-B_y/B_z)$  is positive for locations in the northern magnetodisk lobe and negative for locations in the southern magnetodisk lobe. At the magnetic equator where  $B_y = 0$ , the stretch angle vanishes. Figure from Simon et al. (2010)

Figure 2.2 illustrates the stretch angle in case the current sheet coincides with the magnetic equator. The value of the stretch angle provides a measure of how much the field lines are stretched at an observers position. A high stretch angle value is therefore an indication of a great distance to the magnetodisk's current sheet.

The magnetodisk is not only characterized by the highly stretched field lines in the lobes, it also shows a deformation of the field lines in the corotational direction. The equatorial current sheet is strongly coupled to Saturn's ionosphere via field aligned Birkeland currents (magnetosphere-ionosphere coupling, Hill (1979)). These currents transfer angular momentum from Saturn's ionosphere into the current sheet in order to accelerate the plasma to corotational speeds. However, this process is limited by the finite Petersen conductance of Saturn's ionosphere. Therefore the magnetosphere-ionosphere coupling cannot provide the necessary angular momentum that is needed to enforce a rigid corotation of the magnetospheric plasma throughout the whole of the magnetosphere. Instead, strict corotation of the plasma is found only in the inner magnetosphere. With increasing distance from Saturn, the plasma is found to subcorotate at about 50-80% of the ideal corotation speed (Thomsen et al. 2010). In the outer magnetosphere ( $> 15 R_S$ ) a saturation is reached, where the azimuthal velocity of the plasma remains nearly constant (Arridge et al. 2011c). At the orbital distance of Titan, the full corotational speed would be  $\sim 200$  km/s, however the average plasma speed is found to be in the range of 120 – 160 km/s (e.g Wilson et al. (2010)). Frozen-in field lines in the equatorial current sheet are

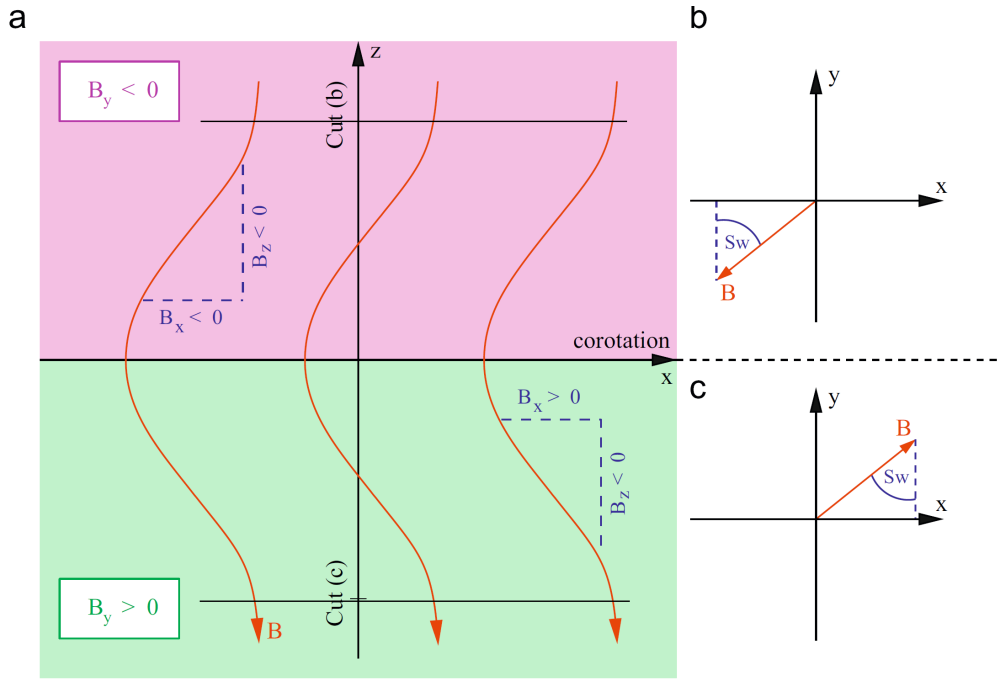


**Figure 2.3:** Illustration of the sweepback angle. The figure shows how Saturn's magnetic field lines are bent back with respect to a strictly corotating meridional plane as a result of the corotational lag in Saturn's magnetodisk current sheet. Plot (a) shows the  $xz$ -plane of the THS system, plot (b) shows a  $xy$ -cut above ( $z > 0$ ) and plot (c) a  $xy$ -cut below Titan's orbital plane. When the magnetic field lines are bent back with respect to a  $x = \text{const}$  plane, the sweepback angle  $Sw = \arctan(-B_x/B_y)$  is negative both above and below the magnetic equator. Figure from Simon et al. (2010).

therefore bent back with respect to a strictly corotating meridional plane (see figure 2.3). The magnitude of this sweepback can be measured with the *sweepback angle*

$$Sw = \arctan\left(\frac{-B_x}{B_y}\right) . \quad (2.2)$$

With this definition, the sweepback angle is negative for swept back magnetic field lines for locations both north and south of the magnetic equator. Consequently, for a scenario of swept forwards field lines that indicate a super corotational plasma flow, the sweep angle would be positive. Observations of positive sweep angles have been occasionally observed near the dusk flank of Saturn's magnetosphere (Bertucci 2009).

Particles at high latitudes experience a gravitational pull towards the equatorial region, where, balanced by the centrifugal force, they are then confined to the plasma sheet. The thickness of the plasma sheet is on the order of 1-2  $R_S$  (Arridge et al. 2011a), with the heavy ions having a smaller scale height than light ions (Thomsen et al. 2010) due to the different masses. Therefore, light ions (protons, hydrogen) are found to dominate the plasma composition in the regions of Saturn's magnetic lobes whereas heavy ions (water group) will dominate in the equatorial current sheet. The plasma beta  $\beta = 2\mu_0 nkT/B^2$ , which is the ratio between thermal pressure and magnetic pressure, shows a similar behavior with a high beta value in the plasma sheet, and a lower beta value in the magnetodisk

lobes (Achilleos et al. 2014).

In combination with the magnetic structure of Saturn's magnetosphere, two main plasma regimes can be distinguished (Arridge et al. 2007): (a) a current sheet regime which is characterized by a dense, high beta plasma composition and a quasi-dipolar magnetic field configuration and (b), a lobe-type regime consisting of a more dilute low-beta plasma with stretched and swept-back magnetic field lines.

### 2.1.1 Coordinate System

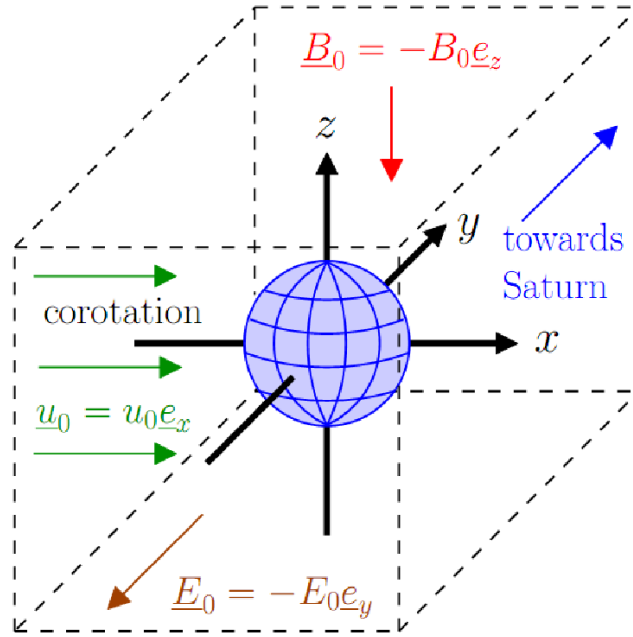


**Figure 2.4:** Illustration of the Titan Interaction System (TIIS) used in this thesis. Also displayed are the orientations of the main upstream plasma parameters  $\underline{E}_0$ ,  $\underline{B}_0$  and  $\underline{U}_0$  for idealized upstream conditions.

To be able to perform numerical simulations of Titan's plasma interaction, a suitable coordinate system that covers the simulation domain is needed. The rotating rest frame of the moon on its orbit around Saturn constitutes a natural choice of coordinates that are best suited to exploit the geometry of the plasma interaction. In the case of Titan, this magnetosphere-moon-interaction system is called the Titan Interaction System (TIIS). In the TIIS system, the  $x$  axis points in the direction of nominal corotation, which is identical to the direction of Titan's orbital motion around Saturn. The  $y$  axis of the coordinate system is pointing towards the center of Saturn, and the  $z$  axis is anti-parallel to Saturn's rotational axis. The origin coincides with the center of Titan. The coordinate system is sketched in figure 2.4, where we assume idealized upstream conditions, i.e., the magnetic field  $\underline{B}_0$  is aligned with the  $-z$  axis, the upstream flow direction is aligned with the  $x$  axis and the convective electric field  $\underline{E}_0 = -\underline{U}_0 \times \underline{B}_0$  points in the  $-y$  direction. However, for the majority of Cassini Titan flybys these parameters were found to not fit this picture of ideal plasma conditions very well, as we will see in section 2.1.2.

Another frame of reference that is frequently used to describe Saturn's magnetosphere is the cylindrical polar Kronocentric Solar Magnetic (KSMAG) coordinate system  $(\rho, \phi, z)$ . In this system the radial unit vector  $\underline{e}_\rho$  is pointing away from Saturn's rotational axis, the azimuthal unit vector  $\underline{e}_\phi$  is pointing eastwards in the corotational direction and the vertical unit vector  $\underline{e}_z$  is aligned with the planets rotational axis. Note that the only difference of this system to TIIS coordinates is a minus sign in the radial ( $y$  in TIIS) coordinate.

Another important set of parameters are the Saturn Local Time (SLT) and Subsolar Latitude (SSL) at the time of an encounter. These parameters define the exact location of the subsolar point in the TIIS system and therefore control the position and orientation of the ionosphere which is mostly generated through photoionization processes. They depend on Titan's orbital status and the Saturnian season. An illustration of the parameters is given in figure 2.5. The SLT can assume values from 0 to 24 as Titan orbits around Saturn. If Titan is at 6 or 18 SLT, the ramside of the impinging magnetospheric plasma coincides with the nightside (6 SLT) or the dayside (18 SLT) of Titan's photogenerated ionosphere. Due to the tilt of Saturn's rotational axis with respect to the ecliptic, and therefore Titan's orbit as well, the SSL varies from  $-26.7^\circ$  to  $26.7^\circ$  depending on the Saturnian season.

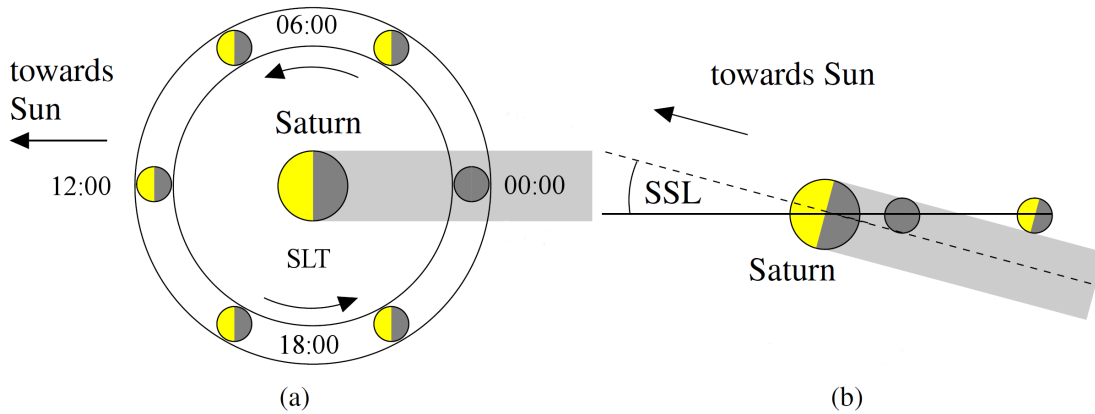


**Figure 2.5:** Illustration of (a) Titan's Saturn Local Time (SLT) and (b) Subsolar Latitude (SSL). The SLT denotes the orbital positions of Titan with respect to the sun. Due to the tilt of Saturn's rotational axis, the subsolar point changes with the seasons.

### 2.1.2 Dynamics of the Magnetodisk

Given that Titan's orbit lies within Saturn's equatorial region, one might expect to observe current-sheet like plasma conditions at Titan at all times. However this was found to be the case only on average. During many Cassini flybys, Titan was actually found to be embedded in the plasma environment of the magnetodisk lobes. The reason for this is that Saturn's magnetodisk is not a stationary system, but rather shows dynamic behavior on various timescales ranging from minutes to several years. These dynamics are induced by either internal processes of the Saturnian magnetosphere or other external factors, mainly the solar wind as well as the Saturnian seasons, and will be described in the following. The first external process that influences the shape of Saturn's magnetosphere is related to the solar wind pressure and manifests in a day-night asymmetry of the magnetodisk struc-

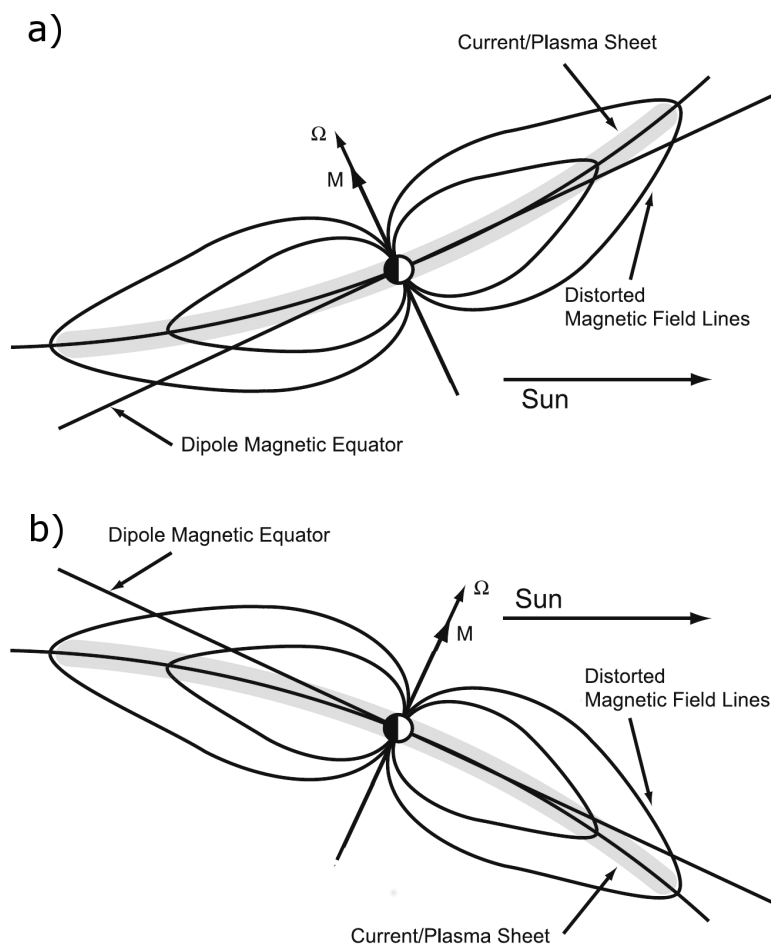


**Figure 2.6:** Sketch of the distortion of Saturn's magnetosphere along the noon-midnight meridian during **a)** southern and **b)** northern summer. As a result of the solar wind pressing against the magnetodisk's current sheet from either below or above, the magnetodisk adopts a bowl-like shape. Figure taken from Arridge et al. (2008a)

ture: The impinging solar wind naturally tries to compress the dayside magnetosphere, counteracting the formation of the magnetodisk in the near-noon local time sectors. If the solar wind dynamic pressure is sufficiently high, the stand-off distance of Saturn's magnetopause (where Saturn's magnetic pressure is balanced by the solar wind dynamic pressure) is close enough so that the magnetopause currents effectively suppress the formation of the magnetodisk. Instead a quasi-dipolar field configuration in the near noon time sectors is enforced, as opposed to the nightside and around dusk and dawn sectors, where the magnetodisk structure is not prevented at all. Arridge et al. (2008b) showed that the dayside formation of the magnetodisk can only prevail in times of low solar wind dynamic pressure, where the stand-off distance of the magnetopause is at  $23R_S$  or larger. Since the solar wind dynamic pressure variations do not follow predictable processes, the timescale of the magnetodisk's day-night asymmetry cannot be constrained with by fixed value and may change on a day-to-day basis.

The solar wind has a second impact on the magnetodisk's structure which is also related

to the tilt of Saturn's rotational ( $\approx$  magnetic) axis, and therefore to the Saturnian seasons. Due to this tilt, the solar wind impinges at an angle of up to  $26.7^\circ$  (during the solstices) onto Saturn's magnetic equator plane from either 'above' or 'below'. This leads to a deformation of the outer magnetodisk region into a basin- or bowl-like form (Arridge et al. 2008a), with the magnetic equatorial plane (where the radial magnetic field component  $B_r$  changes sign) being displaced against the rotational equatorial plane. On average, Titan is therefore embedded in the region of the southern magnetodisk lobe during Saturn's southern summer and in the northern magnetodisk lobe during Saturn's northern summer. An illustration of the magnetobowl shape for the two seasons is shown in figure 2.6. Around the equinoxes, this effect is much less pronounced, as the impacting angle of the solar wind with respect to the magnetic equatorial plane is close to zero during this time.

Even though Saturn's magnetic moment and rotational axis are almost perfectly aligned, a number of oscillatory phenomena in the magnetic field and other plasma parameters acting on timescales near the planet's rotation period of  $\sim 10.7$  h have been observed in Saturn's magnetosphere (e.g. Kurth et al. (2008), Khurana et al. (2009), Andrews et al. (2010)). Near Titan, these periodicities are observed as a north-south oscillatory motion of the magnetodisk's current sheet over the moon's orbital plane, which is also referred to as the 'flapping' of the magnetodisk (Arridge et al. 2008, Arridge et al. 2011b). Effectively this means that the plasma and magnetic conditions near Titan can show transitions between the magnetospheric environments of the northern and southern magnetodisk lobe as well as the magnetodisk current sheet on a timescale of  $\sim 10$  h. The reason for these oscillatory behavior of Saturn's magnetosphere is still one of the major open question that has not yet been explained in a satisfactory way (e.g. Andrews et al. (2012), Southwood and Cowley (2014)).

An exemplary observation of a full cycle of such a current sheet sweep across Titan's orbital position is given in figure 2.7, showing the magnetic field data obtained by the Cassini spacecraft during the T54 encounter on May 5, 2009 along with a sketch of magnetodisk's flapping motion at that time. During this encounter, the current sheet moved at least two times over Cassini's position, accompanied each time with a transition of the magnetic environment from one lobe regime to the other. The intervals where Cassini is embedded in the magnetodisk lobe regions are about 5 h long, roughly half of the planetary rotation period. They are clearly identified by their characteristic magnetic signatures:  $B_y > 0$  in the southern magnetodisk lobe,  $B_y < 0$  in the northern lobe. Also the sweepback of the magnetic field is visible in the  $B_x$  component in those intervals:  $B_x > 0$  in the southern lobe,  $B_x < 0$  in the northern lobe, see also figure 2.3. One of the current sheet sweeps is nearly coincident with Cassini's closest approach to Titan. This illustrates that these types of internally induced dynamics of the magnetodisk are quite significant for the understanding of Titan's plasma interaction, since they can disturb the upstream plasma and magnetic conditions on the timescale of a Cassini flyby.

The magnetic field observations depicted in figure 2.7 also show the last dynamic process of the magnetodisk current sheet, which is also associated with the flapping motion mentioned above. As can be seen in the time interval from 02:00-04:00 in figure 2.7, the north-south motion of the current sheet does not necessarily need to be a smooth transition from one lobe regime to the other. Instead, the magnetic field can be accompanied by short-scale 'jitter' with periods up to 30 min. The occurrence of such short-scale fluctuations of the magnetic field in the magnetodisk's current sheet near Titan is in fact an

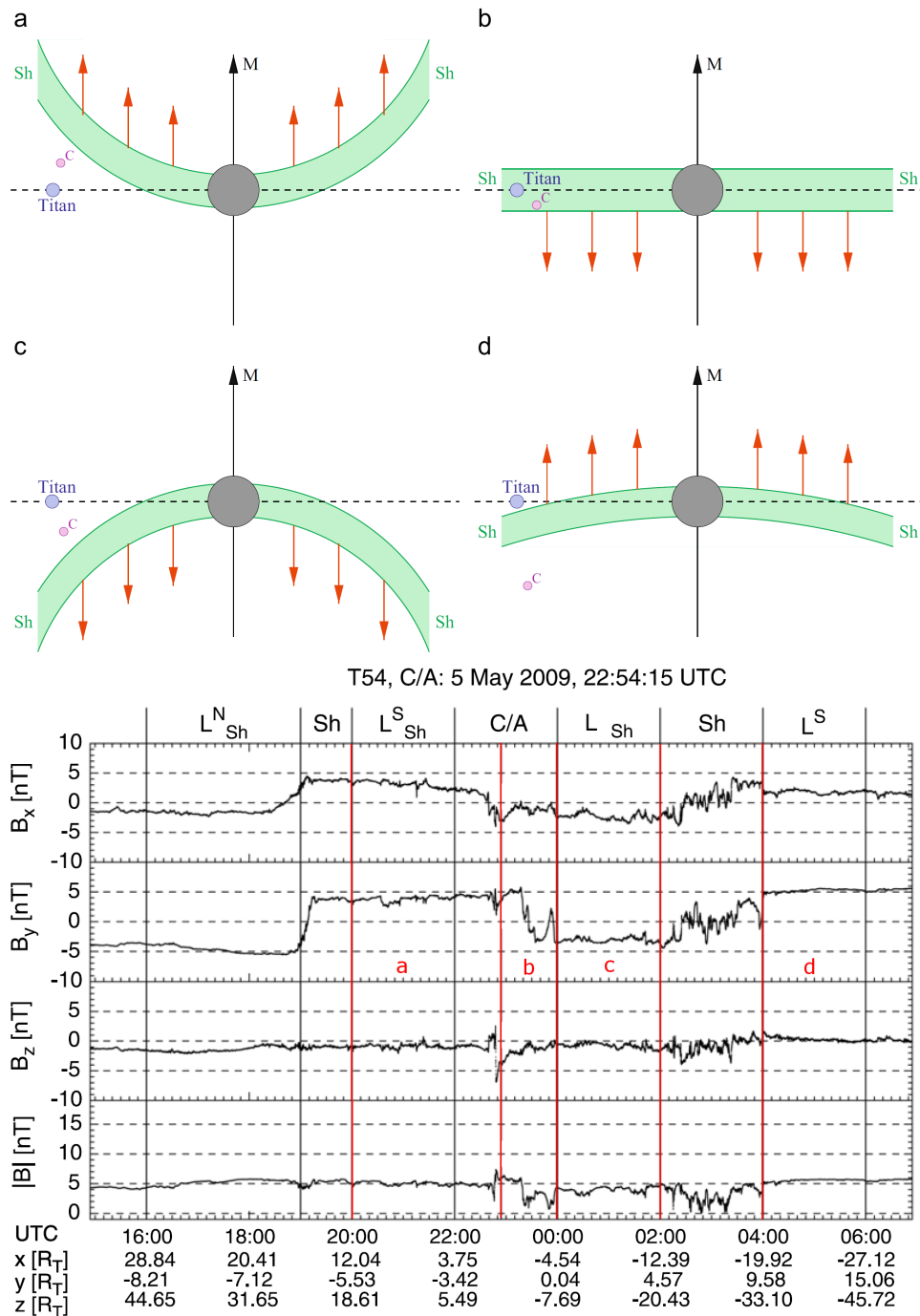


**Figure 2.7:** Sketch of the current sheet (green shaded area) sweeping over Titan and Cassini (C) during T54 (top figure, a-d) combined with the magnetic field observations made by Cassini (bottom figure). The areas distinguished by the red lines and marked with characters a, b, c, d in the magnetic data plot correspond to the four snapshots of the magnetodisk's state in the top figure. **(a)** Cassini and Titan are located in the southern magnetodisk lobe region after a northward sweep of the current sheet **(b)** The recurring current sheet sweeps back over Titan shortly after closest approach **(c)** The current sheet has swept south past Titan and Cassini, putting both in the northern magnetodisk lobe regime **(d)** The current sheet sweeps back again and is now located above Cassini, putting the spacecraft again in the southern lobe. Figures from Simon et al. (2010).

omnipresent feature and has been observed multiple times by Cassini (e.g. figure 2 in Arridge et al. (2007), figure 7 in Simon et al. (2010)). The magnitude of the 'jittering' in the current sheet can be comparable to the background magnetic field strength and even last for several hours, as evidenced during the T20 encounter (see figure 6 in Simon et al. (2010)).

The picture of the magnetospheric conditions that arises near Titan (and generally in the outer magnetosphere at distances  $> 15 R_S$ ) is that of a highly disturbed magnetospheric environment. The various dynamic processes of the magnetodisk current sheet can change the conditions near Titan on timescales of minutes and may influence Titan's plasma interaction significantly during a single Cassini flyby. For this reason, several classification schemes have been developed in the past in order to characterize the plasma environment near Titan's interaction region on an encounter-to-encounter basis, utilizing different Cassini instruments and the large data set of Titan flybys.

Using electron spectra obtained from the Cassini Plasma Science (CAPS) and Magnetospheric Imaging Instrument (MIMI) instruments, Rymer et al. (2009) developed such a classification scheme for the encounters TA-T54. This scheme was later expanded up to the T84 flyby by Smith and Rymer (2014), which was the last Titan encounter where the CAPS instrument was still operational on board of Cassini. Observational data in a  $\pm 3$  h window around closest approach is considered. The scheme by Rymer et al. (2009) distinguishes between four types of encounters based on the peak energy and flux density of the observed electron distribution: 'plasma sheet' (high energy, high flux), 'lobe-like' (high energy, low flux), 'magnetosheath' (low energy, very high flux) and 'bimodal' (superposition of cold and high energy electron populations). The specific criteria for each type are listed in table 2.1. Encounters that could not unambiguously be identified were marked as unclassifiable and those with more than one type identified, as mixed. A mixed classification typically indicates transition between plasma regimes over the course of an encounter. The combined surveys of Rymer et al. (2009) and Smith and Rymer (2014)

Classification	Peak energy (eV)	Peak flux ( $10^{10} \text{m}^{-2} \text{s}^{-1} \text{sr}^{-1}$ )
Plasma sheet	120-600	0.35-1.2
Lobe-like	150-820	0.053-0.24
Magnetosheath	$\sim 50$	1
Bimodal	200-3400	0.09-0.24
	5.3-16.3	0.57-1.6

**Table 2.1:** Criteria for the Titan encounter classification scheme based on electron data from Rymer et al. (2009).

showed that from the set of TA-T84, 45% of the encounters took place when Titan was embedded in the current sheet and 38% in lobe-like conditions. Only two encounters were identified where Titan was close to or in the magnetosheath, T32 and T42. The study by Smith and Rymer (2014) also investigated the plasma environment for virtual encounters when Cassini crossed Titan's orbital path with the moon absent. A comparison of the Titan encounters and Titan orbit passings according to their local time showed that the distribution of the different plasma environments was similar in both cases, with only small differences. They found that without the moon the probability of the plasma environment being embedded in the current sheet at Titan's orbital distance is slightly

Classification	Mnemonic	Criteria
Magnetodisk lobe	$L^N$ and $L^S$	$ B_y /B > 0.6, \delta B_y/B \leq 0.05$
Lobe with current sheet features	$L_{Sh}, L_{Sh}^N, L_{Sh}^S$	$ B_y /B > 0.6, 0.05 < \delta B_y/B \leq 0.05$
Current Sheet	Sh	$ B_y /B < 0.6, \delta B_y/B \leq 0.2$

**Table 2.2:** Criteria for the Titan encounter classification scheme based on magnetic field data from Simon et al. (2010).  $B_y, B$  are mean values over 1 hour intervals, with  $\delta B_y$  being the standard deviation. The indices N and S denote northern and southern lobe regimes.

increased with 55%. They also found that in the pre-noon to noon local time sectors, the probability of encountering magnetosheath plasma conditions is slightly increased when Titan is absent, supporting theories that Titan may influence or maintain its own plasma environment to a certain degree (Wei et al. 2009, Snowden et al. 2011a).

The classification scheme by Rymer et al. (2009) was later supported by a study based on ion spectra by Németh et al. (2011). The classifications based on ion-spectra for the first 54 Titan encounters were found to be in very good agreement with those obtained through electron observations. However, Németh et al. (2011) stated that in reality most of the encounters were more of a mixed type classification from the ion point of view. They noted that shorter time intervals would allow a clear classification in most cases. Garnier et al. (2010) also classified all crossings of Titan's orbit by Cassini before 2008 using the flux spectra of high energy (27-255keV) protons.

Simon et al. (2010) developed a classification scheme of the Titan's plasma environment based on Cassini magnetic field observations for the flybys TA-T62. This study was later continued up to T85 by Simon et al. (2013). A much longer time-interval of data of  $\pm 8$  h was considered here, in order to account for possible much longer lifetimes of fossilized magnetic fields in Titan's tail (see also section 2.4). Three different magnetic regimes were considered by Simon et al. (2010): the magnetodisk lobes ( $L$ ), where the magnetic field is highly stretched and quiet, the current sheet ( $Sh$ ) which is identified by a weak radial component and increased fluctuations, and a transitional regime ( $L_{Sh}$ ) with characteristics of lobe fields distorted by current sheet fluctuations. The exact classification criteria from Simon et al. (2010) are displayed in table 2.2.

Simon et al. (2010) found that during most flybys Titan was embedded either in the highly perturbed magnetic environment of the current sheet or in a transitional magnetic environment between lobe-like and current sheet fields. They also found that for a series of flybys that took place during southern summer (T16-T24), the magnetic field above Titan's orbital plane was characterized by a mixture of lobe-like and current sheet fields and below Titan's orbital plane they mainly belonged to the lobe category. This finding is therefore consistent with the warping of the magnetodisk into the bowl-shape form during southern summer (Arridge et al. 2008a). However, a series of flybys that occurred around equinox in 2009 also revealed that the picture of a quasi-stationary magnetodisk cannot be sustained. During those flybys, Titan's magnetic environment was characterized by frequent current sheet crossings, contradicting the expected picture of rather quiet conditions and an unwrapped magnetodisk near equinox.

A detailed review and comparative analysis of these classification schemes was done in a study by Arridge et al. (2011a). Table 11 in that work lists all flybys from TA-T85 and the classification of each encounter according to the schemes of Rymer et al. (2009), Simon

et al. (2010), Németh et al. (2011) and Garnier et al. (2010). Arridge et al. (2011a) point out the importance of the different time-intervals that were considered in each classification scheme which leads to varying classifications for some of the Cassini flybys.

It should also be noted that despite the fact of the high variability in the plasma parameters and the magnetic field, these variabilities do not necessarily need to be in phase with each other or be observable over the same spatial volume. This means that applying strict criteria from only one classification scheme may not be sufficient for a complete description of Titan's upstream plasma environment for a given Cassini flyby. Therefore, a combined classification of the plasma environment near Titan using multiple instruments is needed in order to obtain a complete picture.

One example is the T11 encounter which took place in the plasma sheet from the electron point of view but the magnetic field classification put it in the lobe region, since they met the criteria for these regimes in the respective classification schemes (see table 11 in Arridge et al. (2011a)). Figure 2.8 shows the combined electron and magnetic data from that flyby. Looking only at the electron data in the  $\pm 3$  h interval around closest approach reveals indeed an electron population around 100 eV that is consistent with the current sheet criteria, albeit at very low densities. Outside this interval, the electron densities are even lower. Over the whole  $\pm 8$  h interval the magnetic field data clearly suggest an magnetic environment that belongs to the southern magnetodisk lobe ( $B_r < 0$ ,  $B_\phi > 0$ ). Inside the  $\pm 3$  h interval, the magnetic field tends more towards the current sheet (indicated by  $B_r$  and  $B_\phi$  approaching zero), however it is still classified as lobe-like according to the classification criteria (table 2.2).

Combining these findings, Arridge et al. (2011a) conclude that the plasma environment during T11 belongs to the outer layers of the plasma sheet, where the magnetic field lines are already stretched and swept back, but still inside a region with a current sheet like electron population. In particular, near closest approach the spacecraft came closer to the current sheet region which is clearly seen in the radial magnetic field component. Thus, this example shows that Saturn's magnetodisk near Titan is not a region with clearly defined and separated plasma regimes. The different plasma regimes exist and can be identified from the magnetic or electron/ion point of view but they do not need to strictly correlate or overlap with each other at all times.

The highly variable magnetospheric environment makes it very difficult to provide well defined parameters for the upstream plasma at Titan. However in order to perform numerical studies of Titan's plasma interaction, it is often necessary to have some kind of stationary and homogenous upstream conditions in the magnetic field and plasma composition. A time dependent upstream plasma has the problem that the Cassini observations only provide a very limited and spatially confined view along the spacecraft's trajectory on Titan's plasma environment, potentially missing important aspects. Also additional problems may arise with regards to numerical stability when time dependent upstream data is used. This is in contrast to the situation at, e.g., Enceladus which is located very close to Saturn in the inner magnetosphere. At Enceladus, the magnetospheric dynamics have a much smaller impact and the moon is usually embedded in a more homogeneous and quiet plasma environment with well known parameters. At Titan, the definition of an average upstream plasma with a certain composition, mass density, magnetic field vector, and temperature is not very meaningful because of the high variability in these parameters.

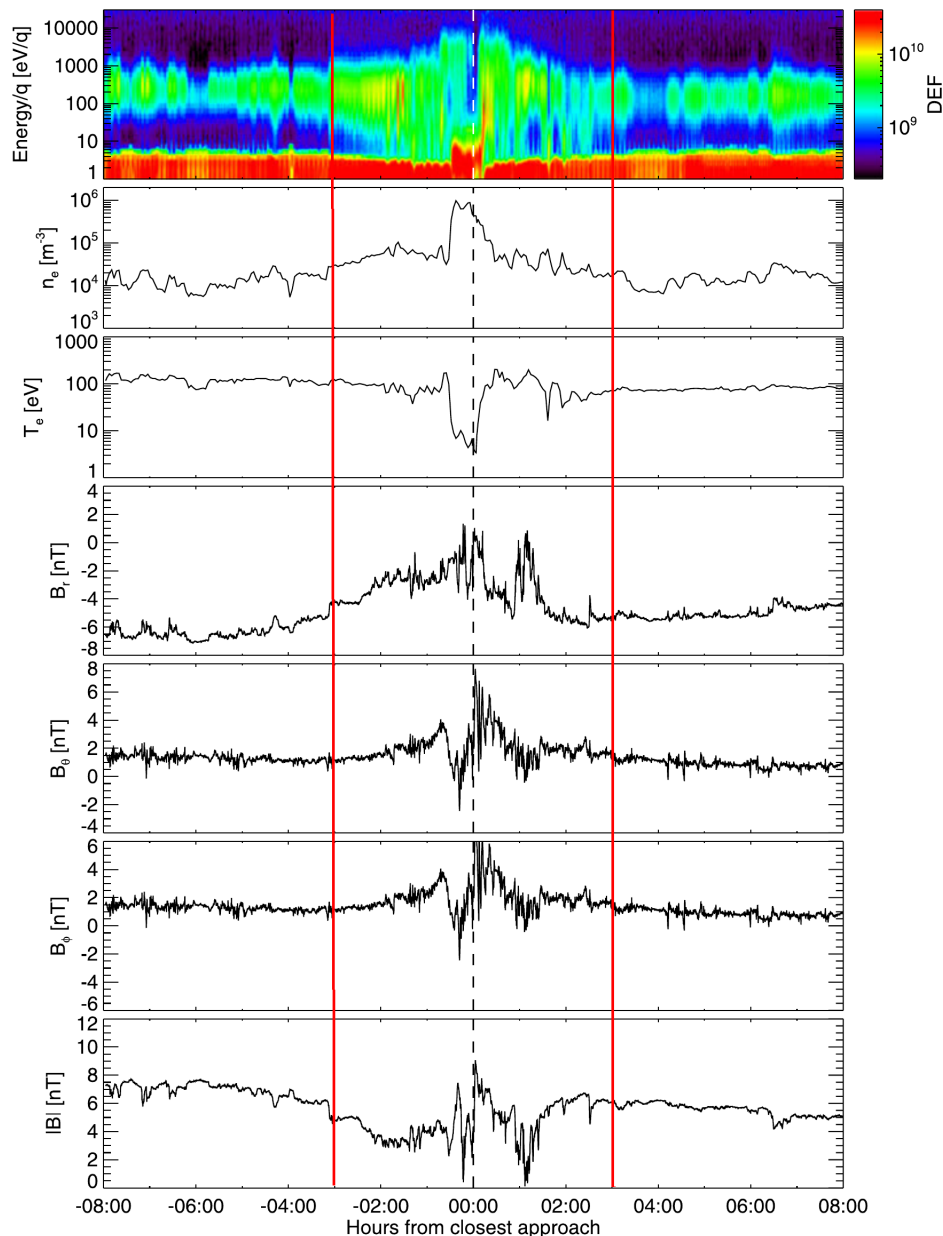


**Figure 2.8:** Electron and magnetic field data from the T11 flyby. The top three panels show the raw electron spectra, electron density  $n_e$  and electron temperature  $T_e$ . The bottom four panels show the three components  $B_r$ ,  $B_\theta$ ,  $B_\phi$  and magnitude  $B$  of the magnetic field. The red lines illustrate the  $\pm 3$  h interval that was considered by the electron classification scheme (Rymer et al. 2009). The whole plot covers the range of  $\pm 8$  h considered by Simon et al. (2010). The magnetic observations are overall consistent with the magnetospheric environment of the southern magnetodisk lobe, whereas the electron spectra indicate that Titan is embedded in current sheet plasma with a low density. Due to the different time intervals and strict classification criteria based on single instruments applied in those classification schemes, only partial aspects of Titan's ambient magnetospheric environment may be identified. Figure from Arridge et al. (2011a)

Quantity	Symbol	Value	Comments
Magnetic field orientation	$\underline{B}_0/B_0$	(0,0,-1)	North-south oriented, strong $B_y$ , $B_x$ components in magnetodisk lobes
Magnetic field strength	$ \underline{B} _0$ [nT]	5	Usually stronger field strength in magnetodisk lobes
Upstream O <sup>+</sup> number density	$n_{0,O^+}$ [cm <sup>-3</sup> ]	0.2	Density lower in magnetodisk lobes
Upstream H <sup>+</sup> number density	$n_{0,H^+}$ [cm <sup>-3</sup> ]	0.1	and dominated by protons
Electron Temperature	$T_e$ [eV]	200	
Electron plasma beta	$\beta_e$	0.97	
Electron plasma frequency	$\omega_{pe}$ [s <sup>-1</sup> ]	$30.9 \cdot 10^3$	
Ion Temperatures	$T_{i,O^+}$ [eV]	2900	Lower temperature
	$T_{i,H^+}$ [eV]	210	in magnetodisk lobes
Ion plasma beta	$\beta_i$	9.66	
Plasma bulk velocity	$ \underline{U} _0$ [km/s]	120	Mostly corotational direction with radial deviations
Alfvén velocity	$v_A$ [km/s]	60	
Sound velocity	$c_s$ [km/s]	196	
Magnetosonic velocity	$c_{MS}$ [km/s]	205	
Alfvénic Mach number	$M_A$	2	Superalfvénic
Sonic Mach number	$M_S$	0.61	Subsonic
Magnetosonic Mach number	$M_{MS}$	0.59	Submagnetosonic
O <sup>+</sup> gyration frequency	$\Omega_{O^+}$ [s <sup>-1</sup> ]	0.03	
O <sup>+</sup> gyration radius	$R_{g,O^+}$ [ $R_T$ ]	1.56	Comparable to Titan's radius

**Table 2.3:** List of typical upstream plasma parameters near Titan inside Saturn's magnetosphere. The values listed here were derived from the observations made during the Voyager 1 flyby (Neubauer et al. 1984) and are representative for the ambient plasma conditions of a dense and hot current sheet plasma with a strictly north-south oriented magnetic field. Note that the plasma conditions usually show deviations from these values during spacecraft flybys due to the reasons discussed in this section.

Despite, it has become common to use the plasma parameters that have been obtained during the Voyager 1 flyby (Neubauer et al. 1984) as a first basis for simulations of Titan's plasma interaction. The conditions that were found during this flyby are characteristic of a very dense and high temperature current sheet plasma with a strictly north-south oriented magnetic field (see table 2.3). While the current-sheet like plasma (albeit less hot and dense) has been confirmed to be the average state of Titan's plasma environment, the magnetic conditions of the Voyager 1 flyby have only been observed one other time in the Cassini era during the T70 encounter (Simon et al. 2013).

Recently, Achilleos et al. (2014) combined a global model of Saturn's magnetodisk with a geometrical model of an oscillating current sheet in order to model the time dependent plasma conditions near Titan. Using their model they were able to reproduce several of the large scale periodic signatures that were observed in the magnetic field data during Cassini's T15 flyby. They also found that the magnetic pressure makes up the predominant part of the upstream flow pressure when Titan is located within the magnetodisk

Species	Near Surface (0-6 km)	Thermosphere (1150 km)
N <sub>2</sub>	94.2±0.1%	96.6 ± 0.1%
CH <sub>4</sub>	5.6 ± 0.1%	3.0 ± 0.1%
H <sub>2</sub>	0.1 ± 0.01%	0.43 ± 0.01%

**Table 2.4:** Mole fractions of the main constituents of Titan's neutral atmosphere near the surface and in the upper ionosphere. Other neutral species make up less than 0.01% of the total density. Values from Cui et al. (2009) and Niemann et al. (2010).

lobes. When Titan is embedded in the plasma of the magnetodisk current sheet, the dynamic pressure of the plasma contributes the most to the total pressure. Achilleos et al. (2014) showed that the total pressure may increase by a factor of 3 during a transition from the magnetodisk lobes to the current sheet.

## 2.2 Titan's Atmosphere

Titan's nitrogen-rich atmosphere is among the most complex in the entire solar system. It has not only the most dense atmosphere compared to other moons, with the surface pressure being even higher than at Earth, it also has an extensive ionosphere that leads to a characteristic interaction with Saturn's magnetospheric plasma. Understanding the complex structure of the Titan's neutral atmosphere and ionosphere as well as the various processes that lead to these structures have been a major topic of research since the Voyager 1 flyby and especially since Cassini's arrival at Saturn and the landing of the Huygens probe on the moon's surface in 2005. In the following we will give a brief overview of the most important aspects of Titan's atmosphere.

Spectral analyses of Titan prior to the Voyager 1 flyby already had revealed that CH<sub>4</sub> is a minor constituent of the atmosphere along with H<sub>2</sub> (Trafton 1972a,b). However it was not clear what the main component of Titan's atmosphere was. The final detection of the main N<sub>2</sub> component was achieved by ultraviolet spectral observations made during the Voyager 1 flyby (Broadfoot et al. 1981). Table 2.4 shows the mole fractions of the most abundant neutral species, N<sub>2</sub>, CH<sub>4</sub> and H<sub>2</sub> near the surface and in the ionosphere. As we can see, the mole fractions are not constant over the whole atmosphere, but show a slight variation depending on the altitude. This is rooted in the complex neutral and ion-neutral chemistry that takes place all over Titan's atmosphere and which is fueled by the ionization of the main neutral components. There are several processes that take part in the ionization of neutrals over the whole range of Titan's neutral atmosphere. The first one is ionization through solar X-ray and EUV radiation. Photoionization is the most important process for the ionization of the neutral atmosphere (e.g. Coates et al. (2011)). The peak density of the photogenerated day side ionosphere varies from 2500-3500 cm<sup>-3</sup> and is usually located at an altitude between 1050-1150 km, depending on the intensity of the incoming solar radiation (Ågren et al. 2009). Impact ionization through energetic electrons and protons from Saturn's magnetosphere is the second source of ionization. The electrons mostly contribute to the ionization in the upper part of the ionosphere around the peak altitude (e.g. Krasnopolsky (2009)). Also secondary ionization through photoelectrons contributes in that region. The more energetic ions, mostly protons and oxygen (see table 2.3), are able

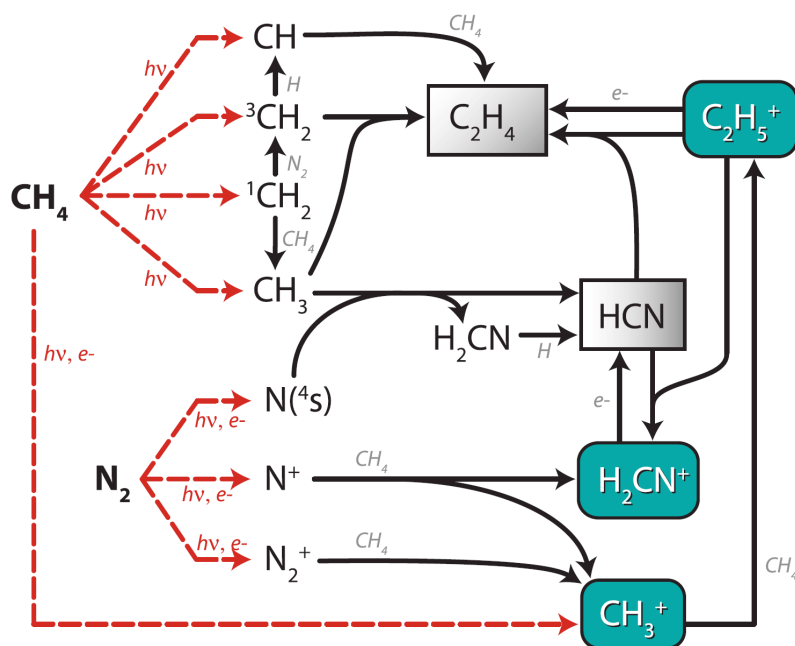


**Figure 2.9:** Chemistry chart that covers some of the most important chemical reactions of Titan's atmosphere. The main neutral components  $\text{N}_2$  and  $\text{CH}_4$  are ionized through various processes and converted through chemical reactions into the main ion species  $\text{C}_2\text{H}_5^+$  and  $\text{HCNH}^+$ . Figure from De La Haye et al. (2008).

to penetrate deeper into the neutral atmosphere and generate an additional ionospheric layer at altitudes between 500-1000 km (Kliore et al. 2008, Cravens et al. 2008). A third source of ionization is given by extreme energetic cosmic rays that generate a prominent ionospheric layer at very low altitudes. Measurements made by the Huygens probe on its decent to the surface revealed an ionospheric peak at an altitude of 65 km with densities of  $2000 \text{ cm}^{-3}$  for positive ions and  $450 \text{ cm}^{-3}$  for electrons (López-Moreno et al. 2008). On the night side, only impact ionization by magnetospheric particles contributes to the generation of the upper ionosphere. In general, the electron density on the night side is by a factor of 5-6 lower than the peak density on the day side (e.g. Ågren et al. (2009)). The ionization and dissociation of the main neutral constituents starts a chain of chemical reactions between ions and neutrals that creates a plethora of new neutral and ion species in the mass range from 1 amu up to several hundred amu. Also a purely neutral chemistry develops and both ion-neutral and neutral reaction chains are strongly intertwined with each other. Figure 2.9 shows a chart of the most important chemical reactions in Titan's atmosphere. The neutral and ion end products of these reaction chains can be broadly distinguished into two major groups, Carbon-Hydrates ( $\text{C}_x\text{H}_y^{(+)}$ ) and Nitrogen bearing species ( $\text{C}_x\text{N}_y\text{H}_z^{(+)}$ , see also figure 2.10). The neutral end products are only very minor constituents compared to  $\text{N}_2$  and  $\text{CH}_4$ . However, one of the remarkable features of Titan's ionosphere is that the first ionization products of  $\text{N}_2$  and  $\text{CH}_4$ ,  $\text{N}^+$ ,  $\text{N}_2^+$ ,  $\text{CH}_4^+$  and  $\text{CH}_3^+$ , are rapidly converted into  $\text{C}_2\text{H}_5^+$  (benzhol) and  $\text{HCNH}^+$  (hydrogen cyanide) which have been observed to dominate the ionospheric composition (Cravens et al. 2006). Organic compounds of high mass have been found to dominate the lower atmosphere, as they are more susceptible to gravitation. At the bottom of the atmosphere, aerosols with

masses up to  $\sim 40000$  amu form the thick orange colored haze layer seen in figure 1.1. The aerosols are believed to be the chemical product of reacting high mass organic compounds as they sink towards the surface (Waite et al. 2007).

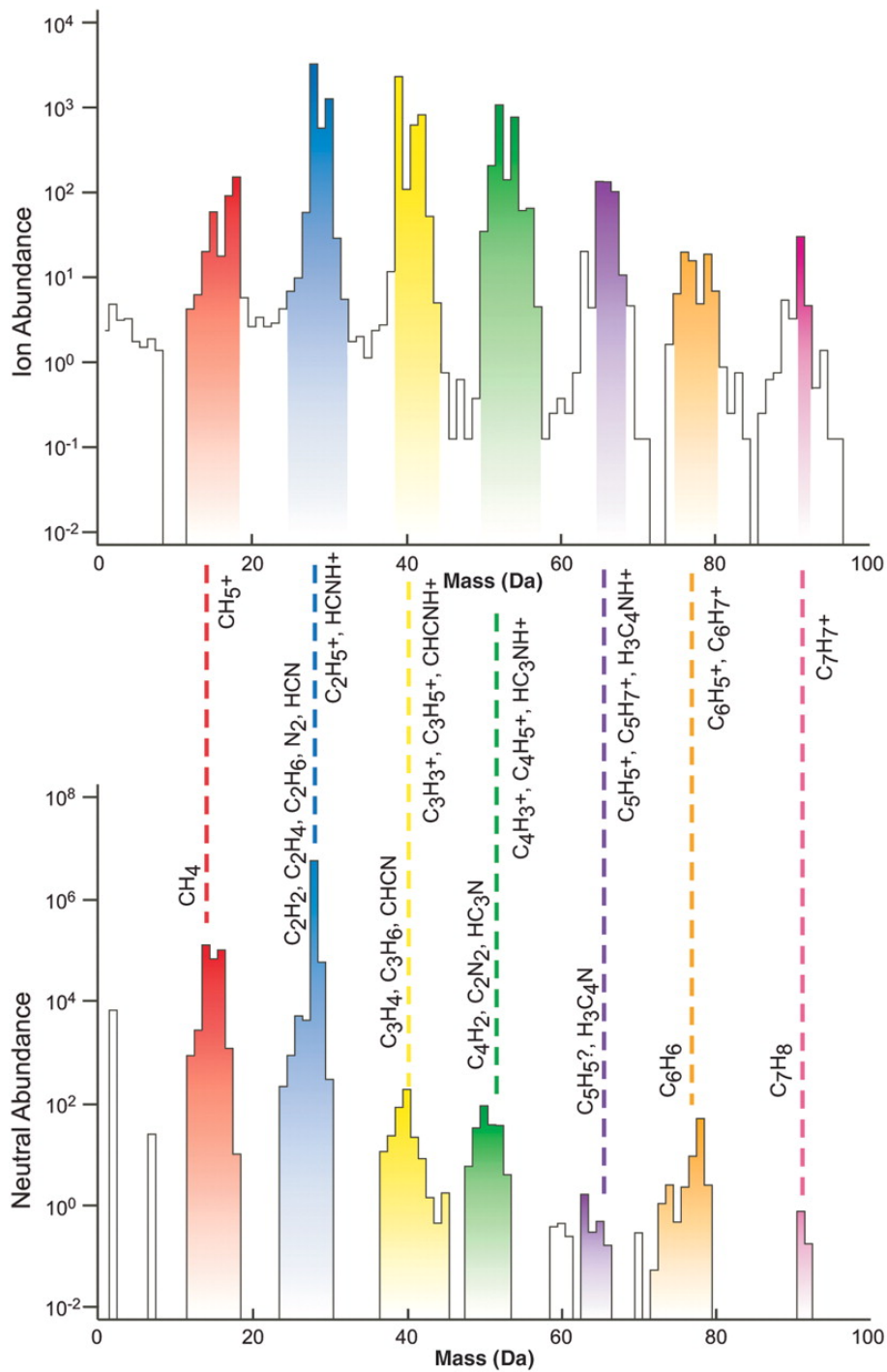
The picture of the chemistry became even more complex with the discovery of negatively charged ions in Titan's ionosphere (Coates et al. 2007a, 2009). The observations showed the occurrence of negative ions over a wide range of masses, with a peak mass-to-charge ratio of over 10000 amu/q (Coates et al. 2007a). The amount of negative charges was suggested to be as high as  $q=5$ , thus the mass of negative ions may be as high as 50000 amu (Coates et al. 2007a). Observations from multiple Cassini flybys showed that the distribution of negative ions is correlated to their mass (Coates et al. 2009, Wellbrock et al. 2013). Negative ions with a higher mass peak at lower altitudes and also the maximum altitude where they are observed decreases with increasing mass.

Figure 2.10 gives an impression of the complexity of Titan's atmosphere. The plot shows the ion and neutral mass spectra between 950 and 1000 km, measured by Cassini during the T19 flyby. One can clearly see that the ion and neutral species are clustered in various groups that cover a certain mass range. This is due to the fact that most of the chemical reactions are rooted to the neutral nitrogen and methane, which means that the 'gaps' between the mass groups will be on the order of 12-14 amu. Also these mass groups show a clear correlation between the neutrals and ions.

## 2.3 Titan's Plasma Interaction

Titan does not possess a detectable intrinsic magnetic field that may impact the magnetic signature of its plasma interaction with the magnetospheric plasma. The magnetic observations made during the Voyager 1 flyby yielded an upper limit of the magnetic moment of  $|M| < 4.1 \text{ nT } R_T^3$  (Neubauer et al. 1984). Later, a study by Wei et al. (2010) based on the data of several Cassini flybys further reduced this limit to a value of  $M < 0.78 \text{ nT } R_T^3$ . The error in each component of the magnetic moment in this study was calculated to be on the same order. Therefore, Titan's magnetic moment is either non-existent, or at least about 1000 times smaller than that of Ganymede (Magnetic moment of  $|M| = 711 \text{ nT } R_G^3$ ), which is the largest moon in the Solar System ( $R_G = 2634 \text{ km}$ ) and the only one with a known intrinsic magnetic field. However, some studies suggest the existence of conducting layers on or in the moon (Béghin et al. 2009) and in the ionosphere (Rosenqvist et al. 2009, Cravens et al. 2010) that might influence the lifetime of magnetic fields in Titan's lower ionosphere.

As Titan orbits around Saturn at a velocity of  $\sim 5.57 \text{ km/s}$ , it is constantly overtaken by the Saturnian magnetospheric plasma that travels at sub-corotational speeds of  $\sim 100 \text{ km/s}$  (rigid corotational speed near Titan is  $200 \text{ km/s}$ ). The moon and the plasma move in the same direction around Saturn (counterclockwise), the magnetospheric plasma therefore impinges 'from behind' on Titan. Since the moon does not possess an intrinsic magnetic field of relevant strength, the magnetospheric plasma interacts directly with Titan's atmosphere and ionosphere. This interaction leads to the formation of an 'induced magnetosphere' around Titan, which means a perturbation of the upstream magnetic field and plasma due to the transfer of energy and momentum into the atmosphere (Bertucci et al. 2011). An example of an 'intrinsic magnetosphere' would be the interaction of Saturn



**Figure 2.10:** The ion and neutral mass spectra of Titan's upper ionosphere measured by Cassini during the T19 flyby. Neutral and ion species cover a wide range of masses and cluster around certain mass values as a result of the Nitrogen-Methane driven chemistry. Figure from Waite et al. (2007).

with the solar wind (due to Saturn's intrinsic magnetic field). The formation of the induced magnetosphere is a combination of the massloading and diversion of the upstream magnetospheric plasma flow around the moon's ionosphere. As

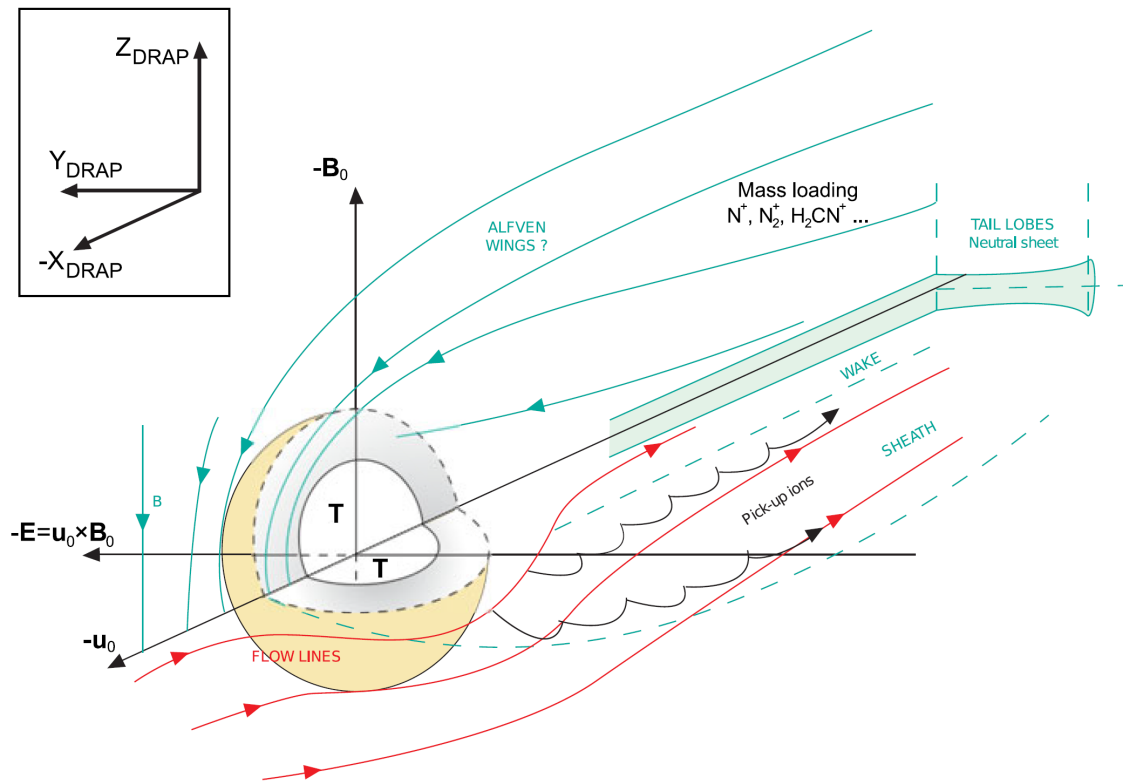


**Figure 2.11:** Schematic of the main features of Titan's plasma interaction. The DRAP coordinate system is used (see text). Titan's induced magnetosphere consists of piled-up and draped field lines and a diversion of the upstream flow around the ionosphere. Downstream a magnetotail is formed by two magnetic lobes of reversed polarity. Ions originating from Titan's ionosphere escape in the magnetic wake via pick-up processes. Figure from Arridge et al. (2011a).

the upstream plasma approaches Titan, more and more ions originating from the moon's ionosphere are added to the plasma. The ionospheric ions are generated for the most part through photoionization of the neutral atmosphere and are much colder (few eV) compared to the upstream plasma. These newborn ions are also much slower than the upstream plasma, since their parent neutrals possess only a negligible velocity (on the order of the neutral constituents' wind speed of 100 m/s to  $\sim 1$  km) compared to the rest frame of the upstream plasma. Thus, the bulk velocity of the upstream plasma needs to decrease in order to conserve momentum as it gets progressively massloaded while approaching Titan. The moon's electrically conducting ionosphere also acts as an obstacle to the impinging plasma flow. The induced currents prevent the magnetized magnetospheric plasma from penetrating the conducting obstacle by diverting the plasma flow around the ionosphere. As a result of these processes, the frozen-in magnetospheric field lines drape around the conducting ionosphere, generating a characteristic perturbation signature of the magnetic field.

The general structure of Titan's induced magnetosphere for an idealized geometry of the upstream flow conditions is illustrated in figure 2.11. This figure uses the DRAP (draping) coordinate system of (Neubauer et al. 2006), in which the  $z$  axis is anti-parallel to

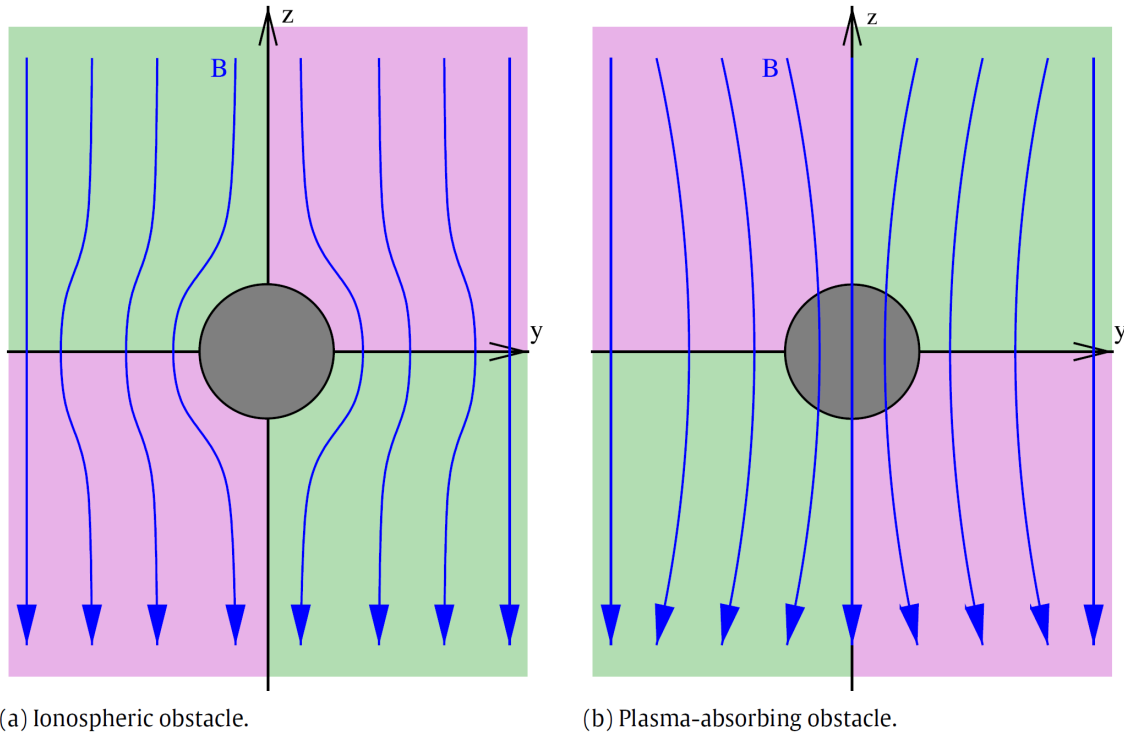


**Figure 2.12:** Sketch of the downstream magnetic field structure for an **(a)** ionospheric obstacle (Titan) and **(b)** a purely plasma absorbing obstacle. The figure shows a  $x = \text{const}$  plane that cuts through the downstream tail region of the obstacle. The grey circle denotes the intersection with the obstacle's plasma wake. Areas with  $B_y < 0$  are marked in green, and areas with  $B_y > 0$  are marked in magenta. **(a)** In the case of an ionospheric obstacle where the tail is filled with cold escaping ions, the magnetic field is pushed out of the wake region. **(b)** The exact opposite happens for a plasma absorbing obstacle, where the magnetic field is pushed into the less dense wake region to compensate the lack of plasma pressure, which leads to an increase of magnetic field strength in the wake and a reversed  $B_y$  pattern. Figure from Simon et al. (2015).

the upstream magnetic background field  $\underline{B}_0$ , the strictly corotational upstream flow  $\underline{U}_0$  is aligned with the  $x$  axis and the resulting convective electric field  $\underline{E}_0 = -\underline{U}_0 \times \underline{B}_0$  defines the  $y$  axis. Note that this system is identical to TIIS coordinates (Section 2.1.1) for a strictly north-south magnetic field and a corotational flow. On the ramside, the magnetic field strength is enhanced as a result of the pile-up of magnetic field lines in the massloaded region. The entrance to the induced magnetosphere is indicated by the induced magnetosphere boundary (IMB). The IMB is characterized by a strong change in the magnetic field strength (also called magnetic barrier or magnetic pile-up) and occurrence of draped field lines, a decrease in electron temperature as well as a decrease in the density of upstream ion species (Bertucci et al. 2011). The inner boundary of the induced magnetosphere is marked by the ionopause (IP), which is characterized by the occurrence of a cold photoelectron population and an increase in the electron density as well as a decrease of the magnetic field strength (Bertucci et al. 2011). Downstream of the moon, two magnetic lobes with opposite polarities form Titan's magnetotail. The magnetic lobes are a direct consequence of the draping of magnetic field lines around the ionosphere. De-

pending on the orientation of the upstream magnetic field, the lobes have a characteristic magnetic signature by which they are identified. For a strictly north-south ( $B_z < 0$ ) oriented background field, the northern lobe is identified by a negative  $B_x < 0$  component and southern lobe by a positive  $B_x > 0$  component.

The interior of the downstream tail (also called wake) is filled with escaping cold plasma from Titan's exosphere. Due to the increased density in this region, the plasma pressure is therefore enhanced. The magnetic field strength thus needs to be reduced in the same region in order to sustain the total pressure balance  $P_{total} = P_{plasma} + P_{mag}$  between the ambient region and the magnetotail. The region of decreased magnetic field strength in the magnetotail is referred to as Titan's magnetic 'wake'. As a result of the pushed-out magnetic field lines outside of the wake, a distinct pattern in the  $B_y$  component is formed around the magnetotail. This pattern is outlined in figure 2.12 where we also compared it against that of a plasma absorbing inert moon (such as Dione or Rhea), where the opposite effect occurs. The magnetic lobes of the magnetotail are separated by a neutral sheet, where the sign of the  $B_x$  and  $B_y$  perturbations reverse. A consequence of these distinct and spatially confined magnetic signatures in the magnetotail is that they allow for an easy identification of the magnetotail structures and the plasma interaction type (object with or without ionosphere) based on spacecraft measurements.

An important aspect of Titan's plasma interaction are the effects of the large ion gyro radii at Titan. For average plasma conditions, the gyro-radius of 16 amu ions is comparable to the radius of the moon (see table 2.3). Ions from the rest-frame of Titan's ionosphere get accelerated by the convective electric field  $\underline{E}_0 = -\underline{U}_0 \times \underline{B}_0$ . Due to the magnetic field the ions start to gyrate, which ultimately leads to a cycloidal motion in the plane perpendicular to  $\underline{B}_0$  as they get picked up by the ambient plasma flow. This 'pick-up' process leads to a distinct asymmetry in Titan's induced magnetosphere and ion density outflow, with the pick-up ions moving in a confined plane perpendicular to the magnetic field, also called Titan's 'pick-up tail'. The spatial extensions of the pick-up tail are on the order of the local gyro radius (up to several  $R_T$ ). Since the gyro radius scales with the mass of the ions, Titan's pick-up tail may be viewed as a natural mass spectrometer where the ions accumulate according to their mass in the pick-up tail, with the heaviest ions on the outer flank and lighter ions towards the moon (Luhmann 1996). The magnetic perturbations generated by the pick-up ions also distort the magnetic structures with respect to the direction of  $\underline{E}_0$  (see also chapter 4).

For the large majority of Titan flybys however, the upstream geometry of the magnetic background field  $\underline{B}_0$  and the upstream plasma bulk velocity  $\underline{U}_0$  will deviate from the idealized conditions established above (figure 2.11). If  $\underline{B}_0$  and  $\underline{U}_0$  are not perpendicular to each other, further asymmetries are added to Titan's induced magnetosphere, e.g. twisting of the magnetic field in the vicinity of Titan and a deformation of the neutral sheet between the magnetic lobes (Simon and Motschmann 2009). However the general characteristics of Titan's induced magnetosphere and magnetotail do not change compared to the  $\underline{U}_0 \perp \underline{B}_0$  case. If we consider a rotation of the upstream magnetic field around a fixed direction of the upstream flow, the only difference in the large scale structure of Titan's induced magnetosphere and magnetotail is analogous to an equal rotation of these structures around the flow direction itself. However, time dependent changes of the magnetic field may also lead to the fossilization of magnetic field lines in Titan's ionosphere (see the next section 2.4).

There are other bodies in the solar system who show a very similar type of plasma interaction with their surrounding plasma environment. This applies to Venus and Mars, both planets that are unmagnetized (Acuna et al. 1998, Russell et al. 1979) and that also possess an atmosphere, as well as to the interaction of active comets with the solar wind. The induced magnetospheres of these bodies share many features of their structure and generation with that of Titan (Bertucci et al. 2011). This includes the formation of an induced magnetosphere as a result of the massloading of the upstream plasma flow due to the presence of a ionosphere as well as the formation of a characteristic magnetotail with two magnetic lobes. The induced magnetosphere boundary and the ionopause have been observed as well at Mars and Venus (Knudsen et al. 1982, Acuna et al. 1998, Bertucci et al. 2003). At Mars however, the ionopause does not coincide with a drop in magnetic field strength, due to the latent crustal fields. A significant difference to the plasma interaction of Titan is the occurrence of a upstream bow shock at Mars, Venus and also comets. A bowshock can only be developed if the upstream plasma conditions are of supermagnetosonic nature ( $M_{MS} > 1$ ). The flow energy of the impinging plasma is converted into thermal energy at the shock front, leaving a decelerated plasma with  $M_{MS} < 1$  afterward. Near Titan, the plasma conditions are almost always of submagnetosonic nature so that no bow shock is formed. There is only a single observation of a bow shock at Titan in the entire Cassini era so far. This was during the T96 encounter where Titan was located outside of Saturn's magnetosphere in the solar wind (similar to Venus and Mars) (Bertucci et al. 2015). The T96 encounter is subject to discussion in chapter 5 of this thesis.

## 2.4 Fossilized Magnetic Fields at Titan

An interesting aspect of Titan's interaction with its highly variable magnetospheric environment is the so called 'fossilization' (Neubauer et al. 2006) of magnetic field lines in its upper ionosphere: when the ambient magnetic field near Titan changes from one regime to another (e.g. from northern to southern lobe like conditions), the induced draping pattern of the first magnetic regime may prevail in a certain altitude regime of Titan's ionosphere on timescales of up to several hours (Neubauer et al. 2006). This means that during a Titan flyby of Cassini **two** distinct magnetic draping patterns in Titan's induced magnetosphere may be detected: First, a draping pattern that is compatible with the upstream magnetic background field immediately prior to the encounter, and second a draping pattern which is observed closer to the moon and that is compatible with a different upstream magnetic background field which has already gone past Titan.

This 'memory effect' effect of Titan's ionosphere is closely connected to the timescales of plasma transport in the ionosphere. Outside of Titan's atmosphere, the magnetic field is frozen-in with the magnetospheric plasma and therefore magnetic field lines move at the bulk speed of the ambient sub-corotating plasma at around  $\sim 100$  km/s. However, with decreasing altitude towards Titan, the plasma velocity gradually decreases due to mass-loading by very slow moving newly generated ions in Titan's ionosphere and also due to increasing collisions with particles from Titan's neutral atmosphere. Based on MHD simulations (Backes et al. 2005) of Cassini's first Titan encounter, Neubauer et al. (2006) estimated that the plasma bulk velocity decreases from upstream values of  $\sim 100$  km/s down to values of about  $\sim 0.1$  km/s in the altitude range of 1700 – 1400 km (see figure 2.13).

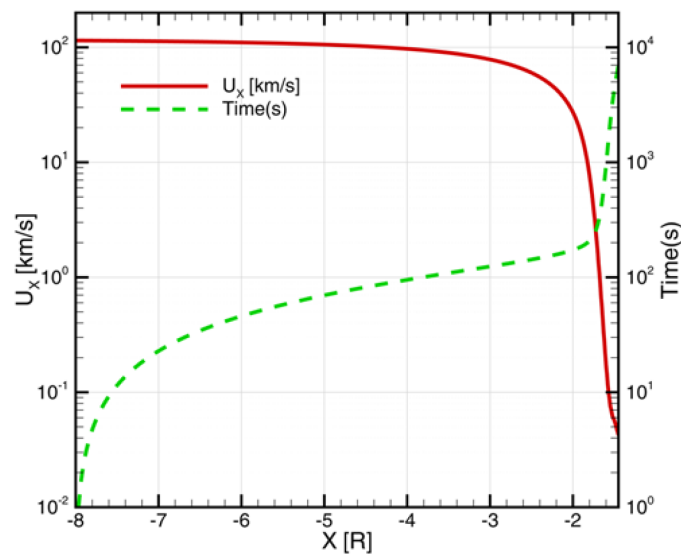


**Figure 2.13:** Illustration of the plasma velocity (solid red) along the ram direction and travel-time (dashed green) of frozen-in magnetic field lines from a distance of  $-8 R_T$ . With decreasing altitude the plasma flow velocity drops and the travel time increases. In the ionosphere the travel-time of field lines goes up to values of hours compared to the outside region. This allows magnetic field lines to 'survive' for an extended period of time in this region regardless of changes in the upstream magnetic field. Figure from Ma et al. (2009).

We note that fossilized fields are constrained to a rather narrow altitude regime in Titan's ionosphere. It is essentially the altitude regime where the region of very slow plasma flow velocity overlaps with the region in Titan's ionosphere where plasma transport is still convection dominated. However, with decreasing altitude the transport of magnetic field lines becomes more and more diffusion dominated due to the increased neutral density. The transition from a convection-dominated to diffusion-dominated plasma flow was suggested by Cravens et al. (2010) to be located at around  $\sim 1000$  km altitude. Below this altitude the magnetic field is detached from the plasma and is transported through magnetic diffusion.

After the prediction of the existence of fossilized magnetic fields in Titan's ionosphere by Neubauer et al. (2006), so far there have only been two observations of this phenomenon through subsequent Cassini measurements. The first happened during Cassini's T32 encounter on 13 June 2007 and the second during the T96 encounter on 01 December 2013 (see chapter 5 for a discussion of the T96 encounter). In both these cases the ambient magnetic field underwent a significant change in direction before Cassini entered the Titan interaction region. Beforehand of T32, the solar wind dynamic pressure was enhanced compared to normal levels so that Saturn's magnetopause was pushed back towards Saturn and swept multiple times over the Cassini spacecraft (Bertucci et al. 2008). The situation prior to Cassini's flyby past Titan was such that the moon was embedded inside Saturn's magnetosphere for  $\sim 3$  hours with a mainly southward oriented magnetic background field. Around 10 minutes before Cassini entered the Titan interaction region the magnetopause swept back over Titan, exposing the moon to a mainly northward oriented

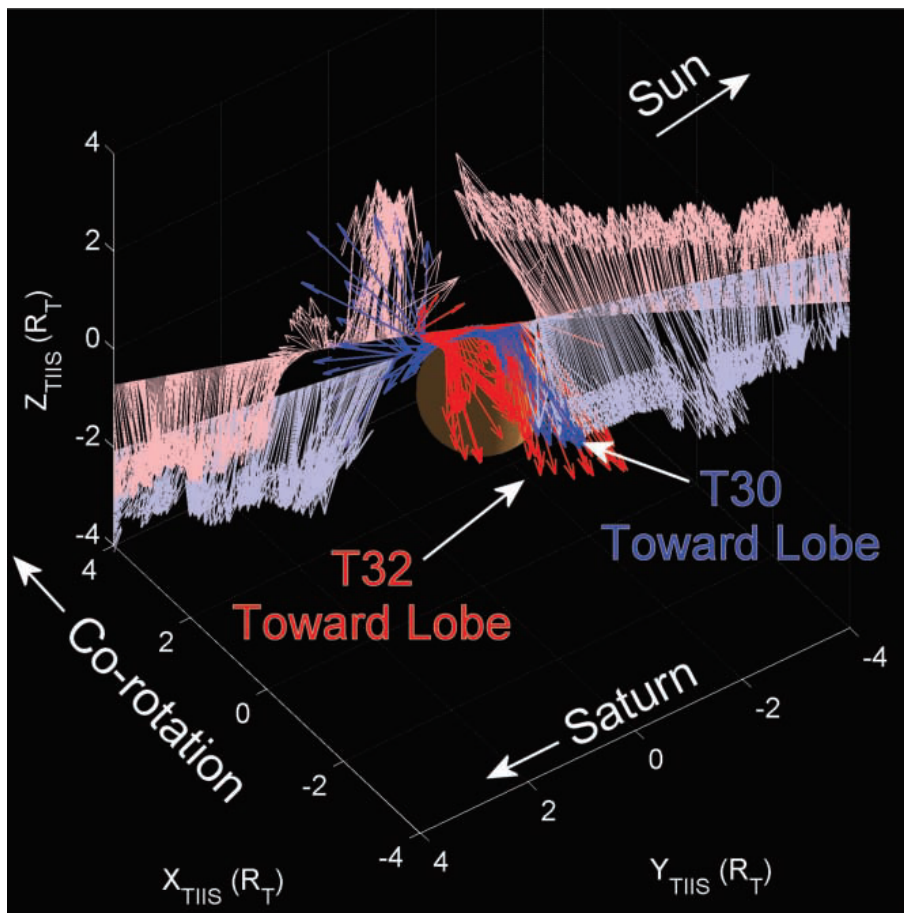


**Figure 2.14:** Observation of fossilized magnetic field lines during the T32 flyby. The plot shows magnetic measurements along the flyby trajectories of T32 (red arrows) and T30 (blue arrows) in TIIS coordinates. Magnetic field vectors that belong to the draped field of Titan's induced magnetosphere are highlighted in darker colors, whereas the unperturbed ambient magnetic field is indicated by lighter colors. Figure from Bertucci et al. (2008).

magnetic field from the magnetosheath (Bertucci et al. 2008).

The situation of this flyby is illustrated in figure 2.14. Cassini was located at northern altitudes and traveling away from Saturn. The figure also shows the magnetic measurements along the T30 encounter which has a very similar flyby trajectory to T32 with a similar southward oriented ambient magnetic field near Titan. The draped field lines of Titan's induced magnetosphere (dark blue arrows) for T30 show the typical magnetic signature that is expected for these conditions, with a strong component along the negative  $x$ -direction (described as toward lobe in figure 2.14). However, for the T32 case, Titan's induced magnetosphere shows a similar magnetic signature (dark red arrows) that is not compatible with the northward pointing ambient magnetic field of the magnetosheath in which Titan was embedded in prior to the encounter. For this magnetic field one would expect to observe a component along the positive  $x$ -direction instead, which was not observed. Bertucci et al. (2008) thus concluded that Titan's induced magnetosphere during T32 was dominated by fossilized magnetic fields from the 3 h time interval where the moon was located inside Saturn's magnetosphere.

Several studies have further constrained the theoretical lifetime of the fossilized magnetic fields. Initially, Neubauer et al. (2006) predicted a possible lifetime of up to several hours. This timescale was substantiated by the study of Bertucci et al. (2008), who constrained the lifetime to a window of  $\sim 20$  min to  $\sim 3$  h, based on the observations made during the T32 encounter. Values in this range were later supported by numerical models of the T32 encounter. Hybrid simulations by Müller et al. (2010) put a lower limit of  $\sim 25$  min on the lifetime of fossilized magnetic fields, whereas MHD simulations by Ma et al. (2009) and Snowden et al. (2011b) estimated lifetimes of  $\sim 2$  h and  $\sim 50$  min, respectively. Simon et al. (2010) also speculated that the lifetime of fossilized fields may even further exceed these values in Titan's wake region due to the prolonged transport times through Titan's diffusion dominated region.

Despite the impact of the variability in the upstream plasma conditions on the inner region of Titan's induced magnetosphere, the influence on the large scale structures of Titan's induced magnetosphere was found to be weaker than expected. Ulusen et al. (2012) compared Cassini observations from nine Titan flybys against the results of an MHD simulation and suggested that the magnetic perturbations of Titan's plasma interaction can be divided into two layers: up to an altitude of 1800 km the induced magnetic field perturbations are generally in agreement with a steady-state draping of the average ambient magnetic field. Below that altitude, the observations show strong deviations from the steady-state draping picture due to fossilized fields and effects of neutral winds. These findings were later supported by the study of Simon et al. (2013) who also investigated the robustness of Titan's induced magnetosphere against the magnetospheric variabilities of the upstream magnetic field based on a much larger dataset. They found that for most flybys the magnetic measurements can be understood by the draping of an average magnetic background field around Titan's ionosphere. For cases where this picture was not applicable they found that the moon's induced magnetosphere was obscured by magnetospheric perturbations.



## 3 Simulation Model

In this chapter we describe the main features of the simulation model. In section 3.1 we give a brief overview of different model approaches and describe the main equations of the hybrid simulation code A.I.K.E.F. (Adaptive-Ion-Kinetic-Electron-Fluid) which is used in this thesis. A brief overview of the numeric details of our hybrid code is given in section 3.2. We discuss the implementation of Titan's ionosphere and the chemistry network into our model in section 3.3. We finish with an overview of other numerical simulation studies of Titan's plasma interaction that have been presented in the past in section 3.4.

### 3.1 Hybrid Model A.I.K.E.F.

There are several ways to perform numerical simulations of the plasma interaction of a planet/moon with an impinging plasma. Table 3.1 gives an quick impression of the conceptual differences between the main model approaches that have been developed in the past. The simplest approach to numerical plasma simulations is a pure magnetohydrodynamic (MHD) model, where the plasma is represented by a single fluid with average parameters. This approach allows the use of a very high grid resolution due to the low demanding computational costs. Also the description of plasma-neutral interactions such as collisions are very straightforward as they can easily be included as a loss term in the momentum equation. However, asymmetries due to large gyro radii of ions can not be included with this approach. In the next step, an MHD model can be improved by including multiple continuity equations, to form a multi species MHD code. This allows for a very detailed description of ion-neutral chemistry, but ion effects are still neglected by the use of a single equation for the bulk velocity. This problem is solved by the multi-fluid approach, where each plasma species is represented with its own continuity and momentum equation. Thus, asymmetries due to different ion species with different masses can be resolved. Multi fluid codes are also not very computationally demanding and can therefore be used to simulate a planet's magnetosphere and a moon in the same box. However, multi fluid models cannot simulate non-Maxwellian particle distributions which may be important in Saturn's outer magnetosphere.

The hybrid approach combines parts of the advantages of a full particle approach and the simplicity of a fluid approach by representing ions as kinetic particles, while treating electrons as a fluid. By solving the equations of motion for the ions, the hybrid approach can resolve non-Maxwellian particle distributions and naturally the effects of the velocity shear of different ion species. Also the inclusion of negatively charged ion species is possible, such as the negatively charged dust grains near Enceladus. However, this

	Fluid Models		Kinetic Models	
Single Fluid	Single Fluid	Multi Fluid	Hybrid Model	Full Particle
Single species (MHD)	Multi Species	Multi Species	Kinetic Ions Electron Fluid	Kinetic Ions Kinetic Electrons
- Ion effects	- Ion effects	(+) Ion effects	+ Ion effects	+ Ion effects
+ Computational cost	+ Computational cost	+ Computational cost	- Computational cost	+ Electron effects -- Computational cost

**Table 3.1:** Main conceptual differences, strengths and weaknesses of various modeling approaches for numerical plasma simulations.

semi-kinetic approach is computationally very demanding, since the phase-space  $(\underline{x}, \underline{v})$  of millions of macroparticles needs to be stored. Therefore, a hybrid code is usually restricted to a coarser grid resolution compared to a fluid approach. A full particle model treats both ions and electrons as kinetic particles under the influence of external forces. By using the complete set of Maxwell equations, this approach is able to cover the complete physics without the use of simplifying approximations. However, the computational cost of managing the phase space of ions and electrons is exceptional. Also the description of particle interactions (especially chemical reactions) is not easily possible in a comparable straightforward manner as it is for fluid codes. Because this approach resolves electron dynamics, which have generally much smaller characteristic scales than ions, a full particle code would also take too much time to complete a simulation of e.g. Titan's plasma interaction. In addition, resolving the effects of electron dynamics is often not necessary for the majority of celestial bodies, since the ion dynamics dominate the plasma interaction, especially at Titan.

In this thesis, we use the hybrid simulation code A.I.K.E.F. (Müller et al. 2011), which treats ions as particles, while electrons act as a massless, charge-neutralizing fluid. The hybrid approach therefore enables plasma simulations to cover kinetic effects of individual particles, such as the asymmetries associated with large ion gyro radii and different flow patterns of light and heavy plasma constituents. Thus, the hybrid approach is particularly suitable to study the unusual ion tail structures seen during T9, T63 and T75.

In the following we will derive the main hybrid equations of the A.I.K.E.F. code. Note that this code and its underlying equations and numerical mechanisms have been extensively described in previous studies, e.g. Bagdonat (2005), Simon (2007), Kriegel (2014), Müller et al. (2011). For an in depth description of the numerical details we refer the reader to those works. The hybrid model which we use is based on three main assumptions:

- The mass of electrons is neglected,

$$m_e = 0 \quad . \quad (3.1)$$

- The plasma is assumed to be quasi-neutral, i.e,

$$en_e = \sum_s^N q_s n_s \quad . \quad (3.2)$$

For a plasma of  $s = 1, \dots, N$  ion species with charge  $q_s$ , density  $n_s$  and electron density  $n_e$ . In this thesis we only use single charged positive ions.

- The Darwin-Approximation (Bagdonat 2005) is used, where the displacement currents are neglected  $0 \approx \frac{1}{c^2} \frac{\partial \underline{E}}{\partial t}$ . Ampères law then becomes

$$\nabla \times \underline{B} = \mu_0 \underline{j} \quad . \quad (3.3)$$

These assumptions place several constraints on the validity of the model. The quasi-neutrality condition demands that the characteristic length scales are larger than the Debye length  $\lambda_D$  of the plasma and the characteristic frequencies to be smaller than the plasma frequency  $\omega_{pe}$ . These conditions are always fulfilled in the vicinity of Titan (see table 2.3). By neglecting the electron mass we allow for the treatment of the electrons as a massless fluid, which leads to a simple equation for the calculation of the electric field (see below). This assumption is justified because the characteristic scales of electrons are much smaller than those of the ions, meaning that electrons are able to adapt to ion dynamics without a noticeable inertial delay. By neglecting displacement currents in Ampères law, we simply demand that the characteristic speeds of the system are much smaller than the speed of light. In a space plasma the characteristic speed is given by the Alfvén velocity, which is at maximum on the order of hundreds km/s.

Since it is computationally not possible to store the phase space coordinates of the  $\sim 10^{27}$  real individual particles (assuming a total ion density of  $0.3 \text{ cm}^{-3}$  in a  $(10 R_T)^3$  simulation box), the hybrid model treats the ions as macroparticles with the same mass-to-charge ratio as the real individual particles. The motion of these particles is therefore governed by the Lorentz force arising from the electromagnetic fields  $\underline{E}$  and  $\underline{B}$ , with equations of motion that read:

$$\frac{d\underline{x}_j}{dt} = \underline{v}_j \quad , \quad \frac{d\underline{v}_j}{dt} = \frac{q_j}{m_j} (\underline{E} + \underline{v}_j \times \underline{B}) \quad , \quad (3.4)$$

where  $\underline{x}_j$ ,  $\underline{v}_j$ ,  $m_j$  and  $q_j$  denote the position, velocity, mass and charge of a single macroparticle.

With the assumption of negligible electron inertia (electron mass  $m_e \approx 0$ ) as well as an isotropic electron pressure, the electron momentum equation reads

$$0 = -(\underline{E} + \underline{u}_e \times \underline{B}) - \frac{1}{en_e} \nabla P_e + \eta \underline{j} \quad . \quad (3.5)$$

In this equation,  $\underline{u}_e$ ,  $n_e$  and  $P_e$  are the electron bulk velocity, electron number density and electron pressure, respectively. The last term describes the diffusion of electromagnetic fields through a medium of finite resistivity  $\eta$  (such as Titan's body). We introduce the charge-averaged ion quantities

$$\underline{u}_i = \frac{\sum_j q_j n_j \underline{u}_j}{en_e} \quad \text{and} \quad \rho_{c,i} \equiv en_e = \sum_j q_j n_j \quad , \quad (3.6)$$

where the summation is carried out over all positive ion species, and  $\underline{u}_j$  and  $n_j$  denote the bulk velocity and number density of the respective ion species. Using the definition of the current density,  $\underline{j} = -en_e\underline{u}_e + \sum_j q_j n_j \underline{u}_j$ , as well as Ampère's law,  $\nabla \times \underline{B} = \mu_0 \underline{j}$ , one can derive an expression for the electric field from Equation (3.5):

$$\underline{E} = -\underline{u}_i \times \underline{B} + \frac{(\nabla \times \underline{B}) \times \underline{B}}{\mu_0 \rho_{c,i}} - \frac{\nabla P_e}{\rho_{c,i}} + \frac{\eta}{\mu_0} \nabla \times \underline{B} \quad , \quad (3.7)$$

where  $\rho_{c,i}$  is the total charge density of the ions. For the electron pressure we use an adiabatic equation of state given by

$$P_e = P_{e,0} \left( \frac{n_e}{n_{e,0}} \right)^\kappa \quad , \quad (3.8)$$

with the adiabatic exponent  $\kappa = 2$ , representing two degrees of freedom for electrons in a magnetized plasma (Bößwetter et al. (2004)). The quantities  $P_{e,0}$  and  $n_{e,0}$  are background parameters describing the undisturbed upstream plasma. An adiabatic description of the electrons had also been applied in the hybrid models of Modolo et al. (2007a) and Lipatov et al. (2012), who successfully described aspects of the split signatures detected during T9. By applying Faraday's law to the electric field equation, one obtains an expression for the time evolution of the magnetic field

$$\frac{\partial \underline{B}}{\partial t} = \nabla \times (\underline{u}_i \times \underline{B}) - \nabla \times \left( \frac{(\nabla \times \underline{B}) \times \underline{B}}{\mu_0 \rho_{c,i}} \right) + \nabla \times \left( \frac{\eta}{\mu_0} \nabla \times \underline{B} \right) \quad , \quad (3.9)$$

where the electron pressure term vanishes in this equation due to the adiabatic description (Simon et al. (2007a)). Negatively charged ions that may occur in Titan's ionosphere (Coates et al. (2007a)) are not included in this model.

## 3.2 Numerical Implementation

In the following we will briefly describe some of the main numerical aspects of A.I.K.E.F. This code is based on the 'Braunschweig' code which was developed by Bagdonat (2005) and subsequently improved by the works of Simon (2007) and Müller et al. (2011) into the version used in this thesis.

A.I.K.E.F. operates on Cartesian coordinates and uses an un-staggered grid. The computational domain can be refined in order to improve the grid resolution near locations of interest. This is achieved by the separation of the underlying grid structure into equally sized 'root' blocks (level 0). Each root block then consists of eight octants. If a certain region of a root block is supposed to be refined to a higher resolution (level 1), the octants that cover that region become the new root blocks of the next higher refinement level. The octants of the new root blocks thus then have twice the resolution compared to the level below. The code theoretically supports an arbitrary number of refinement levels, however, for Titan plasma simulations more than two levels of refinement proved to not be beneficial to the duration of simulation runs. A.I.K.E.F. also supports an adaptive mesh refinement routine, i.e., an on-the-fly adaptation of the local grid resolution that can be triggered by various parameters (e.g. the average number density of an octant). However,

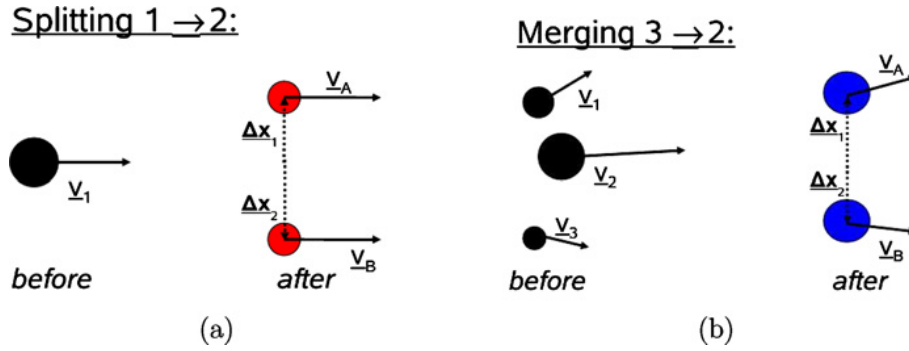


**Figure 3.1:** Details of the splitting (a) and merging (b) mechanisms of particles in A.I.K.E.F. to ensure an approximately constant number of particles in each cell for all refinement levels. In order to conserve momentum, three particles are merged to form two new particles. The new particles are dislocated from their partners by a small (random) distance  $\Delta x$  for both splitting and merging procedures. Figure from Müller et al. (2011).

in this thesis we always use a hierarchical mesh refinement where the region of increased resolution is fixed from the start of the simulation (usually the near vicinity of the Titan obstacle). The code is parallelized with the Message Parsing Interface (MPI). Each CPU process handles all calculations of its assigned root blocks (or refined blocks). The number of assigned blocks per process is checked and balanced after a certain amount of simulation steps in order to maintain a reasonable workload on the processes.

A.I.K.E.F. is a *Particle-in-cell* code, where the ion macroparticles move freely inside the grid cells and the macroscopic physical quantities ( $\underline{E}$ ,  $\underline{B}$ ,  $\underline{U}$ ,  $\rho$ ) are calculated only on the mesh nodes itself. The contribution of a macroparticle at a certain position inside a mesh cell to the bulk velocity and charge density on each of the eight cell corners is extrapolated with the *Cloud-in-Cell* method. In this method the volume that is defined by the corner mesh node and the position of the macroparticle is used to weight that particles contribution to the quantities on the cell corner mesh node. The same method is then used to retroactively calculate the electromagnetic fields at the particles position in order to derive the local Lorentz force.

The mesh refinement of root blocks into child blocks with increased resolution also requires additional procedures for the particle management: the eight newly created child blocks cover the same volume as their parent, thus they also contain the same number of particles. This means that the number of particles per cell is reduced by a factor of eight for each refinement level. In order to avoid having nearly empty cells in the domain, particles that cross the boundaries between refinement levels are therefore subject to splitting and merging (see figure 3.1). This mechanism ensures that the number of particles in each grid cell is centered around a fixed number. Particles that enter a cell with a higher level of refinement are split into two particles. If the number of particles exceeds the optimal value in a cell, three particles are merged into two new particles. Each ion macroparticle has a certain weight that indicates the number of real particles that it represents. The weight of the macroparticles after splitting and merging is adjusted accordingly to keep the number of represented total particles constant.

The electromagnetic fields are advanced in time via several mechanisms. The electric

field is advanced by using the *Current-Advancement-Method* (Matthews 1994). For the magnetic field, the convective term and the Hall term are advanced by a time-explicit, second-order cycling leap frog algorithm (see section 4.3.1 in Bagdonat (2005)). For the diffusion term of the magnetic field, this treatment is not suitable due to the large gradients of the resistivity  $\eta$  that may arise at the inner boundary between the obstacle and the surrounding space. An implicit algorithm is applied for the magnetic diffusion term instead, which is solved via a *Successive-Over-Relaxation* (SOR) scheme.

Due to the use of an un-staggered mesh for the electromagnetic fields, an additional 'divergence cleaning' method is required in order to fulfill  $\nabla \cdot \underline{B} = 0$ . This is achieved by solving Poisson's equation for the (purely numerical) potential of the magnetic field  $\phi_B$ ,

$$\Delta^2 \phi_B = -\nabla \cdot \underline{B} \quad (3.10)$$

with a SOR scheme. The divergence-free magnetic field can then be obtained in the code by correcting the numerical field  $\underline{B}$  via

$$\underline{B}_{corrected} = \underline{B} + \nabla \phi_B \quad (3.11)$$

The numerical stability of the code is mainly affected by the Courant-Friedrichs-Lewy criterion, which states that no information should travel faster than one mesh cell in a single simulation step  $\Delta t$ . This means effectively that the timestep has to be chosen such that no particle can travel through a single grid cell in one step. For the Titan simulations performed for this thesis, choosing a time step that is between  $0.0001 \cdot \Omega_g^{-1}$  to  $0.001 \cdot \Omega_g^{-1}$  (with  $\Omega_g^{-1}$  the inverse gyro frequency of the upstream plasma) proved to be sufficient to ensure this criterion.

### 3.3 Titan ionosphere model

The model for the ionosphere of Titan used in this thesis has been drastically improved compared to the one used in preceding studies (e.g., Simon et al. (2006b, 2007c), Müller et al. (2010)) in several important respects. We describe Titan's ionosphere with a seven-species model, considering the same components as the MHD model by Ma et al. (2004, 2006) and the hybrid model by Ledvina et al. (2012). The model covers masses from 2-74 amu and accounts for the fact that the complex ion-neutral chemistry in Titan's ionosphere produces a vast number of different ion species, which are found to cluster around several distinct mass values (Cravens et al. (2006)). An overview of the species included in the model is given in Table 3.2. The most abundant ion species observed in Titan's upper ionosphere ( $> 1000$  km),  $C_2H_5^+$  and  $HCNH^+$  (Krasnopolsky (2009)) are each represented by a separate model ion species.

In each time step, ions of the first three model species ( $L^+$ ,  $M^+$ ,  $H1^+$ ) are added to the ionosphere in the simulation according to their total ion production rates, taking into account photoionization and impact ionization by magnetospheric electrons. We use the EUVAC model developed by Richards et al. (1994) to calculate realistic photoionization rates for these species. The EUVAC model provides wavelength-dependent solar UV radiation intensities at 1 AU,  $I_{Earth}(\lambda_i)$ , in the range of 50-1000Å. The Solar flux at the topside of Titan's atmosphere  $I_{Saturn}(\lambda_i)$  is obtained by scaling of the EUVAC flux according to

Model species name	Physical composition	Mass	Mass range
L <sup>+</sup>	H <sup>+</sup> , H <sub>2</sub> <sup>+</sup>	2	1-2
M <sup>+</sup>	CH <sub>5</sub> <sup>+</sup> , CH <sub>4</sub> <sup>+</sup> , CH <sub>3</sub> <sup>+</sup> , CH <sub>2</sub> <sup>+</sup> , CH <sup>+</sup> , C <sup>+</sup> , N <sup>+</sup>	14	12-17
H1 <sup>+</sup>	C <sub>2</sub> H <sub>5</sub> <sup>+</sup>	29	29
H2 <sup>+</sup>	HCNH <sup>+</sup>	28	28
MHC <sup>+</sup>	C <sub>3</sub> H <sup>+</sup> , C <sub>3</sub> H <sub>2</sub> <sup>+</sup> , C <sub>3</sub> H <sub>3</sub> <sup>+</sup> , C <sub>3</sub> H <sub>4</sub> <sup>+</sup> , C <sub>3</sub> H <sub>5</sub> <sup>+</sup> , C <sub>4</sub> H <sub>3</sub> <sup>+</sup> , C <sub>4</sub> H <sub>5</sub> <sup>+</sup>	44	37-53
HHC <sup>+</sup>	C <sub>5</sub> H <sub>3</sub> <sup>+</sup> , C <sub>5</sub> H <sub>5</sub> <sup>+</sup> , C <sub>5</sub> H <sub>7</sub> <sup>+</sup> , C <sub>5</sub> H <sub>9</sub> <sup>+</sup> , C <sub>6</sub> H <sub>5</sub> <sup>+</sup> , C <sub>6</sub> H <sub>7</sub> <sup>+</sup> , C <sub>7</sub> H <sub>5</sub> <sup>+</sup>	70	63-89
HNI <sup>+</sup>	C <sub>3</sub> H <sub>2</sub> N <sup>+</sup> , C <sub>5</sub> H <sub>5</sub> N <sup>+</sup> , C <sub>3</sub> HN <sup>+</sup>	74	51-79

**Table 3.2:** Ionospheric species used in the model with respective mass of the species in the code and the mass range of the corresponding physical species. Species which possess similar mass are grouped into a single species. Based on Ma et al. (2004).

the distance of Saturn to the Sun,  $d(\text{Saturn})$  (in astronomical units), by

$$I_{\text{Saturn}}(\lambda_i) = I_{\text{Earth}}(\lambda_i) \frac{1}{d(\text{Saturn})^2} . \quad (3.12)$$

This wavelength interval is divided into 37 wavelength bins and the intensity of the solar flux is scaled to account for the variability of the solar activity in the solar cycle. Our model includes three neutral species that are used for photoionization: H<sub>2</sub>, CH<sub>4</sub> and N<sub>2</sub>. The density profiles of these main components of Titan's neutral atmosphere are adopted from Cui et al. (2009) (see figure 3.2) and are assumed to be spherically symmetric. In the hybrid code, the main neutral densities are implemented via barometric equations  $n(z) = n_0 \exp(-z/H)$ , where  $n_0$  is the density at the surface and  $H$  is the scale height of the species:

$$n_{\text{N}_2}(z) = 3.21 \cdot 10^{22} \exp\left(-\frac{2575}{66.3}r\right) \quad [m^{-3}] \quad (3.13)$$

$$n_{\text{CH}_4}(z) = 1.06 \cdot 10^{19} \exp\left(-\frac{2575}{90.6}r\right) \quad [m^{-3}] \quad (3.14)$$

$$n_{\text{H}_2}(z) = \begin{cases} 5.82 \cdot 10^{19} \exp\left(-\frac{2575}{69.8}r\right), & z \leq 0.4757 \\ 5.82 \cdot 10^{19} \exp\left(-\frac{2575}{297.6}r\right), & z > 0.4757 \end{cases} \quad [m^{-3}] \quad (3.15)$$

Close to Titan, N<sub>2</sub> and CH<sub>4</sub> dominate the neutral atmosphere, however at high altitudes (~ 2000 km), hydrogen becomes the dominant species due to its large scale height ( $H_{\text{H}_2} \sim 300$  km compared to  $H_{\text{N}_2, \text{CH}_4} \sim 70 - 90$  km). Note that the regions below an altitude of 900 km are not important for Titan's plasma interaction since the plasma transport is not convection dominated there and thus it is sufficient to cover the upper altitudes with a precise neutral density profile only. Photoionization of H<sub>2</sub> is associated with the L<sup>+</sup> species, of CH<sub>4</sub> with the M<sup>+</sup> species and of N<sub>2</sub> with the H1<sup>+</sup> species. It is crucial to understand that this is justified because, as we have stated in section 2.2, in reality the photoionized main neutrals N<sub>2</sub> and CH<sub>4</sub> are rapidly converted into those species anyway by the chemistry.

All three neutral species are assumed to attenuate the solar flux in Titan's atmosphere by

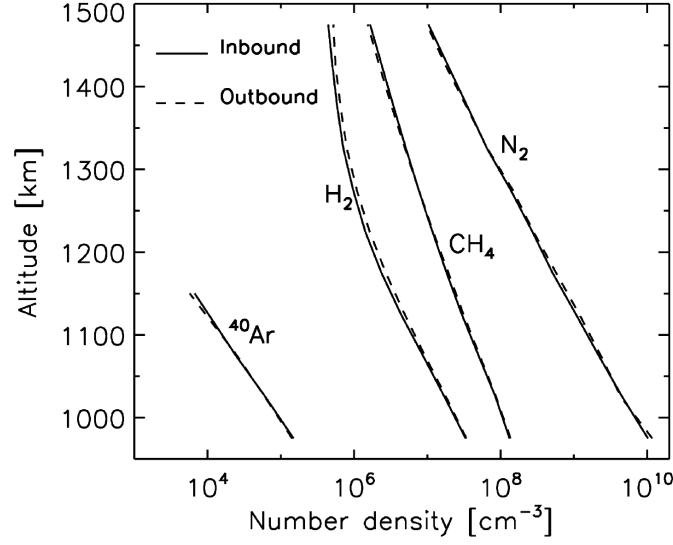


**Figure 3.2:** Average density profiles of  $N_2$ ,  $CH_4$  and  $H_2$  between 950 and 1500 km. The profiles are averaged over 15 close encounters of Cassini and measured by the Ion-Neutral-Mass-Spectrometer (INMS). The altitude profiles are used in our model. Figure from Cui et al. (2009).

absorption of solar radiation. The total photoionization production rate  $P_{ph,j}(\underline{x}_0)$  for ion species  $j = \{L^+, M^+, H1^+\}$  at a position  $\underline{x}_0$  in Titan's upper atmosphere is therefore given by

$$P_{ph,j}(\underline{x}_0) = \sum_{i=1}^{37} \sigma_{ion,n}(\lambda_i) n_n(\underline{x}_0) I_{Saturn}(\lambda_i) \exp[-\tau(\underline{x}_0, \lambda_i)] \quad , \quad (3.16)$$

where we have introduced the optical depth

$$\tau(\underline{x}_0, \lambda_i) = \sum_n \sigma_{abs,n}(\lambda_i) \int_{\infty}^{\underline{x}_0} n_n(s) d\underline{s} \quad , \quad (3.17)$$

and  $\sigma_{ion,n}$ ,  $\sigma_{abs,n}$  and  $n_n$  denote the photoionization and absorption cross-sections and the density of the respective neutral species  $n = \{H_2, CH_4, N_2\}$ . The integration in equation (3.17) is carried out along the path element  $d\underline{s}$ , which is along the straight line from the sun to  $\underline{x}_0$ . The wavelength dependent photoabsorption and photoionization cross-sections are taken from Schunk and Nagy (2009). This method precisely describes the photoionization of Titan's atmosphere. It accounts for the local time and seasonal dependency of the location of the subsolar point and produces realistic ion production rates in the region around the terminator, in contrast to our preceding model (e.g., Simon et al. (2006b)). In the geometric shadow of Titan, the photoionization is zero. Thus, the ion production due to solar radiation is of a bowl-like shape and possesses rotational symmetry around the Sun-Titan line.

The model considers another source of ions for the ( $L^+$ ,  $M^+$ ,  $H1^+$ ) species associated with impact ionization by magnetospheric electrons. The respective ionization rates are taken from Ledvina et al. (2012) and added to the photoionization rate. According to the resulting production rates, ions are injected into the simulation during each time step.

Reaction	$k_{in}$ [ $10^{-10}$ cm <sup>3</sup> /s]
$\text{CH}_5^+ + \text{C}_2\text{H}_4 \rightarrow \text{C}_2\text{H}_5^+$	15.0
$\text{C}_2\text{H}_5^+ + \text{HC}_3\text{N} \rightarrow \text{HC}_3\text{NH}^+$	36.0
$\text{CH}_5^+ + \text{C}_2\text{H}_6 \rightarrow \text{C}_2\text{H}_5^+$	2.0
$\text{HCNH}^+ + \text{C}_4\text{H}_2 \rightarrow \text{C}_4\text{H}_3^+$	1.8
$\text{N}^+ + \text{CH}_4 \rightarrow \text{HCNH}^+$	4.0
$\text{HCNH}^+ + \text{HC}_3\text{N} \rightarrow \text{HC}_3\text{NH}^+$	34.0
$\text{CH}_3^+ + \text{CH}_4 \rightarrow \text{C}_2\text{H}_5^+$	11.0
$\text{C}_3\text{H}_5^+ + \text{C}_2\text{H}_2 \rightarrow \text{C}_5\text{H}_5^+$	3.8
$\text{C}_2\text{H}_5^+ + \text{HCN} \rightarrow \text{HCNH}^+$	27.0
$\text{C}_3\text{H}_3^+ + \text{C}_2\text{H}_4 \rightarrow \text{C}_5\text{H}_5^+$	5.5
$\text{C}_2\text{H}_5^+ + \text{C}_2\text{H}_2 \rightarrow \text{C}_3\text{H}_3^+, \text{C}_4\text{H}_5^+$	1.9
$\text{C}_4\text{H}_3^+ + \text{C}_4\text{H}_2 \rightarrow \text{C}_6\text{H}_3^+$	7.4
$\text{C}_2\text{H}_5^+ + \text{C}_2\text{H}_4 \rightarrow \text{C}_3\text{H}_5^+$	3.5

**Table 3.3:** Ion-neutral reactions included in the model. Rate constants  $k_{in}$  are taken from Krasnopolsky (2009) and Vuitton et al. (2007).

All other ionospheric species are generated solely as a result of ion-neutral reactions (see Table 3.3). The ion-neutral interactions which are considered by our model include elastic collisions of the impinging magnetospheric plasma with Titan's three main neutral species ( $\text{N}_2$ ,  $\text{CH}_4$ ,  $\text{H}_2$ ), as well as the most important ion-neutral chemical reactions in the ionosphere. The elastic collision rates  $\nu_{in}$  are calculated by

$$\nu_{in} = \frac{2.7 \cdot 10^{-9} n_n (\alpha_n \mu_{in})^{0.5}}{m_i}, \quad (3.18)$$

where we apply  $\alpha_{\text{H}_2} = 0.82$ ,  $\alpha_{\text{CH}_4} = 2.59$  and  $\alpha_{\text{N}_2} = 1.76$  as the neutral polarizability parameters (Schunk and Nagy (2009)). The parameter  $\mu_{in}$  is the reduced mass of the reaction partners and  $m_i$  is the mass of the involved ion species.

The ion-neutral reactions which produce the other species in the ionosphere and their respective rate constants  $k_{in}$  are listed in Table 3.3. For any reactions that include a neutral species other than  $\text{H}_2$ ,  $\text{CH}_4$  or  $\text{N}_2$ , we assume a constant ratio  $\eta_n = n_n/n_{\text{CH}_4}$  of the respective species and  $\text{CH}_4$  in order to be able to calculate the process rate  $\nu_{in} = k_{in}n_n$  of the reaction. These minor species are only needed for the calculation of the chemical reactions and do not possess a fine structure (e.g. a local maximum) in their density profile above 900 km altitude. The mixing ratios of the minor neutral species are estimated from the density profiles given by Ledvina et al. (2012).

The numerical realization of the chemical reactions is done in a purely statistical way, with the method introduced by Kriegel et al. (2011). A detailed description of the numerical mechanism for the chemical reactions is provided in that preceding work. During each time step, reaction probabilities for every particle in the simulation are calculated. The reaction probabilities are related to the lifetime of a particle: the lifetime of an ion, i.e. the time between two reactions, is a random variable which obeys an exponential distribution. The probability that a particle does *not* undergo a reaction for the next time

interval  $t$  is given by

$$P(t) = \exp\left(-\frac{t}{\tau_{in}}\right) \quad , \quad (3.19)$$

where  $\tau_{in}$  is the average time between two reactions. The probability that a particle will undergo a reaction during the next time interval  $\Delta t$  is therefore related to the reaction rate  $\nu_{in} = 1/\tau_{in}$  and given by  $p\Delta t$ , where

$$p = \frac{d}{dt}(1 - P(t))|_{t=0} = \nu_{in} = k_{in}n_n \quad . \quad (3.20)$$

In the numerical model, the product  $p\Delta t$  is then compared against a random number  $r$  between 0 and 1 to decide if a reaction occurs (reaction:  $p\Delta t > r$ , no reaction:  $p\Delta t < r$ ). This approach requires the timestep  $\Delta t$  to be such that  $p\Delta t$  is much smaller than 1. If this conditions is not fulfilled, the method is not implemented correctly.

During a reaction, an ion of the original species is removed from the simulation and replaced by an ion of the product species. New ions are initialized with the velocity of the neutral reaction partner, which we assume to have a temperature of 150 K in our simulations. No bulk velocity of the neutral species is assumed in our model. Since these neutral velocities ( $\sim 1$  km/s) are negligible compared to the plasma velocities ( $\sim 100$  km/s), the chemical reactions as well as collisions effectively slow the overall plasma down. If an elastic collision occurs, the ion remains in the simulation and its velocity is changed to that of the neutral species.

## 3.4 Other Titan simulation models

A number of different simulation models have been developed in the past by several groups in order to describe various aspects of Titan's plasma interaction. These models cover almost the full spectrum of different numerical approaches presented in table 3.1, apart from full-particle codes.

A single fluid, multi species MHD code was developed by Ma et al. (2004). This model introduced the basics of the 7-species representation of Titan's ionosphere that is also used in our model. However since all the ion species share the same bulk velocity, the asymmetries in Titan's plasma interaction due to ion gyration effects can not be resolved by this model. The model was applied to study Titan's plasma interaction during the first two Cassini Titan flybys TA and TB (Ma et al. 2006), as well as the T9 flyby (Ma et al. 2007). Simulations of the plasma interaction during the T32 encounter of Cassini confirmed the existence of fossilized magnetic fields in Titan's ionosphere Ma et al. (2009). Ma et al. (2011) further developed their model by introducing a two-fluid approach for electrons and ions in order to include electron thermal heating processes in Titan's ionosphere.

Snowden et al. (2007) developed a simple multi fluid code for Titan's plasma interaction. Their code is therefore able to resolve the asymmetric effects of ion gyration near Titan. Snowden et al. (2007) applied their model to simulate Titan's plasma interaction during the TA, TB and T3 encounters of Cassini and found a good agreement of their simulation results with Cassini magnetic observations. By taking advantage of the computational abilities of fluid codes, Snowden (2010) embedded the local Titan interaction model into a global multi-scale model of Saturn's magnetosphere. Using this global model Snowden

et al. (2011a) investigated the variability of Titan plasma environment when it is located in the pre noon sector at 9 Saturn local time for the cases of a stationary, inward moving and outward moving magnetopause. They found indications that Titan's presence may be able to hinder Saturn's magnetopause from crossing over Titan's orbital location in this sector. By using time-dependent solar wind conditions in their global model, Snowden et al. (2011b) studied Titan's interaction during the magnetopause crossing of the T32 encounter and found similar constraints on the timescales (50 min to 2 h) of fossilized magnetic fields in Titan's ionosphere as other studies. An improved version of the multi fluid code that includes electron impact ionization, ion neutral collisions and ion recombination was used by Snowden and Winglee (2013) to simulate Titan's plasma interaction during the T55 flyby. They showed that electron impact ionization was necessary to explain observed electron densities on the night side of the moon and also suggested that the impinging plasma flow on Titan contained a strong radially outward pointing component during T55 instead of a corotational direction. Snowden et al. (2013) combined their model with a two-stream electron transport model to study the energy deposition into Titan's ionosphere by magnetospheric electrons that precipitate along the draped field lines. They found that the total power deposited by magnetospheric electrons is about an order of magnitude less than the power deposited by solar EUV radiation during the solar minimum around 2008, confirming the sun as the major source of input energy for Titan's ionosphere.

Ledvina et al. (2012) applied a hybrid model that includes the major chemical reactions and ion-neutral collisions of Titan's ionosphere in order to investigate the effect on Titan's plasma interaction caused by the orientation of the day side ionosphere with respect to the incident magnetospheric plasma flow. These authors found Titan's ionosphere to be always in a state of photochemical equilibrium at altitudes below 1200 km regardless of illumination angle. In addition, they found that the ion outflow and magnetic field structures of Titan's induced magnetosphere are highly robust against changes of the illumination angle. Ledvina and Brecht (2012) included negative ions to their ionosphere model. They found that negative ion pickup may be detectable by spacecraft observations, however Titan's induced magnetosphere structure is not affected in a significant way.

Other hybrid models have been applied to study Titan's plasma interaction during the Voyager 1 encounter (Brecht et al. 2000, Kallio et al. 2004, Sillanpää et al. 2007) as well as the Cassini's TA flyby (Modolo and Chanteur 2008, Lipatov et al. 2014), where the model results generally showed agreement with the observational data. Hybrid models were also applied to study aspects of Titan's plasma interaction during the T9 flyby (these are described in section 4.1).

The hybrid code A.I.K.E.F. in its previous versions has been used in preceding studies for a wide range of plasma interaction scenarios throughout the solar system. Titan's plasma interaction has been the subject of the majority of these studies. The first modeling of Titan's plasma interaction with A.I.K.E.F. was done by Simon et al. (2006b), who studied the general structure of the Titan's induced magnetosphere for different orbital locations and upstream Mach numbers. In this work Titan's ionosphere and the upstream magnetospheric plasma each were represented by a single ion species. Simon et al. (2007b) extended their Titan ionosphere model to multiple upstream and ionospheric species, with Titan's ionosphere being represented by photoionized H<sub>2</sub>, CH<sub>4</sub> and N<sub>2</sub>, and compared their model results with their previous one species model. Simon et al. (2007c) also ap-

plied their model to the T9 flyby of Cassini (see section 4.1). Simon et al. (2008b) were able to reproduce key features of the observed magnetic field signatures during the T34 encounter. Titan's response to time-dependent changes of the magnitude and direction of the upstream magnetic field was studied by Simon et al. (2008a), where they showed that the asymmetric features of Titan's magnetotail cannot develop under the distorted upstream conditions. The reconfiguration of Titan's induced magnetosphere during the crossing of Saturn's magnetopause throughout the T32 encounter was studied in real-time by Simon et al. (2009a). Using a hierarchical grid that permits a higher resolution in Titan's ionosphere, the fossilization of the magnetic field in the moon's ionosphere during this encounter was studied by Müller et al. (2010). Titan's interaction with the supersonic solar wind was analyzed by Simon (2009). Simon and Motschmann (2009) studied the asymmetries of Titan's induced magnetosphere as a function of the moon's distance to Saturn's magnetodisk current sheet. They showed that non-perpendicular upstream geometries of the bulk velocity and magnetic field induce additional asymmetries to Titan's magnetotail structures.

A.I.K.E.F. was also applied to study the plasma interactions of numerous other Saturnian moons visited by Cassini, e.g., Tethys (Simon et al. (2009b)), Rhea (Roussos et al. 2008, Simon et al. 2012), and Dione (Krupp et al. 2013). Kriegel et al. (2011, 2014) also included the effects of negatively charged dust grains on the plasma flow, which proved to be essential for the description of Enceladus's dusty plasma interaction. Outside the Saturnian system, the hybrid code was successfully applied to the study aspects of the plasma interactions of magnetized asteroids (Simon et al. 2006a), Mars (Simon et al. 2007a, Bößwetter et al. 2007, Boesswetter et al. 2009, 2010) and Mercury (Müller et al. 2012).

## 4 Split Signatures in Titan's tail

The following chapter has been published in wide parts before submission of the thesis. The copyright holder of the pre-publication is Elsevier, and the cited parts are reprinted with permission. The publication can be found under the following reference:

**Feyerabend, M.**, Simon, S., Motschmann, U., Liuzzo, L., 2015, Filamented ion tail structures at titan: A hybrid simulation study, *Planetary and Space Science*, 117, 362-376, ISSN 0032-0633, <http://dx.doi.org/10.1016/j.pss.2015.07.008>

### 4.1 Introduction

Since its arrival at Saturn in 2004, the Cassini spacecraft has performed more than 100 flybys of Titan. Most of these flybys were aimed to pass Titan at low altitudes within  $1 R_T$  to study its ionospheric structure. The number of flybys which actually passed through Titan's tail, i.e., the population of pickup ions and/or the magnetic wake downstream of Titan, with a closest approach altitude (C/A) larger than  $1 R_T$  is much smaller. Simon et al. (2014) identified 19 encounters that are potentially suitable to study Titan's plasma tail at intermediate altitudes between  $1 R_T$  and  $5 R_T$ .

One interesting finding of the mid-range tail flybys were the so-called '*split signatures*' (Coates et al. (2007b), Modolo et al. (2007b)), during the T9 (C/A at  $4 R_T$  on 26 December 2005), T63 (C/A at  $1.9 R_T$  on 12 December 2009) and T75 (C/A at  $3.9 R_T$  on 19 April 2011) encounters (Coates et al. 2012). This term denotes the subsequent detection of two spatially separated regions downstream of Titan that are populated by cold pick-up ions. The detection of the split signatures was surprising, since it was expected that Cassini flybys that penetrate through Titan's downstream tail region would show at maximum one signature of escaping ions that originate from Titan's ionosphere. The trajectories of these flybys, with indications of the location of the split signatures, are shown in Figure 4.1.

Ion and electron spectra presented for T9 by Coates et al. (2007b), Szego et al. (2007) and Modolo et al. (2007b) showed the detection of cold ions and electrons of ionospheric origin in two spatially separated segments along the T9 trajectory (see Figure 4.2). The ion compositions differed as well between the two segments, with heavy ions (mass-to-charge ratio  $m/q = 16$  and  $32$ ) dominating during the first segment and light ions (mass-to-charge ratio  $m/q = 1$  and  $2$ ) dominating during the second segment (Coates et al. (2007b), Szego et al. (2007)). Szego et al. (2007) suggested that the second event was part of the distant pick-up tail of Titan and that during the first event ions were escaping along magnetic field lines due to the specific magnetic background geometry. Coates et al. (2007b) identified ionospheric particles in both events and suggested that the source of the ions in the second event was located on the nightside of Titan and at higher altitudes. Sittler et al. (2010)

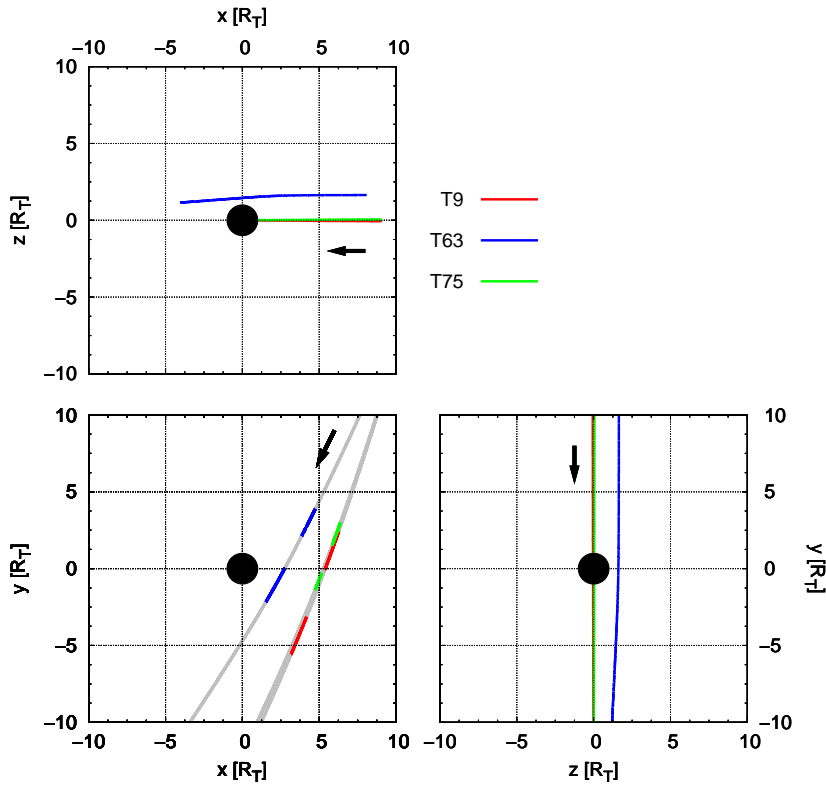


**Figure 4.1:** Projections of the T9, T63 and T75 flyby trajectories onto the planes of the TIIS coordinate system. The colored intervals along the trajectories in the  $xy$  plane indicate the locations of the split signatures according to Coates et al. (2012). T9 and T75 occurred in Titan's equatorial plane, with nearly identical trajectories. T63 took place slightly north of Titan's equatorial plane. The flyby direction was the same for all encounters, indicated by the black arrows.

explained the second event as light ions that were picked up by draped field lines near the induced magnetopause boundary. Similar split signatures have also been reported for the T63 (see figure 4.3) and T75 encounters by Coates et al. (2012). However, for both of these flybys the individual filaments of the split tail contained an admixture of heavy ( $m/q = 16$  and  $28$ ) and light ( $m/q = 1$  and  $2$ ) ions, in contrast to T9. The authors also used Cassini Plasma Spectrometer (CAPS) data to constrain plasma escape rates for each flyby and concluded that Titan's ionosphere loses about 7 tonnes of mass per Earth day. Magnetic field observations from the T9 encounter (Bertucci et al. (2007)) showed that Titan was located below Saturn's magnetodisk, i.e., the magnetic field possessed significant components oriented towards Saturn and along the corotational flow direction (see also Bertucci et al. (2009)). By identifying the position of the neutral region between Titan's magnetic lobes, Bertucci et al. (2007) concluded that the upstream flow was pointing away from Saturn at an angle of  $36^\circ$ . However, other authors suggested a number of different values for the direction of the upstream flow (Modolo et al. (2007a), Szego et al. (2007), Coates et al. (2012)). Sittler et al. (2010) investigated CAPS data from T9 and suggested that the upstream plasma flow consisted mainly of light ( $H^+$ ,  $H_2^+$ ) ions. The

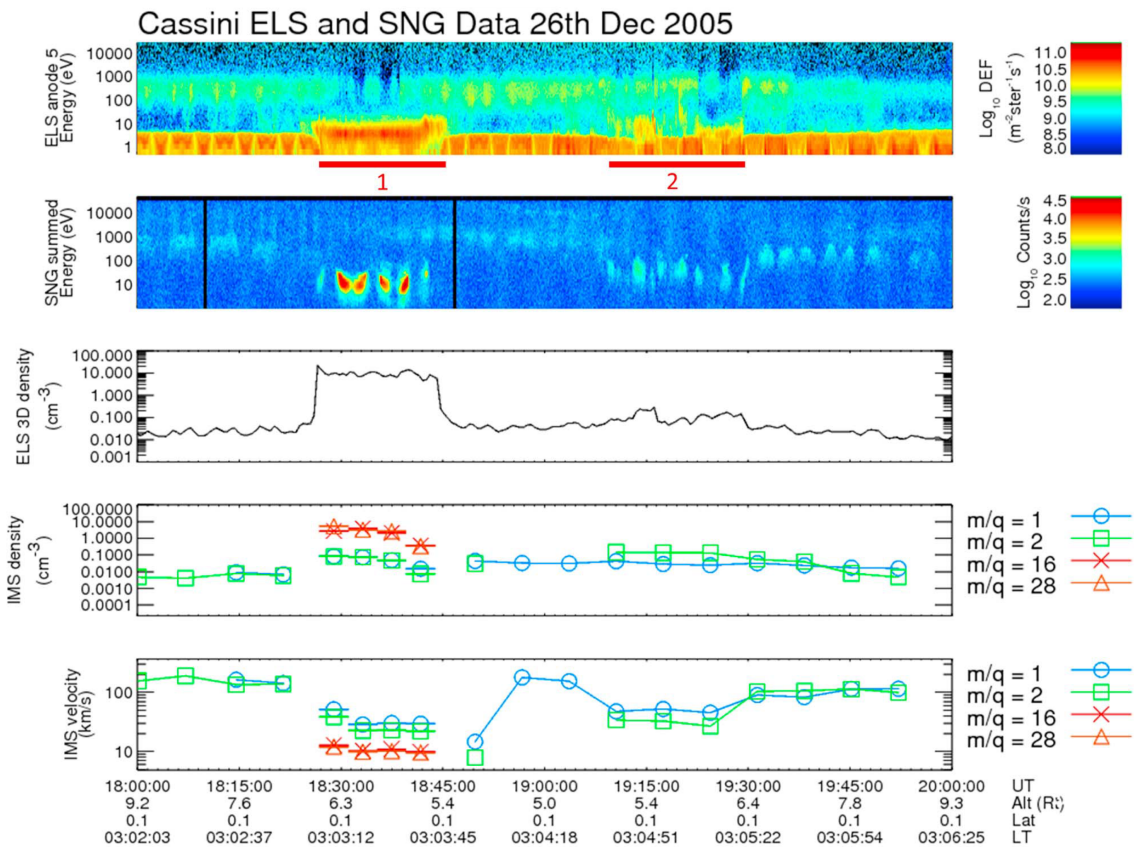


**Figure 4.2:** Combined plot of ion and electron observations during the T9 flyby. The first panel shows the observed electron- and the second panel the ion spectra. The third panel shows the derived electron density. Panel four and five show the derived densities and velocities for ions with masses 1,2,16 and 28 amu. Only the light species ions were detected during the second event. Figure from Coates et al. (2012)

upstream flow during T63 and T75 was approximately corotational (Coates et al. (2012)). By applying a hybrid model (kinetic ions, fluid electrons), Modolo et al. (2007a) were able to reproduce the locations of the split signatures measured by the Langmuir Probe in the electron densities during T9. They needed an upstream plasma with a high mass density ( $O^+$  component with  $n(O^+) = 0.2 \text{ cm}^{-3}$ , as suggested by Neubauer et al. (1984)) in order to do so. Hybrid modeling by Kallio et al. (2007) showed that the magnetic field measurements during T9 can only be explained if the upstream plasma possesses such a high mass density. Hybrid modeling by Simon et al. (2007c) showed that the magnetic field topology measured during the T9 encounter is very robust against changes of the ionospheric SUV production rate and that a rotation of the ambient flow direction away from Saturn by  $34^\circ$  gives good agreement with the observed magnetic data. Ma et al. (2007) showed that applying a Hall-MHD model is suitable to reproduce magnetic perturbations seen during the flyby. These authors also showed that without a heavy upstream plasma component (16 amu) the magnetic data cannot be reproduced. However, their model did not succeed in generating the split signature and showed only a single peak in the electron density that was located in-between the two segments of the split tail. Subsequently, Lipatov et al. (2012) applied a hybrid model with an upstream plasma con-

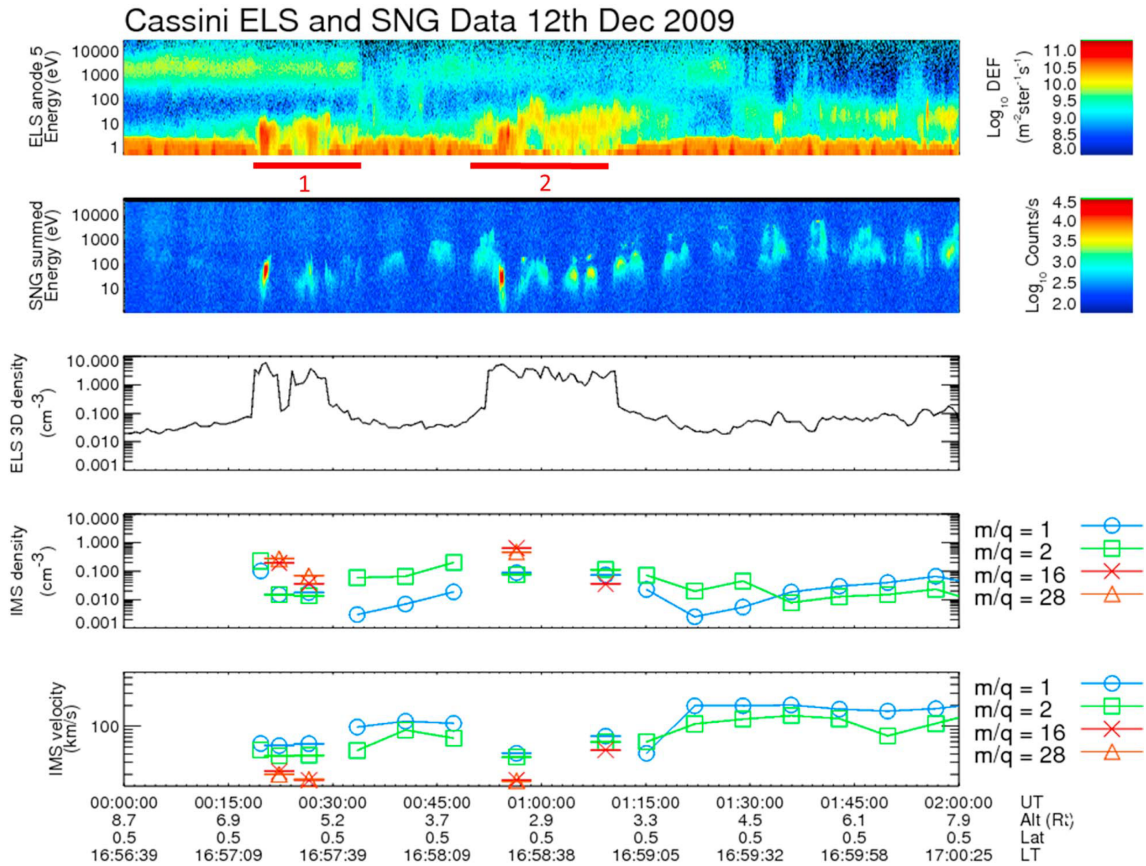


**Figure 4.3:** Combined plot of ion and electron data during the T63 flyby. The third panel shows the derived electron density. Panel four and five show the derived densities and velocities for ions with masses 1,2,16 and 28 amu. Both heavy and light ion species were detected in the split signature. Figure from Coates et al. (2012)

sisting only of  $H^+$  ions and showed that using a high density ( $n(H^+) = 0.1 \text{ cm}^{-3}$ ) plasma or a low density ( $n(H^+) = 0.02 \text{ cm}^{-3}$ ) plasma with high beta produces similar results for the T9 flyby. They were able to quantitatively reproduce the ion densities measured in the first event; however, their modeling produced a higher density during the second event and no density gap in-between the two events. Their model also failed to simultaneously reproduce the magnitudes and locations of the magnetic draping signatures.

However, Lipatov et al. (2012) assumed that the incident magnetospheric ions moved at super-corotational speed ( $\sim 125\%$  the nominal corotation speed at Titan), which is inconsistent with the ambient magnetic field observations during T9. During this flyby the magnetometer detected a field line orientation that was swept back with respect to a strictly corotating meridional plane (i.e.  $B_{0,x} > 0$ ,  $B_{0,y} > 0$  in TIIS coordinates). According to Bertucci et al. (2009) and Simon et al. (2010) (see Figure 4 in that work), this implies that the incident plasma was in a state of subcorotation.

Several authors proposed that the split signatures seen in Titan's tail region during T9 may be related to non-stationarities or in the incident magnetospheric flow conditions on the length and time scales of the encounter (Modolo et al. (2007a), Bertucci et al. (2007)). However, the subsequent detection of these features during T63 and T75 suggests that

the split signatures may indeed be a more common feature in Titan’s plasma interaction region. The non-detection of these split signatures during numerous tail crossings may imply that the individual filaments of the split tail are quite narrow in diameter. This suggests that it might be fairly easy for Cassini to simply ‘miss’ these signatures during an encounter. So far the split signatures detected during the T63 and T75 encounters have not been the subject of any modeling.

In this chapter, we therefore conduct a systematic study of the split signatures in the ion densities downstream of Titan, focusing especially on the dependency of the locations, densities and extensions of the individual tail filaments on Titan’s orbital position and the incident magnetospheric flow conditions. We are more interested in understanding the physics behind these split signatures than in reproducing the details of the observations. For all three flybys during which Cassini detected a split signature in Titan’s tail, the incident magnetospheric flow conditions are poorly constrained. Especially for T9, conflicting information on the incident plasma composition and flow direction can be found in the literature (cf. Kallio et al. (2007), Modolo et al. (2007a), Sittler et al. (2010), Coates et al. (2012)). As opposed to exploring the vast parameter space of upstream conditions to achieve the best possible agreement with the data as other studies have done (Kallio et al. (2007), Simon et al. (2007c), Modolo et al. (2007a), Lipatov et al. (2012)), we rather focus on a few simple scenarios that permit straightforward access to the physical mechanisms leading to the generation of the split tails.

This chapter is structured as follows: in Section 4.2 we describe the different simulation setups that are considered for this part. The results of our model runs are presented in Sections 4.3 to 4.5, along with a discussion of their implications for Cassini observations in Titan’s tail region. Our major findings are briefly summarized in Section 4.6.

## 4.2 Simulation Setup and Numerical Parameters

In our simulations we use a box with an extension of  $20R_T \times 20R_T \times 20R_T$ , where the center of the box coincides with the center of Titan. A hierarchical grid with one level of refinement is used, the spatial resolutions of which are  $L_0 = 0.25R_T$  and  $L_1 = 0.125R_T$ . The region of high refinement is located within a cube of  $2R_T \times 2R_T \times 2R_T$  around the center of Titan, containing the ionosphere. In all simulation runs, we use two magnetospheric upstream species,  $O^+$  and  $H^+$ , with  $n(O^+) = 0.2 \text{ cm}^{-3}$ ,  $n(H^+) = 0.1 \text{ cm}^{-3}$ . The upstream flow direction is always corotational. The upstream species are initialized with 40 particles in every cell at the beginning and at the outer boundaries during the simulations. The inner boundary is set to 1000km above the surface during all runs. If a particle reaches the inner boundary, it is removed from the simulation. The plasma parameters for the simulation runs presented in this chapter are summarized in Table 4.1. To permit straightforward access to the physics of the split signatures in Titan’s tail, we first consider an idealized geometry, where the upstream flow direction is aligned with the  $x$ -axis and the ambient magnetic field is aligned with the  $-z$  axis (Run #1 in table 4.1). In the literature, this setup is often referred to as the ‘Voyager 1 scenario’ of the Titan interaction (Simon et al. (2009a)).

For the T9 case (Run #2 in Table 4.1) there has been a lot of discussion about the direction and composition of the upstream plasma flow. While the consensus was that the

Quantity	Symbol	Run #1	Run #2	Run #3
Local Time	LT	18:00	3:00	17:00
Latitude of Subsolar point	SSL [°]	0	-19.06	-2.04
Upstream magnetic field vector	$\underline{B}_0$	(0,0,-5)	(3.73,4.7,-2.15)	(0.05,-0.33,-4.48)
Upstream magnetic field strength	$B_0$ [nT]	5	6.37	4.49
Number density of upstream O <sup>+</sup>	$n_{0,O^+}$ [cm <sup>-3</sup> ]	0.2	0.2	0.2
Number density of upstream H <sup>+</sup>	$n_{0,H^+}$ [cm <sup>-3</sup> ]	0.1	0.1	0.1
Upstream plasma bulk velocity	$U_0$ [km/s]	120	120	120
Alfvénic Mach number	$M_A$	1.96	1.54	2.22
O <sup>+</sup> gyration period	$\Omega_0^{-1}$ [s]	33	26	37

**Table 4.1:** Plasma parameters of the simulation runs.

flow deviated from the corotational direction, a number of different values for the angle of this deviation have been proposed in numerical and observational studies (Bertucci et al. (2007), Modolo et al. (2007b), Szego et al. (2007)). Also, Kallio et al. (2007), Simon et al. (2007c) and Ma et al. (2007) showed that in order to explain the magnetic signatures which were observed during T9, an upstream plasma with a high mass density ( $\sim 10^{-1}$  amu/cm<sup>3</sup>) is needed, in contrast to observational studies that showed no evidence of heavy ions (O<sup>+</sup>) in CAPS data (Sittler et al. (2010), Coates et al. (2012)). Considering the typical electron number densities observed at Titan's orbital position (on the order of  $10^{-2}$  cm<sup>-3</sup>, cf. Arridge et al. (2011a)), such high mass density cannot be achieved by a plasma only consisting only of H<sup>+</sup> and H<sub>2</sub><sup>+</sup>.

In summary, CAPS and MAG observations do not provide a consistent picture of the magnetospheric flow parameters during T9, and even different studies of CAPS data suggest conflicting values for the vector  $\underline{u}_0$ . Again, we are more interested in investigating the physics of the split signatures rather than in reproducing flyby data, and therefore restrict ourselves to a corotational upstream flow direction with the same upstream composition as in the Voyager scenario, i.e.  $n_{0,O^+} = 0.2\text{cm}^{-3}$  and  $n_{0,H^+} = 0.1\text{cm}^{-3}$  for all simulations (see Table 4.1). This upstream composition was also used by Kallio et al. (2007) and Simon et al. (2007c) to explain magnetometer data from T9. We also note that a statistical study of CAPS data from numerous crossings of Titan's orbit found the *average* radial and north-south components of the upstream flow direction to be negligible, compared to the azimuthal component (Arridge et al. (2011a)) at the location of Titan (see Table 6 in that work).

During T63 and T75, Titan's environment was distorted by the moon's proximity to Saturn's magnetodisk current sheet (Simon et al. (2013), Smith and Rymer (2014)). The magnetic signature of Titan's interaction during T63 and T75 was therefore partially obscured by magnetospheric fluctuations, whereas T9 was clearly located in the southern lobe of Saturn's magnetodisk. The chosen background magnetic field vector for T63 is therefore strongly dependent on the averaging intervals and not well constrained, whereas for T9 the background magnetic field has a far more quiet structure.

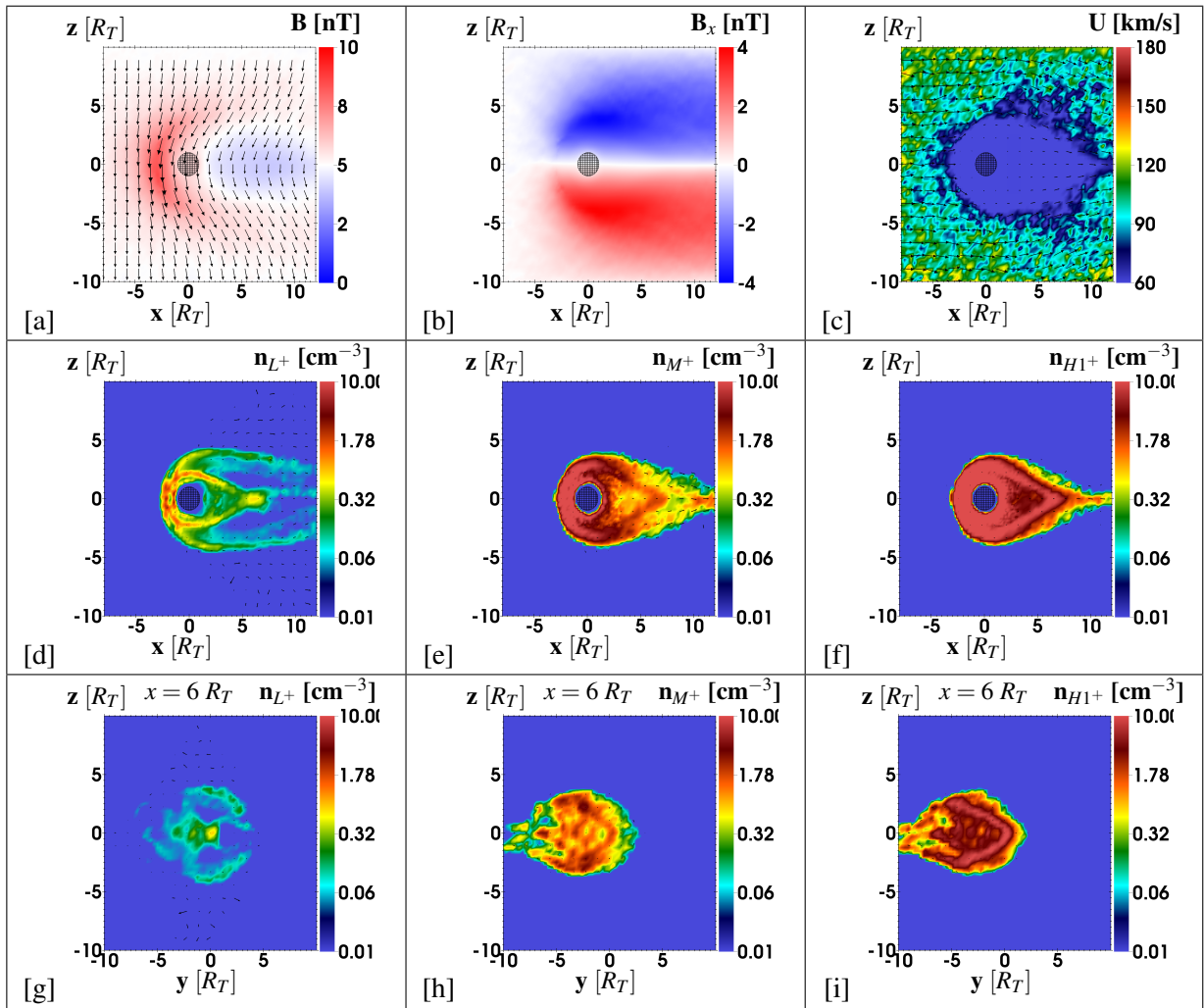


**Figure 4.4:** Plasma quantities in the  $y = 0$  plane for Run #1: (a) Magnetic field strength, (b)  $B_x$  component (c), Total velocity magnitude  $|\underline{u}_i|$  (Eq. 3.6), (d) Ionospheric  $L^+$  density, (e) Ionospheric  $M^+$  density, (f) Ionospheric  $H1^+$  density. Quantities in  $x = 6 R_T$  plane: (g) Ionospheric  $L^+$  density, (h) Ionospheric  $M^+$  density (i), Ionospheric  $H1^+$  density. Arrows indicate velocities of respective ion species ( $\underline{u}_j$ ) or the quantity itself ( $\underline{B}$ ,  $\underline{u}_i$ ).

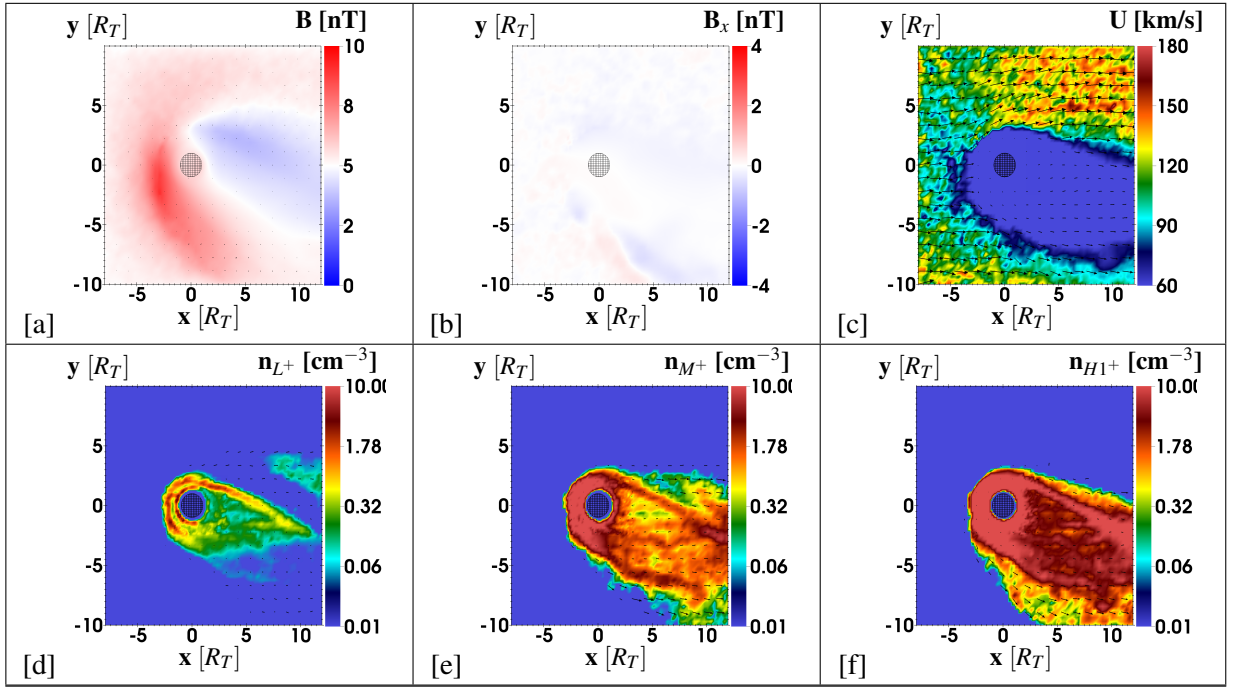


**Figure 4.5:** Plasma quantities in the equatorial  $z = 0$  plane for Run #1. (a) Magnetic field strength, (b)  $B_x$  component, (c) Total velocity magnitude  $|\underline{u}_i|$ , (d) Ionospheric  $L^+$  density, (e) Ionospheric  $M^+$  density, (f) Ionospheric  $H1^+$  density. Arrows indicate velocities of respective ion species ( $\underline{u}_j$ ) or the quantity itself ( $\underline{B}$ ,  $\underline{u}_i$ ).

### 4.3 Run #1: Voyager-type upstream conditions

First we look at the ‘canonical’ Voyager scenario (Run #1 in Table 4.1). In this run, the dayside ionosphere coincides with the ramside of the moon and the convective electric field points in the  $-y$  direction. Important upstream plasma quantities and the densities of the  $L^+$ ,  $M^+$  and  $H1^+$  species are plotted in Figure 4.4.

Panel 4.4(a) shows the magnetic field strength with a pileup upstream of Titan of  $\sim 8$  nT (undisturbed value  $\underline{B}_0 = 5$  nT) and a decreased field in the magnetic wake downstream of Titan with a value  $\sim 3.5$  nT. The draping of the magnetic field is seen in the  $B_x$  component in panel 4.4(b), where the  $B_x$  component is negative in the northern lobe and positive in the southern lobe, reaching values of  $\pm 3.25$  nT (from  $B_{0,x} = 0$ ). The draping is symmetric with respect to  $z = 0$  in this plane. As can be seen from panel 4.4(c), the plasma velocity  $|\underline{u}_i|$  is greatly reduced from its upstream value of  $\underline{u}_0 = 120$  km/s to a few m/s in the vicinity of Titan, starting at  $x \approx -4$ . The region of reduced flow speed possesses an extension of up to  $8 R_T$  along the  $z$  axis, due to collisions and mass-loading of cold ionospheric ions. Compared to our previous simulations (e.g., Simon et al. (2006b)), the effective size of the obstacle is increased by about  $\sim 2-3 R_T$  due to the large region around Titan where slow ionospheric ions reduce the mean plasma velocity, leading to a broader and more diffuse pileup and draping pattern of the magnetic field. Panels 4.4(d)-(f) show the structure of the ionospheric tail in the plane parallel to the background field  $\underline{B}_0$ , revealing a different behavior between the light species ( $L^+$ ) and the heavy species ( $M^+$ ,  $H1^+$ ). The light ion species in panel 4.4(d) shows a symmetric split tail in the  $y = 0$  plane with four escape

paths near Titan ( $x < 6 R_T$ ) and only three further away downstream ( $x > 6 R_T$ ). The split tail consists of two outer filaments visible at  $z = \pm 5 R_T$  and two inner filaments at  $z = \pm 2 R_T$ , which merge into a single tail along  $z = 0$  with densities comparable to or larger than the upstream plasma density. The two outer filaments have a thickness of less than  $1 R_T$  in  $z$  direction and become more diffuse with increasing distance to Titan. The heavy species in panels 4.4(e),(f) show two broader filaments (thickness  $1-2 R_T$ ) which merge at a similar distance in the  $z = 0$  plane. These structures correspond to the *inner* filaments seen in the  $L^+$  species, but no outer filaments are formed.

The formation of the outer filaments in the light species can be understood as follows: Due to the electron pressure gradient force pointing away from Titan, newly generated ions are accelerated radially *away* from the moon. A fraction of these ions then move along the draped magnetic field lines and escape into the region of Titan's magnetic lobes as they are transported downstream, which produces the two outer filaments at  $z = \pm 5 R_T$  in the density pattern of the light ion species ( $L^+$ ). The heavier ionospheric species (panels 4.4(e),(f)) are in principle susceptible to the same escape mechanism. However, since the light neutral species has a larger scale height than the heavy species ( $H_{H_2} \sim 300$  km compared to  $H_{N_2,CH_4} \sim 70 - 90$  km), the region where light  $L^+$  ions are produced penetrates deeper into the region of draped field lines than the region where  $M^+$  and  $H1^+$  ions are produced. Therefore the fraction of light ions escaping along the draped field lines is much larger than the fraction of intermediate ( $M^+$ ) and heavy ions ( $H1^+$ ). For this reason the two outer filaments are absent in the density patterns of the heavier species (panels 4.4(e),(f)).

The ions generated at lower altitudes form the two inner filaments, which are seen in all ionospheric species. Since the ion production rates of the heavy species are at least one order of magnitude higher than that of the light ions, the inner filaments of the heavy species (panels 4.4(e),(f)) have a higher density (factor  $\sim 10$ ) and are broader ( $1 - 2 R_T$  compared to less than  $1 R_T$ ). The inner filaments are mainly associated with the transport of ions from the ramside towards downstream, i.e. these filaments first 'drape' around Titan and are then focused into the magnetic wake, merging to a single tail at a certain distance (at  $x \sim 6 - 7 R_T$  in this simulation) along the  $x$ -axis in the  $z = 0$  plane. This yields a triangular escape pattern in the  $y = 0$  plane with a region of decreased density inside (factor of  $\sim 10$  compared to the filaments). In Run # 1 the dayside ionosphere coincides with the ramside (18 Saturnian Local Time), so that most of the ions are produced at the ramside and have to pass Titan to reach the wake.

For the  $x = 6 R_T$  plane, panels 4.4(g)-(i) depict the densities of the ionospheric species to illustrate the extent and structure of the outer filaments perpendicular to the magnetic field. In this plane, the outer filaments of the light  $L^+$  species in panel 4.4(g) have a parabolic shape that cover the region of a half-circle ( $-2 R_T < y < 4 R_T$  and  $-4 R_T < z < 4 R_T$ ), and are discontinuous perpendicular to the magnetic field (along  $z = 0 R_T$ , cf. panel 4.4(g)). They have a thickness of less than  $1 R_T$ , which is the same extension as already seen in the  $y = 0$  plane of panel 4.4(d). The outer filaments are mostly seen on the Saturn-facing side ( $y > 0 R_T$ ). On the Saturn-averted side ( $y < -2 R_T$ ) no parabolic filament structure can be identified, since the pick-up motion of the ions is going into that direction, as can be seen by the asymmetry in the ion density distribution towards  $y < 0$  in panels 4.4(g)-(i). Since the outer filaments of the light  $L^+$  species have a small thickness and are mainly located in planes that are defined by the unperturbed convective electric field  $\underline{E}_0 = \underline{u}_0 \times \underline{B}_0$ , it

would be easy for a spacecraft to miss them. For the Voyager-type upstream conditions just discussed, a spacecraft would have needed to move mainly in the  $z$  direction to be able to detect the outer filaments of the light species. Spacecraft trajectories that are not roughly aligned with the magnetic background field  $\underline{B}_0$  cannot observe both of the split tail filaments, only one part of them.

The quantities for the equatorial  $z = 0$  plane are shown in Figure 4.5. The magnetic field pile up shown in panel 4.5(a) is shifted towards  $y < 0$  (see also Simon et al. (2006b)). No draping pattern can be seen in the  $B_x$  component in panel 4.5(b), since the  $z = 0$  plane coincides with the neutral plane of the draped field. The area of decreased plasma velocity in panel 4.5(c) is also shifted towards  $y < 0$ , due to the cycloidal motion of pickup ions into that direction. The pickup tail of the  $L^+$ ,  $M^+$  and  $H1^+$  species is seen in panels 4.5(e)-(f). Newly generated ions escape on cycloidal trajectories in the direction of the convective electric field, forming an asymmetric structure in the equatorial plane due to the large gyro radii which are on the order of several Titan radii. In this plane the tail also exhibits filament-like structures: Similar to the  $y = 0$  plane, the transport of ions from Titan's ramside to the wakeside generates a similar triangular region of decreased density downstream of the moon as seen in panels 4.4(d)-(f). However, this structure is asymmetric with respect to the direction of the convective electric field, i.e. it is frayed out.

Thus, the ionospheric tail of Titan possesses a quite complex structure. The densities in Titan's pick-up tail are not homogeneous, but the ion escape mainly takes place in several narrow, filament-like channels. In the  $y = 0$  plane (i.e. the plane defined by  $\underline{E}_0$ ), the tail is symmetric with respect to  $z = 0$  and consists of four segments near Titan. Along the outer edges, only light (2 amu) ions escape into the magnetic lobes. These outer filaments exhibit a parabolic shape in directions perpendicular to  $\underline{u}_0$ . However, the largest fraction of all species escape in two inner filaments from the dayside to the nightside and is focused into the magnetic wake at  $z = 0$ .

Filamentation of the ionospheric tail is also seen in the  $z = 0$  plane (defined by  $\underline{n} = \underline{B}_0$ ), however here the tail structures are asymmetric (shifted towards  $y < 0$ ) due to the large gyro radii of the pick-up ions. Combined, the inner filaments which are associated with the transport of ions from the ramside to the wakeside form a cone structure behind Titan, pointing towards downstream. The surface of the cone consists of the inner filaments and inside the cone the density of the ionospheric species is decreased compared to the surface. The apex of the cone is the point downstream of Titan, where the inner filaments merge to a single tail. Towards the direction of the convective electric field, the cone is 'open', or frayed out. It is therefore possible to find trajectories that penetrate through different parts of the filament structures, leading to the detection of split signatures in the ion densities.

### 4.3.1 Run #1: Collisions and $\nabla P_e$ removed

Now we consider the same upstream conditions as in Run #1, but this time with collisions and  $\nabla P_e$  term removed from the simulation. Apart from the more sophisticated ionosphere model, this setup is similar to what was done in our preceding studies (Simon et al. (2006b, 2007b)). We plot the same selection of quantities as in the previous section, for the  $y = 0$  plane in Figure 4.6 and the equatorial  $z = 0$  plane in Figure 4.7.

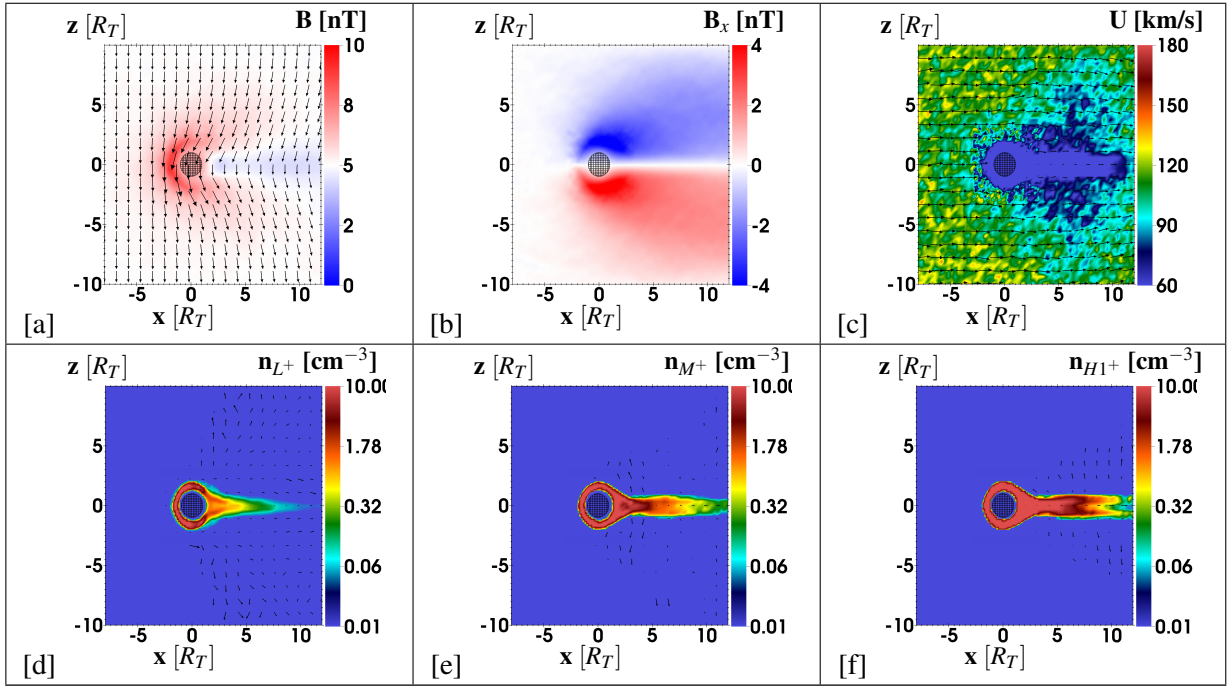


**Figure 4.6:** Plasma quantities in the  $y = 0$  plane for Run #1 with collisions and  $\nabla P_e$  term removed. (a) Magnetic field strength, (b)  $B_x$  component, (c) Total velocity magnitude, (d) Ionospheric  $L^+$  density, (e) Ionospheric  $M^+$  density, (f) Ionospheric  $H1^+$  density. Arrows indicate velocities of respective ion species ( $\underline{u}_j$ ) or the quantity itself ( $\underline{B}$ ,  $\underline{u}_i$ ).

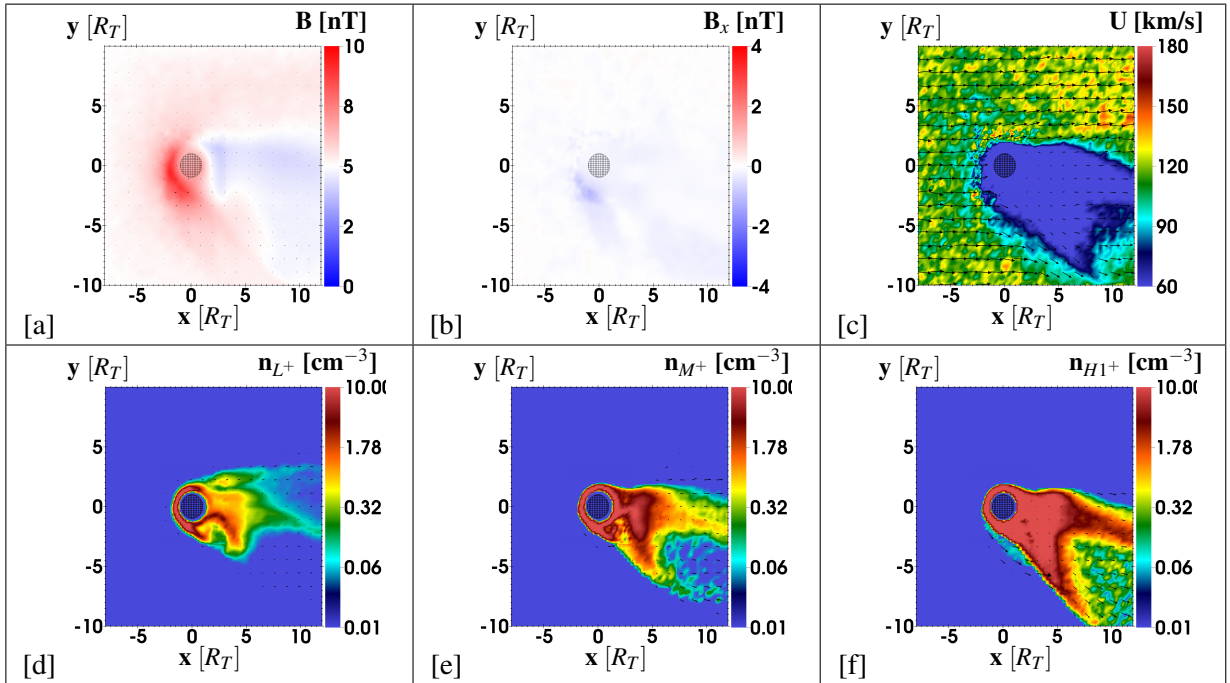


**Figure 4.7:** Plasma quantities in the  $z = 0$  plane for Run #1 with collisions and  $\nabla P_e$  term removed. (a) Magnetic field strength, (b)  $B_x$  component, (c) Total velocity magnitude, (d) Ionospheric  $L^+$  density, (e) Ionospheric  $M^+$  density, (f) Ionospheric  $H1^+$  density. Arrows indicate velocities of respective ion species ( $\underline{u}_j$ ) or the quantity itself ( $\underline{B}$ ,  $\underline{u}_i$ ).

With no collisions and no  $\nabla P_e$  term in the electric field equation, the overall plasma interaction is confined to a narrower region than before, since the ionosphere is no longer inflated by the pressure gradient term and thus, the effective size of the obstacle is much smaller. This is indicated by the region of reduced plasma velocity around Titan in panel 4.6(c), which is by a factor of  $\sim 2$  smaller than in the previous run (panel 4.4(c)). With no collisions and the  $\nabla P_e$  term removed, the magnetospheric ions are not slowed down in Titan's neutral atmosphere, and the cold ionospheric ions are not accelerated radially away from Titan, so that the region of decreased plasma velocity around Titan is not inflated. Bagdonat (2005) found a similar impact of the pressure gradient term in hybrid simulations of the solar wind interaction of comet 67P/Churyumov-Gerasimenko. This author showed that the pressure gradient term tends to extend the region of high heavy ion density around the comet, thereby also increasing the size of the region where the Solar Wind is deflected and decelerated.

Consequently, the pileup of the magnetic field in panel 4.6(a) is slightly increased with  $\approx 9$  nT compared to before ( $\approx 8$  nT) due to the more pronounced draping of the magnetic field around Titan. The outer filaments of the light species vanish (panel 4.6(d)) since no ions are accelerated radially away from the moon, i.e. the region at Titan's ramside where the region of slow ionospheric particles intersects the draped magnetic field is much smaller than in the preceding case. The cone structure formed by the inner filaments is not visible anymore (panels 4.6(d)-(f)), as the ions generated on the ramside pass Titan at a much closer distance and the two streams merge immediately downstream of Titan into a single narrow tail. The tail formed by the heaviest species shows some tendency to split up at large distances to Titan: the only split tail structure that can be identified here is confined to the equatorial plane, where one filament is filling the magnetic wake (at  $y = 0$  in panels 4.6(d)-(f), and another filament (panels 4.6(e),(f)) is seen on the  $y < 0$  side, associated with the cycloidal motion of the pick-up ions. However, there is no Cassini flyby that could confirm the existence of this feature.

## 4.4 Run #2: T9-type upstream conditions

During T9 the background magnetic field possessed large positive  $B_{0,x}$  and  $B_{0,y}$  components (Table 4.1) due to Titan's location below Saturn's magnetodisk (Bertucci et al. (2007)). The field lines were swept back due to the corotation lag (Simon et al. (2010)) and were bent towards Saturn. Since the corotational upstream flow is no longer perpendicular to the magnetic background field, the neutral sheet between Titan's magnetic lobes becomes curved, i.e. the magnitudes and extensions in the moon's northern and southern magnetic lobes are no longer symmetric. In addition, the asymmetry that arises from the large gyro radii (Simon and Motschmann (2009)) is still present. An overview of the upstream geometry and the orientation of important planes in TIIS coordinates is provided in Figure 4.8. Since the upstream magnetic field is not aligned with the  $z$ -axis anymore, the tail as a whole is rotated, i.e. the quasi-cycloidal structures of the pick-up ions are not confined to the equatorial  $z = 0$  plane as in the Voyager case (Run # 1), but instead to the inclined plane which is defined by the normal vector  $\underline{B}_0$  (cf. Figure 4.8(b)).

In Figures 4.9(a)-(f) we show the plasma quantities in the plane perpendicular to the mag-

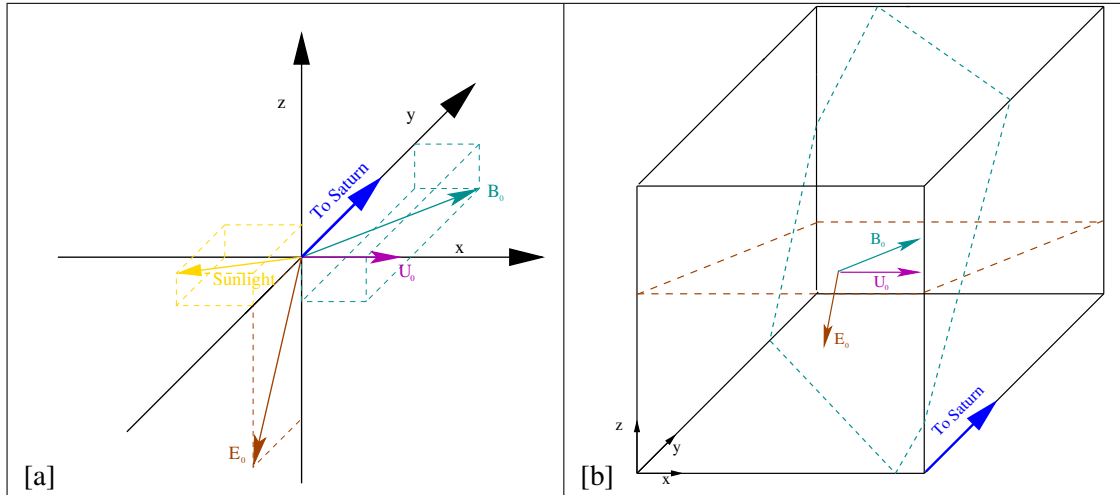


**Figure 4.8:** (a) Upstream geometry of  $\underline{u}_0$ ,  $\underline{B}_0$  and  $\underline{E}_0$  during the T9 encounter in the THIS coordinate system. (b) Orientation of the inclined planes defined by  $\underline{B}_0$  (cyan plane) and  $\underline{E}_0 = -\underline{u}_0 \times \underline{B}_0$  (brown plane) in the simulation box.

netic field, i.e., the plane defined by the normal vector  $\underline{n} = \underline{B}_0$  (cyan plane in Figure 4.8(b)). This inclined plane includes an angle of about  $42^\circ$  with the  $y = 0$  plane, which is why the sections in panels 4.9(a)-(f) have a non-quadratic shape. Also note that the drift velocity  $\underline{E}_0 \times \underline{B}_0$  is not parallel with  $\underline{u}_0$  (corotation) in this run, instead it also possesses components that are aligned with  $-z$  and  $-y$ . Panel 4.9(a) shows the asymmetric pileup and wake structure, which is similar to Figure 4.5(a). The  $B_x$  component of the magnetic field in panel 4.9(b), however, does not indicate the neutral plane of the draped magnetic field anymore as in Figure 4.5(b), because of the rotated magnetic background. As expected, the asymmetric tail structures of the ionospheric species are seen in the plane perpendicular to the magnetic field (cf. panels 4.9(d)-(f)). Filaments ( $1-2 R_T$  thickness) are visible at  $z \approx \pm 3 R_T$ , as well as smaller filaments (thickness less than one  $R_T$ ) for the  $M^+$  and  $H1^+$  species on the edge of the pickup structures (towards  $z < 0$ ). However, no real cone structure is seen, as the filaments do not merge into a single tail similar to the plots in panels 4.5(d)-(f).

A cut through Titan's ionospheric tail at  $x = 6 R_T$  is plotted in panels 4.9(g)-(i). Compared to the plots from Figure 4.5(g)-(i) the filament structure is similar, but they are rotated clockwise by  $\sim 70^\circ$ , which is roughly the angle between the T9 magnetic field and north-south magnetic field used in the Voyager scenario. The light  $L^+$  species shows the outer filament structures at  $y = \pm 5 R_T$  in panel 4.9(g), which are again asymmetric with respect to the direction of the pickup cycloids.

Figures 4.10(a)-(f) show the plasma quantities in the equatorial  $z = 0$  plane, which is identical to the plane of the T9 trajectory (cf. Figure 4.1). The draping pattern in panels 4.10(a) and (b) is asymmetric since the upstream magnetic field and flow direction are not perpendicular to each other (Simon and Motschmann (2009)). Panels 4.10(g)-(i) depict the densities of the ionospheric species in the plane defined by the convective electric field  $\underline{E}_0 = \underline{u}_0 \times \underline{B}_0$  (cf. brown plane in Figure 4.8(b)), i.e., in the plane where the split structures are most pronounced corresponding to the  $y = 0$  plane in the Voyager Run # 1. For the selected set of upstream parameters, this plane is roughly coincident with the  $z = 0$  plane,

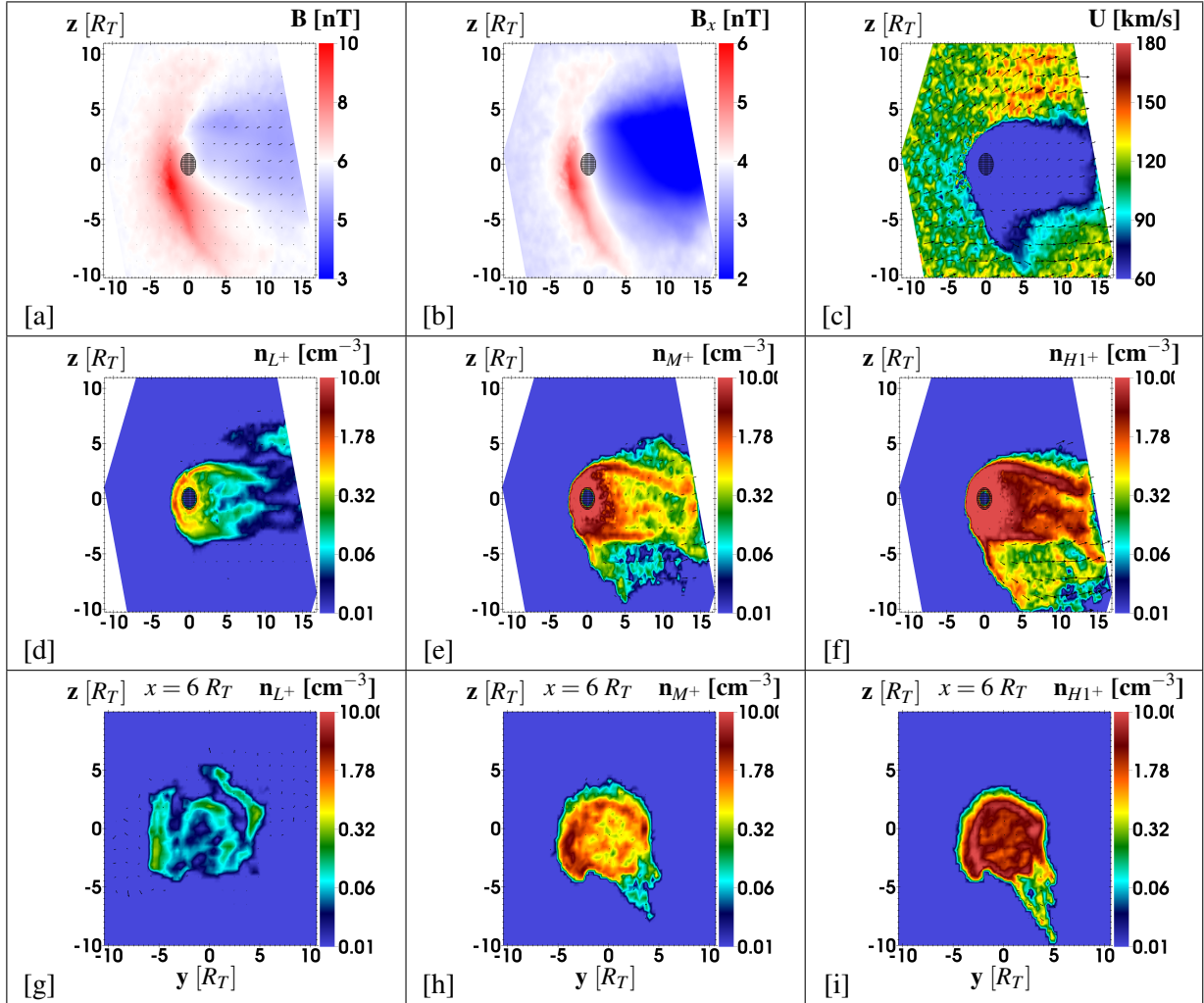


**Figure 4.9:** Plasma quantities for Run #2 (T9) in the plane perpendicular to  $\underline{B}_0$  (cyan plane in Figure 4.8(b), axes are scaled in units of  $R_T$ ): (a) Magnetic field strength, (b)  $B_x$  component, (c) Total velocity magnitude, (d) Ionospheric  $L^+$  density, (e) Ionospheric  $M^+$  density, (f) Ionospheric  $H1^+$  density. Cut through the  $x = 6 R_T$  plane: (g) Ionospheric  $L^+$  density, (h) Ionospheric  $M^+$  density, (i) Ionospheric  $H1^+$  density. Arrows indicate velocities of respective ion species ( $\underline{u}_j$ ) or the quantity itself ( $\underline{B}$ ,  $\underline{u}_i$ ).

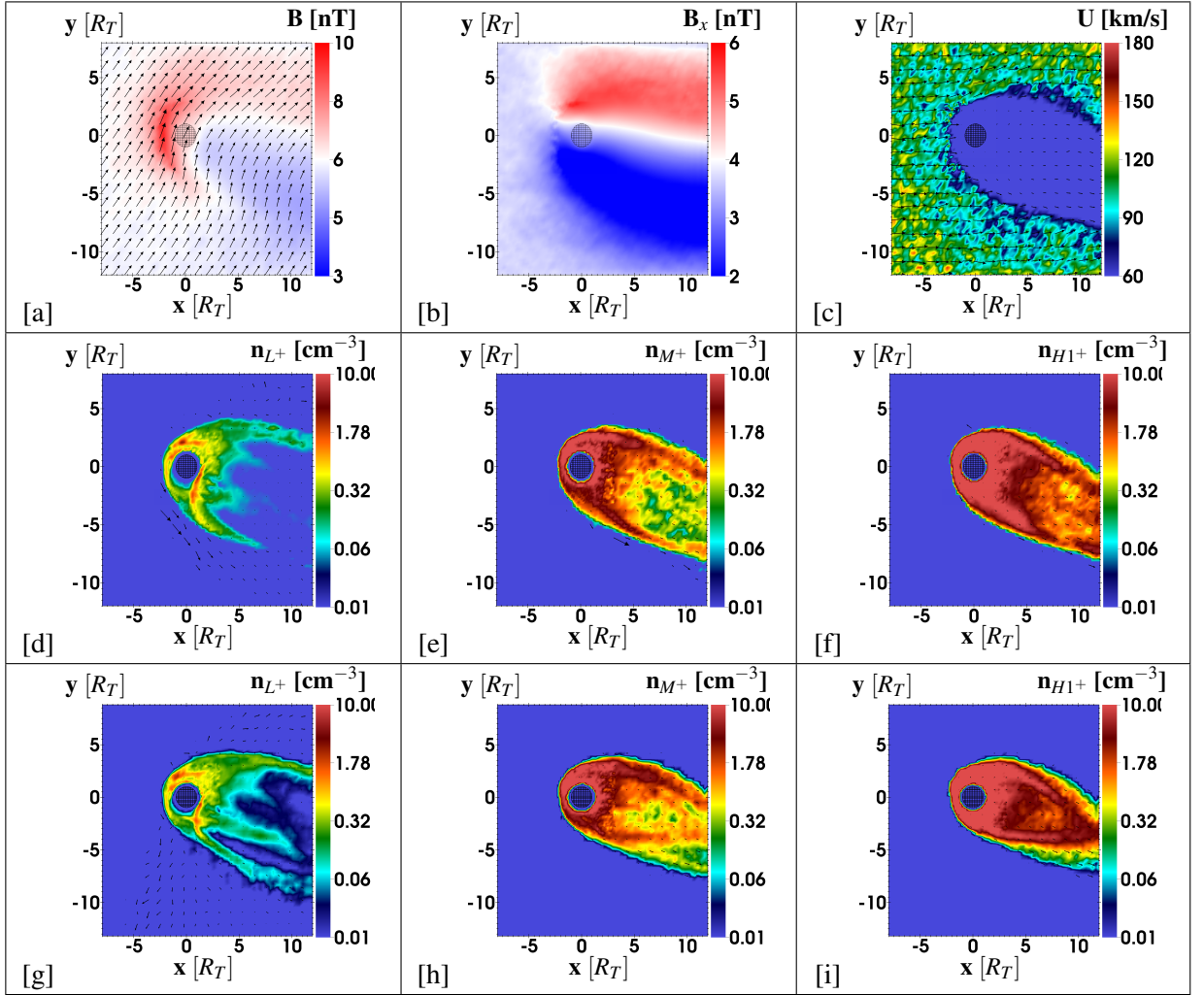


**Figure 4.10:** Plasma quantities for Run #2 (T9) in the *equatorial*  $z = 0$  plane: (a) Magnetic field strength, (b)  $B_x$  component, (c) Total velocity magnitude, (d) Ionospheric  $L^+$  density, (e) Ionospheric  $M^+$  density, (f) Ionospheric  $H1^+$  density. *Inclined plane* defined by  $\underline{E}_0 = \underline{u}_0 \times \underline{B}_0$  (brown plane in Figure 4.8(b)): (g) Ionospheric  $L^+$  density, (h) Ionospheric  $M^+$  density, (i) Ionospheric  $H1^+$  density. Arrows indicate velocities of respective ion species ( $\underline{u}_j$ ) or the quantity itself ( $\underline{B}$ ,  $\underline{u}_i$ ).

but is slightly rotated counter-clockwise around the  $x$ -axis by an angle of  $\sim 25^\circ$ . As we can see in panels 4.10(d)-(i), the tail is tilted with respect to the upstream flow direction  $\underline{u}_0$ .

The split tail of the light  $L^+$  species can be seen in both of these planes (cf. panels 4.10(d) and (g)). However, we do not see a clear four-filament structure as in Run # 1; only three filaments can be identified in these plots. The region of decreased density between the two outer filaments of the light  $L^+$  species in panels 4.10(d) and (g) has a diameter of up to  $7 R_T$ , which is equivalent to 50 minutes of travel time for typical Cassini velocities near Titan (6 km/s). As we would expect, the split tail is most pronounced in the plane that includes both  $\underline{B}_0$  and  $\underline{u}_0$  (cf. panel 4.10(g)), where it reaches the downstream boundary of the simulation box. In the equatorial  $z = 0$  plane (panel 4.10(d)), however, only the Saturn-facing filament reaches the wakeside boundary of the simulation box, whereas the Saturn averted filament bends out of this plane much closer to Titan. This information can be used to obtain an estimation of the length of these parabolic filaments in the plane that contains  $\underline{E}_0$  and  $\underline{B}_0$ . If we consider a point (e.g.  $(5, -7, 0)R_T$ ) where the Saturn-averted filament breaks off in panel 4.10(d) and the angle between the two planes ( $25^\circ$ ), by using simple geometry we derive an upper limit of  $\sim 3 R_T$  on the half width of these filaments in this plane, which is a good approximation if we compare it against the cut through the tail in panel 4.10(g).

On the Saturn-facing side ( $y > 0$ ) the filaments are slightly thicker and more dense, compared to the Saturn-averted ( $y < 0$ ) side. Since the upstream flow is corotational (from  $-x$  to  $+x$ ) and the draped magnetic field lines are more aligned with the upstream flow in the  $y > 0$  half space (see panel 4.10(a)), it is 'easier' for the ions to move into the Saturn-facing segment of the tail. The local time of the encounter further enhances this effect, since Titan's dayside ionosphere during T9 is located in the middle of the  $+x + y$ -quadrant (the orbital position of Titan was at 3 LT, so the terminator line is at a  $45^\circ$  angle with the  $x$ - and  $y$ -axis in TIIS coordinates, cf. panel 4.8(a)). This means more ions are produced on the Saturn-facing side (dayside) than on the Saturn-averted side (nightside) of Titan. Based on the picture from Figure 4.4(d), it seems that the upper outer and inner filaments of the light species merged (from the symmetric case) into one larger filament due to the asymmetric upstream geometry in combination with the location of the dayside ionosphere during T9.

Let us now look at the ion densities of the  $L^+$  and  $M^+$  species along several hypothetical trajectories as well as along the T9 trajectory, plotted in Figure 4.11, to understand the densities in the tail from a spacecraft point of view. Density profiles of the heavy species  $H1^+$  are not shown, as they are very similar to the densities of the  $M^+$  species. The hypothetical trajectories are all parallel to the  $y$ -axis and have different fixed  $x$  and  $z$  coordinates, therefore representing potential observations in different regions of the tail. The exact same trajectories are chosen for both species. It should be noted that selecting a trajectory through a different part of the tail can be equivalent to a change in the upstream geometry, i.e., it does not matter if we change the orientation of Titan's tail or the trajectory.

For a corotational flow, we do not see a clear split signature in the ion densities along the T9 trajectory (Figure 4.11(c), which also shows the T9 CAPS ion data); instead, a broad profile with two small spikes for the heavy species and four spikes for the light species is observed. However there are no significant gaps in-between those spikes, except in the

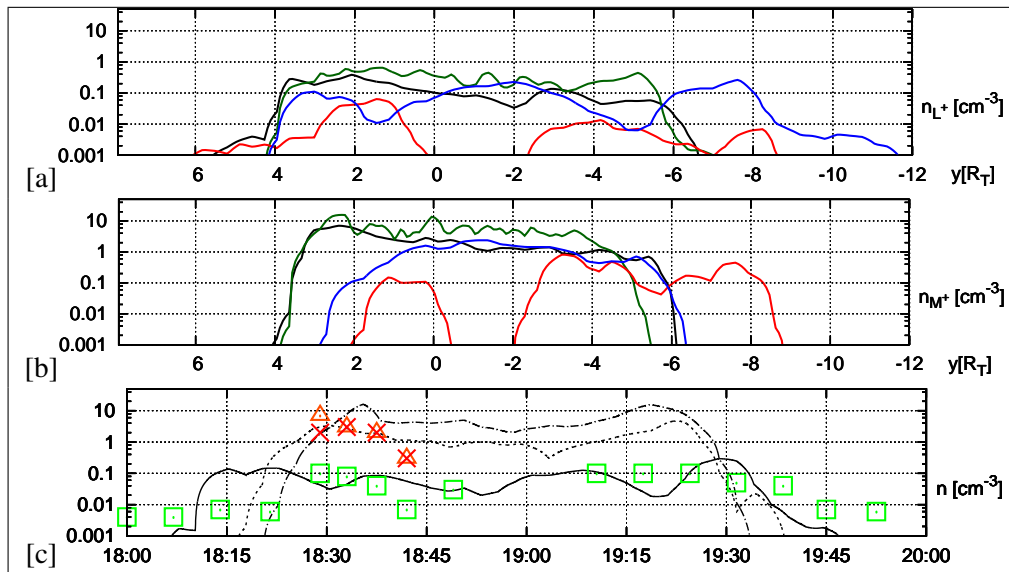


**Figure 4.11:** Densities of the (a)  $L^+$  and (b)  $M^+$  species in the T9 run for different trajectories which are parallel to the  $y$ -axis. Black:  $x = 4 R_T$ ,  $z = -2 R_T$ ; Green:  $x = 2 R_T$ ,  $z = 0$ ; Red:  $x = 8 R_T$ ,  $z = -4 R_T$ ; Blue:  $x = 6 R_T$ ,  $z = 2 R_T$ . (c) Densities of the  $L^+$  (solid),  $M^+$  (dashed),  $H1^+$  (dot-dashed) species along the T9 trajectory. Also shown are the measured CAPS ion densities: Green  $m/q=2$ , Red:  $m/q=16$ , Orange:  $m/q=28$  (cf. Coates et al. (2012)).

profile for the light species at 19:20. As can be seen in Figure 4.11(a) and (b), it is easily possible to find spacecraft trajectories that show split features of varying sharpness, as well as trajectories that show only a single tail crossing. Looking at the densities plotted in red (trajectory located far downstream and south of the equatorial plane) both species show a double-peak, while in between the two peaks the densities fall below  $0.001 \text{ cm}^{-3}$  (less than 1% of the background density in our simulation). Compared to the CAPS measurements as indicated in Figure 4.11(c), this trajectory would therefore have the density gap between the two spikes at roughly the observed location. For the densities plotted in blue (trajectory located north of the equatorial plane and closer to Titan) the light species  $L^+$  shows a triple peak structure and no longer drops to zero, which corresponds to the filaments seen in Figures 4.10 (d) and (g), while the heavy species shows no split feature. The black and green lines correspond to trajectories that are located even closer to Titan and slightly north of (black line) or in the moon's equatorial plane (green line). Neither the light nor the heavy species show a split tail along these trajectories.

As is shown in Figure 4.11, depending on the location of the spacecraft in Titan's tail, there are indeed trajectories which show the split tail feature in the densities of one or more species, although for the T9 trajectory itself we do not see a clear split signature. The upstream flow parameters and the location of the dayside ionosphere with respect to the incident flow direction influences the position and densities of the filament structures. Asymmetries or fluctuations in the upstream flow parameters can therefore further enhance or displace the filaments. Based on our simulation results, the T9 observations can be qualitatively explained by Cassini first penetrating the Saturn-facing (dense) filament, which we see in all ionospheric species, and subsequently passing through the outer

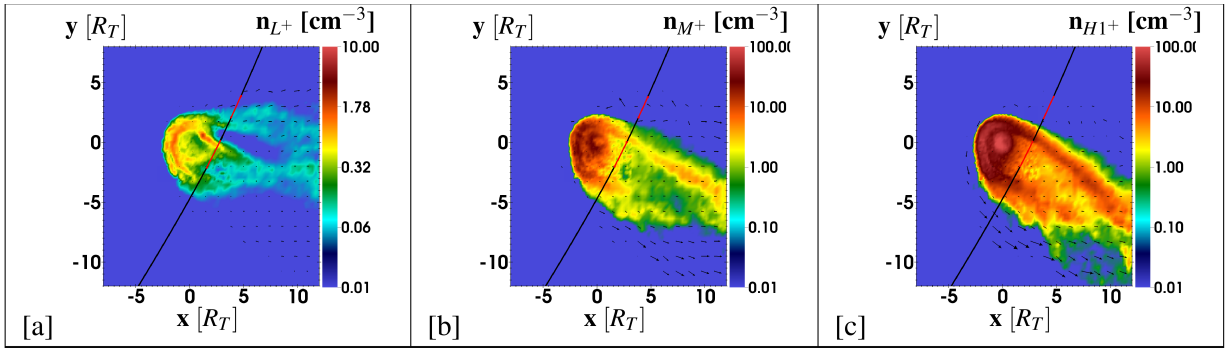


**Figure 4.12:** Densities of the (a)  $L^+$ , (b)  $M^+$  and (c)  $H1^+$  species in the  $z = 1.5 R_T$  plane for T63. Arrows indicate velocities of the respective ion species. The black line shows the T63-trajectory, with the intervals of the observed split signatures marked in red. Cassini moved from  $y > 0$  towards  $y < 0$  during T63.

Saturn-averted filament of the light species. This would explain the observed composition (first interval both heavy and light ions, second interval only light ions, cf. Figure 2 of Coates et al. (2012)) in the split signatures during the T9 encounter. It also explains why the measured densities were higher during the first event (on the Saturn-facing side), compared to the second event. This is because of the much higher ion production rate for the heavy species compared to the light species and the fact that the dayside ionosphere was located mainly on the Saturn-facing side as well.

## 4.5 Run #3: T63-type upstream conditions

During the T63 encounter, the background magnetic field was highly variable, possessing a north-south component with superimposed perturbations in the  $B_y$  component due to strong north-south oscillations of Saturn's magnetodisk current sheet (see Figure 2 of Simon et al. (2014)). The average magnetic background vector we find from this data set mainly pointed in the north-south direction ( $\underline{B}_0 = (0.05, -0.33, -4.48)$ ), because the  $B_y$  oscillations cancel out during the time-averaging process (averaging interval of 2 hours, each before and after Cassini entered the Titan interaction region). The upstream flow  $\underline{u}_0$  pointed in the corotational direction during this flyby (Coates et al. (2012)). Since we chose the same upstream flow composition as in Run #1 (Voyager scenario, Table 4.1), the resulting upstream geometry is nearly identical compared to the previously discussed Voyager scenario (Section 4.3). The local time of the T63 encounter was at 17:00, so that the dayside ionosphere is approximately on the ramside of the moon (similar to Run #1, where the local time was 18:00). The results for the T63 encounter are therefore very similar as those for the Voyager scenario. However this is only because of the rough north-south approximation for the magnetic field, that does not take into account the high level of ambient magnetospheric variability.

Compared to T9, the trajectory of Cassini during T63 (see Figure 4.1) was much closer (C/A at altitude  $1.9 R_T$ ) to Titan. Instead of taking place in the equatorial  $z = 0$  plane, the trajectory was displaced by  $\sim 1.5 R_T$  in the positive  $z$  direction. Looking at the plots from the Voyager case, cf. Figures 4.4(d)-(f) and 4.5(d)-(f), we expect to intersect parts of the

cone structure that are related to the transport of ions from the ramside to the wakeside. The geometry of T63 is also suitable to probe asymmetries between the Saturn-facing and the Saturn-averted hemispheres due to the large gyro radii, since the flyby is located in a plane perpendicular to the magnetic field in our simulation.

These structures are indeed seen in Figure 4.12, where the ionospheric densities from our T63 simulation in the  $z = 1.5 R_T$  plane are plotted. The spacecraft trajectory is shown as well, with indications of the intervals where the split signatures have been measured according to Coates et al. (2012) (also see Figure 4.1 in this work). As we can see, located in the path of the spacecraft are at least two filaments (three for the  $L^+$  species) for all three species with a diameter of  $1.5\text{-}2 R_T$  and densities of  $\sim 10 \text{ cm}^{-3}$ . Note that the observations during T63 showed heavy (16 and 28 amu) and light (1-2 amu) ions in both events of the split signature, with densities  $< 10 \text{ cm}^{-3}$  (Coates et al. (2012)), which is consistent with our results here. However, in our simulation the positions of the filaments do not coincide with the locations of the observations. This is likely because the stationary magnetic background field cannot represent the real magnetic fluctuations that were observed during T63.

The filaments on the Saturn-facing side of the tail in panels 4.12(a)-(c) are due to the transport of ions from the dense ionosphere on the ramside to the wakeside, the same as on the Saturn-averted side where the filaments are broadened due to the gyration of the ions in the  $y < 0$  half space. In between the filaments formed by  $M^+$  and  $H1^+$  (see panels 4.12(b),(c)) the density is decreased, i.e., we see a cut through the cone structure explained in Section 4.3, which is asymmetric in this plane (cf. panel 4.5(d)-(f)). The filament that can be seen at  $y = 1 - 2 R_T$  in panel 4.12 (a) belongs to the outer filament structure of the light  $L^+$  species, which is also present in this slightly elevated plane ( $z = 1.5 R_T$ , cf. panel 4.4(g)).

In summary, the split tail detection during the T63 encounter is well explained with the theoretical picture of the tail structure established earlier, despite the large fluctuations of the ambient magnetospheric field. At T63, Cassini crossed through the cone behind Titan, which arises from the transport of ions from the ramside towards the wakeside. The outer filaments of the light species were probably not intersected during T63. However, we again note that our model does not consider the oscillatory motion of Saturn's magnetodisk during T63, which may very well have affected the locations of the individual tail filaments.

Figures 4.12(a)-(c) suggest that, under *stationary* upstream conditions, the positions of the modeled filaments could be brought into agreement with the observations by a rotation of the entire tail structure around the  $z$ -axis in a counterclockwise direction. Such a rotation may be caused, e.g., by a strong component of the incident flow velocity towards Saturn, or by fluctuations of the magnetic field as were observed during T63.

### 4.5.1 T75 split signatures

The T75 trajectory is almost identical to the T9 trajectory (cf. Figure 4.1), located far downstream ( $C/A$  at  $3.9 R_T$ ) in the equatorial plane ( $z = 0$ ). The ambient magnetospheric field during the T75 encounter was heavily disturbed (even more so than during T63) by multiple crossings of Saturn's magnetospheric current sheet through Titan's orbital plane, near closest approach (cf. Figure 3 in Simon et al. (2014)). Under these circumstances,

a simulation of this encounter (using a stationary background magnetic field) is not very meaningful. However we have already shown that the filamentation of Titan's tail is a common feature. The fluctuations in the magnetic background field (corresponding to rotations of the tail structures) may even be beneficial for a split tail detection (see also Simon et al. (2014)). The changes in the magnetic field can sweep a single filament back and forth over the spacecraft's trajectory, making Cassini detect the same structure twice or rotate additional filaments into the plane of the spacecraft trajectory.

## 4.6 Summary

In this chapter, we applied our hybrid model of Titan's plasma interaction to obtain an understanding of the split signatures which were detected in Titan's tail during the T9, T63 and T75 encounters. Our major findings are as follows:

- Spatial inhomogeneities and filamentation of Titan's tail, which allow the detection of split signatures along an appropriate flyby trajectory, are a common feature of the moon's plasma interaction. The filamentation is most pronounced in a plane through the center of Titan which is perpendicular to the magnetic field as well as in a plane that contains the center of Titan and  $\underline{B}_0$  and  $\underline{u}_0$ .
- The collisional deceleration of the plasma, the strong density gradients near Titan and the deflection of ions from the ramside around Titan are mainly responsible for the observed filament structures. Ions of all species are accelerated radially away from Titan due to the pressure gradient force and then escape along trajectories aligned with the draped magnetic field. Similar to cometary plasma interactions, the pressure gradient force leads to an increased size of the obstacle to the incident plasma flow, which allows the filaments to separate from each other and to form the cone structure as well as the outer filaments of the light species.
- Light ions (1,2 amu) escape along draped field lines into the magnetic lobes and form the outer filaments of the split tail that have a crescent-like shape in the plane perpendicular to  $\underline{u}_0$ . These filaments are most pronounced in a plane through the center of Titan, containing  $\underline{u}_0$  and  $\underline{B}_0$  (i.e. the plane whose normal vector is  $\underline{E}_0$ ). In the direction of the convective electric field, these filaments are much less prominent.
- Transport of ions from the ramside to the wakeside produces a cone structure behind Titan: at the surface of the cone the ions are clustered into filaments with a thickness of 1-2  $R_T$ , and inside of the cone the density is reduced. The cone's apex denotes the point where these filaments merge into a single plasma tail. This effect is seen for all ionospheric species. In the plane perpendicular to the magnetic field, this structure is asymmetric towards the direction of  $\underline{E}_0 = -\underline{u}_0 \times \underline{B}_0$ , where it frays out due to the cycloidal motion of the pick-up ions.
- The locations and densities of the filaments strongly depend on the upstream flow parameters and the orientation of the dayside ionosphere with respect to the incident flow. They are easy to miss by Cassini.

- The T9 observations can be qualitatively explained by a crossing of Cassini through the Saturn-facing filament of the cone structure in the first event, and a subsequent crossing through the Saturn-averted outer filament of the light species in the second event. The upstream magnetic field orientation during T9 was beneficial for the detection of these filaments (flyby plane nearly coincident with the  $\underline{u}_0 \times \underline{B}_0$  plane, where the outer filaments of the light species are most pronounced).
- The T63 observations are consistent with a crossing of Cassini through the cone region. The detection of heavy ions in both events of the split signature supports this further. For T75, a double-detection of the same tail filament is a possible explanation, due to rotations of the tail by the large fluctuations in the ambient magnetic field. Likewise, it is possible that those fluctuations simply rotated two separate filaments into the spacecraft trajectory.

Although the Cassini Plasma Spectrometer ceased to operate in mid 2012 (Smith and Rymer (2014)), future studies of possible split signatures in Titan's tail can be performed by using electron and ion data from the RWPS and INMS instruments. These instruments have been used successfully in the past to identify interesting features of electrons and outflowing ions in Titan's upper ionosphere and the tail region (e.g. Edberg et al. (2010), Westlake et al. (2012)).



# 5 Titan in the Supersonic Solar Wind

The following chapter has been published in wide parts before submission of the thesis. The copyright holder of the pre-publication is the American Geophysical Union, and the cited parts are reprinted with permission. The publication can be found under the following reference:

**Feyerabend, M.**, S. Simon, F. M. Neubauer, U. Motschmann, C. Bertucci, N. J. T. Edberg, G. B. Hospodarsky, and W. S. Kurth (2016), Hybrid simulation of Titan's interaction with the supersonic solar wind during Cassini's T96 flyby, *Geophys. Res. Lett.*, 43, 35-42, <http://dx.doi:10.1002/2015GL066848>

## 5.1 Introduction

For average solar wind conditions, Titan is located within the outer regions of Saturn's magnetosphere (Bertucci et al. 2009), exposed to the subsonic Kronian magnetospheric plasma. However, in times of enhanced solar wind dynamic pressure Titan may be located in the magnetosheath or even upstream of Saturn's bow shock, interacting with shocked/unshocked solar wind plasma (see figure 5.1). However, out of the 117 Cassini

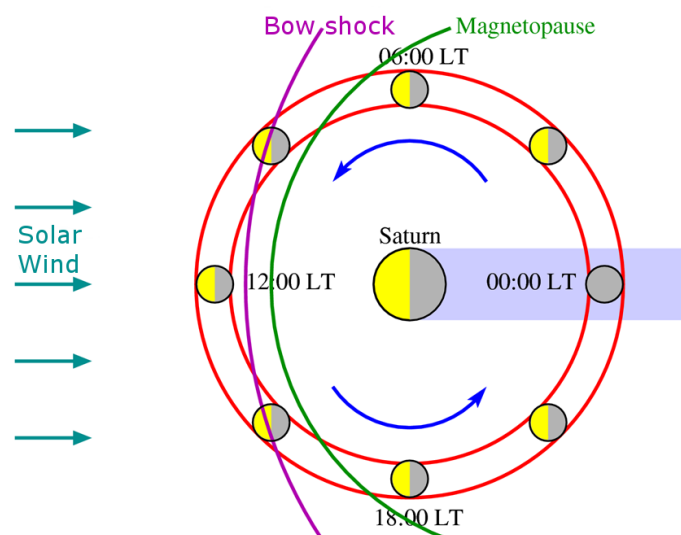


**Figure 5.1:** If the Solar wind dynamic pressure is enhanced above normal levels, Saturn's magnetopause gets pushed towards the planet and may cross Titan's orbit. When Titan is located near the noon sectors around 12 LT, it may therefore be embedded in Saturn's magnetosheath or even in the Solar wind in front of Saturn's bow shock.

flybys so far, only three took place while Titan was located in Saturn's magnetosheath during or prior to the encounter (Rymer et al. 2009, Simon et al. 2013). The first of them was the T32 encounter on 13 June 2007. Magnetic field observations from this flyby provided initial confirmation of the existence of fossilized magnetic fields in the convection-dominated region of Titan's ionosphere (Bertucci et al. 2008). Fossilized field lines are 'trapped' in the ionosphere between altitudes of 1800-1000km due to the low plasma velocity of 0.1-1 km/s in this region, compared to  $\sim 100$ km/s upstream of Titan (Neubauer et al. 2006) (see section 2.4).

The second flyby that showed an ambient plasma environment belonging to the magnetosheath was the the T42 encounter on 25 March 2008. The magnetic field observations of this encounter showed an unusually strong pileup of the magnetic field of up to 37 nT near the closest approach, which is higher than found during any other flyby (before and after T42) (Wei et al. 2011). Also the strongest magnetic field component in the pileup region was the  $B_x$  component, which is incompatible with the draping signature of the mainly southward oriented magnetic field that was observed upstream of Titan. Wei et al. (2011) thus suggested that the strong pileup was caused by fossilized magnetic field flux tubes from the magnetosheath that began to twist under the influence of a retreating magnetosphere.

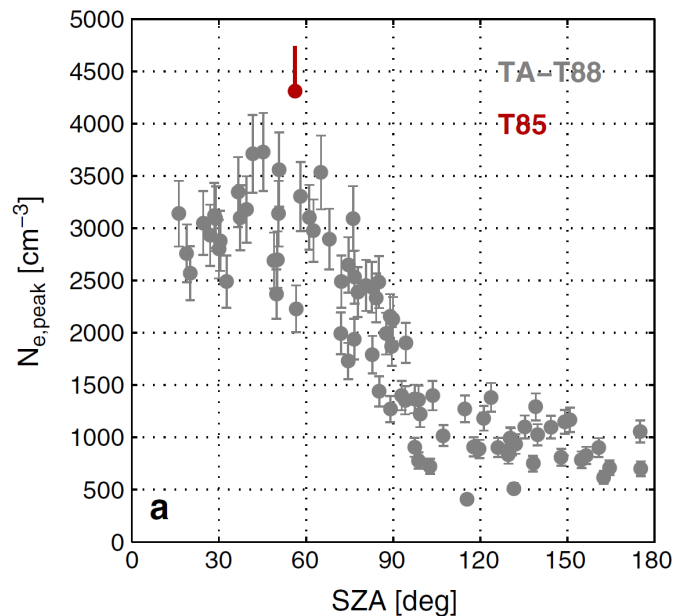


**Figure 5.2:** The ionospheric peak electron density as a function of the Solar zenith angle for all flybys from TA-T88. The T85 flyby, marked in red, shows the highest electron density of all these flybys. The average peak electron density in Titan's ionosphere is in the range of  $2500$ - $3500$   $\text{cm}^{-3}$ . The Figure from Edberg et al. (2013)

The third Titan flyby in Saturn's magnetosheath was the T85 encounter on 24 July 2012. Prior to this encounter, a coronal mass ejection event impacted on Saturn's magnetosphere, which lead to multiple crossings of Saturn's magnetopause over Titan's orbital location, exposing the moon to the shocked plasma of Saturn's magnetosheath for about 3 hours (Edberg et al. 2013). During T85 the Cassini Langmuir Probe (LP) detected the

highest electron densities ever measured in Titan's ionosphere with a maximum of  $4310 \text{ cm}^{-3}$  (see figure 5.2). It was suggested that this was caused by the increased impact ionization in Titan's ionosphere due to more abundant energetic magnetosheath protons that were added by the CME event (Edberg et al. 2013).

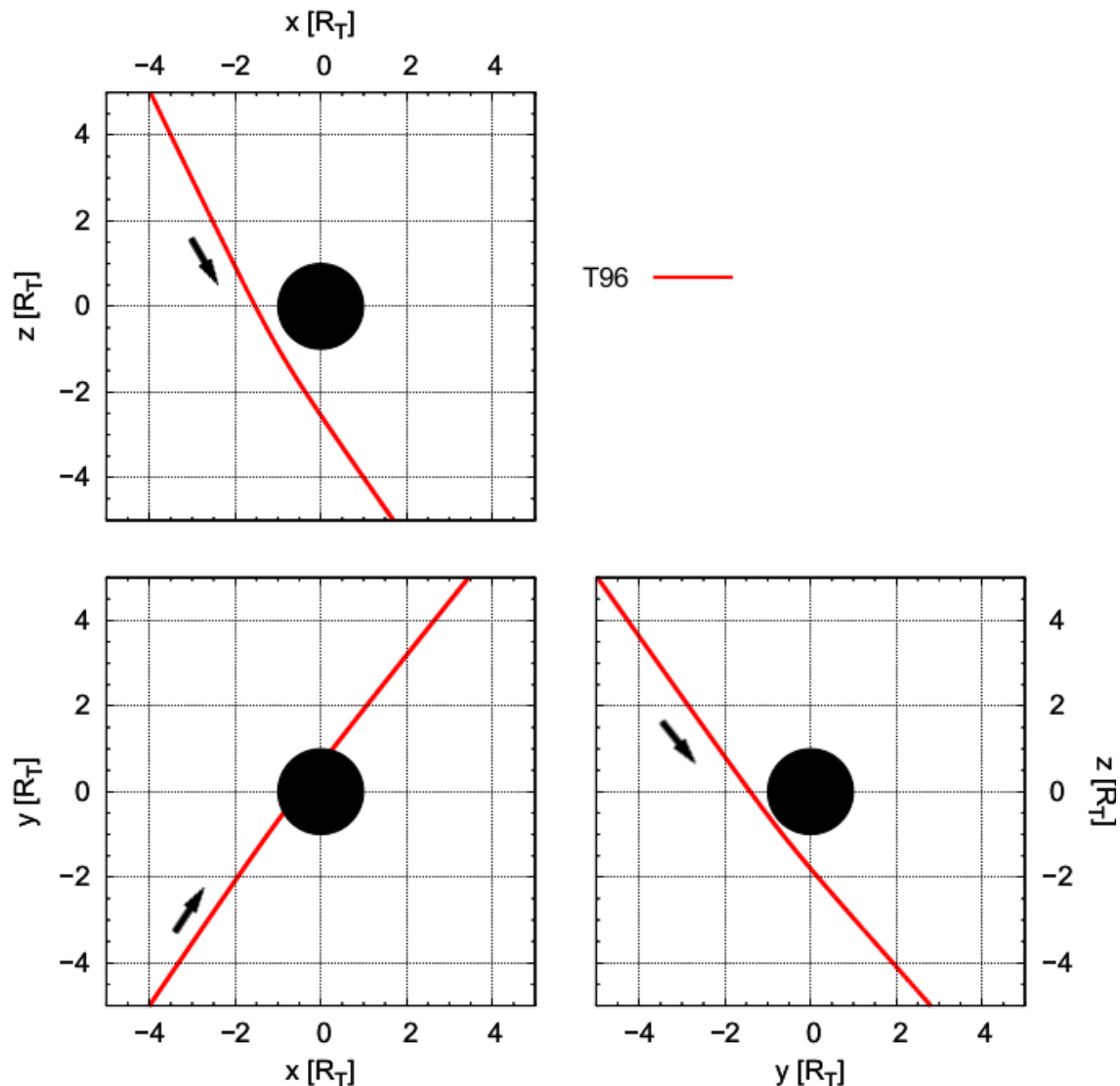


**Figure 5.3:** Cassini's trajectory during the T96 encounter in TSWIS coordinates. The arrows indicate the Cassini's direction in each plane. The  $-x$  axis points towards the Sun and the  $y$  axis points in the direction of Saturn's orbital motion.

The T96 encounter on 01 December 2013 (closest approach altitude of 1400 km at 00:41, 12.4 local time) constitutes the first and only event of the entire Cassini mission where Titan was embedded in the supersonic solar wind upstream of Saturn's bow shock (Bertucci et al. 2015). Titan's plasma interaction with the Solar wind suggests a change of coordinates into a more convenient system than the TIIS frame for this case. Therefore we change from the TIIS frame into the more natural Titan-centered solar wind interaction system (TSWIS) introduced by Bertucci et al. (2015) for the remainder of this chapter. The TSWIS system can be achieved by a simple rotation of the TIIS system.

In the TSWIS frame, the  $-x$  axis points towards the Sun, the  $y$  axis points in the direction of Saturn's orbital motion and the  $z$  axis completes the right-handed system. The trajectory of Cassini for this encounter is plotted in figure 5.3. During T96, Cassini was moving mainly in a north-south direction and towards Saturn, approaching Titan from the upstream side and from high northern latitudes, with a superimposed motion in the  $+y$  direction. Thus Cassini's path for T96 intersects with the upstream interaction region

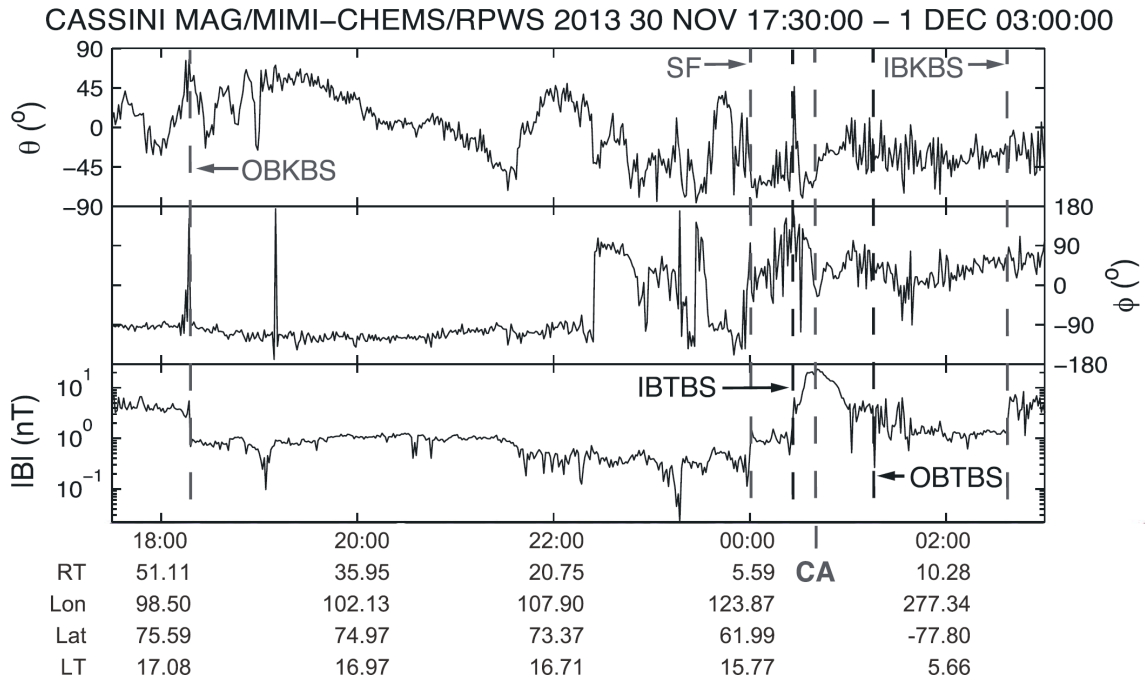


**Figure 5.4:** Long term magnetic observations of the T96 encounter. The magnetic field is plotted in spherical TSWIS coordinates ( $\theta$ ,  $\phi$ ,  $|B|$ ). Saturn's bow shock (OBKBS) was crossed by Cassini after 18:00 on the previous day. In the following 6 h interval Cassini is located inside the Solar wind. Prior to the shock front (SF) at 00:00, the magnetic field was predominantly west-east oriented ( $\phi \approx -90^\circ$ ). After the crossing of the shock front the magnetic field assumes a mainly north-south orientation ( $\theta > -45^\circ$ ) until entering the Titan interaction region. The inbound and outbound crossings of Titan's bow shock are marked by IBTBS and OBTBS. Figure from Bertucci et al. (2015).

of Titan and the Solar wind. Magnetic field observations covering a  $-7/+2$  hour interval around closest approach are shown in figure 5.4. About 6 hours prior to the encounter, Cassini crossed Saturn's bow shock (indicated as OBKBS) in that plot, which is accompanied by a strong jump in the magnetic field strength of one order of magnitude afterward. Ion measurements also showed a strong decrease in particle counts (Bertucci et al. 2015). The magnetic field strength remained at very low levels for about 6 hours, indicating that Titan was exposed to the unshocked high pressure solar wind plasma during that time interval. About 2 hours before closest approach Cassini crossed a sector boundary in the solar wind as indicated by the change in direction of the  $B_\phi$  component of about  $180^\circ$  shortly after 22:00, followed by significant fluctuations in the direction and magnitude of the solar wind magnetic field. From around 00:00 on, these perturbations weakened significantly after the crossing of a shock front (SF), with the solar wind magnetic field

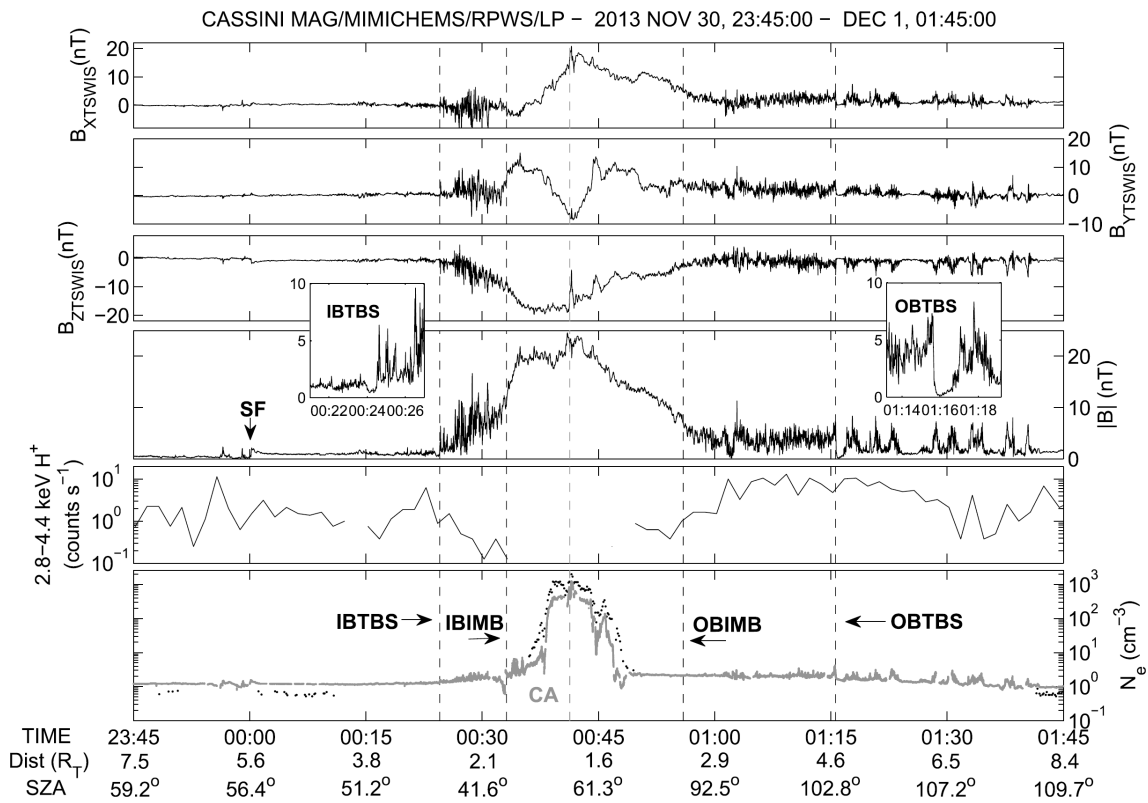


**Figure 5.5:** The top four panels show the  $B_x$ ,  $B_y$ ,  $B_z$  components and magnitude  $|B|$  of the magnetic field in cartesian TSWIS coordinates. The last panel shows the electron densities  $n_e$  that are derived from the Radio and Plasma Wave Science (RPWS, dotted) and Langmuir Probe (LP, grey curve) instruments. The crossing of Titans inbound and outbound bow shock is marked by IBTBS and OBTBS, respectively. IBIMB and OBIMB denote the crossing of Titan’s inbound and outbound induced magnetosphere boundary. Figure from Bertucci et al. (2015).

changing from a predominantly west-east orientation to a predominantly north-south orientation. Although this event is apparently not related to Titan, its nature is not yet understood (Bertucci et al. 2015).

Figure 5.5 provides a closer look on the magnetic field and electron observations in a  $\pm 1$  interval centered around the closest approach at 00:41. The plasma and magnetic data obtained from Titan’s interaction region revealed similar features as known from the induced magnetospheres of Mars and Venus, including the formation of a bow shock (IBTBS and OBTBS in the figure) and a magnetic barrier at Titan’s ramside (IBIMB and OBIMB). The bow shock is a result of the subsonic nature of the impinging Solar wind. However the pileup of the magnetic field at closest approach was found to be too large ( $\sim 25$ nT) compared to upstream values of  $\sim 1$ nT) to be consistent with the dynamic pressure of the upstream solar wind in the 40 minutes after Cassini’s crossing of SF and closest approach: for the assumption of a simple pressure balance between the magnetic pressure in the pileup region and the solar wind dynamic pressure  $B_{max}^2/(2\mu_0) = 0.88 \rho_{sw} u_{sw}^2 \cos(SZA)$  (Dubinin et al. 2006), where  $u_{sw}$  is the solar wind bulk velocity,  $\rho_{sw}$  the solar wind mass density and SZA is the solar zenith angle at the location of the magnetic field strength

maximum  $B_{max}$ , a solar wind dynamic pressure of 0.64 nPa was derived for T96 (Bertucci et al. 2015). However, the dynamic pressure that was derived from the plasma observations was only 0.12 nPa. Bertucci et al. (2015) proposed that the fossilization of magnetic field lines in Titan’s ionosphere from the pre-SF solar wind plasma with higher dynamic pressure may be responsible for the large magnetic pileup.

Since Cassini’s remaining Titan flybys (T118-T126) will all take place in Saturn’s downstream region, T96 will remain the only case of Titan being observed in the supersonic solar wind. In this chapter we model Titan’s plasma interaction with the solar wind during T96 using our hybrid model, and compare our results against Cassini magnetic field and electron data. We investigate the possible contribution of fossilized fields to the observed magnetic field perturbations and study the robustness of Titan’s induced magnetosphere against the observed non-stationarities in the incident solar wind conditions.

## 5.2 Simulation Parameters

Five simulations with different upstream parameters are discussed for the simulation of Titan’s plasma interaction with the solar wind. A summary of the parameters for each run is provided in Table 5.1. All simulations have been performed using a cubic  $-4 R_T < x, y, z < 4 R_T$  box with a maximum resolution of 80 km in Titan’s ionosphere. The upstream solar wind bulk velocity  $\underline{U}_0$  is parallel to the  $x$  axis in all runs. There are two main differences between the parameters of the five simulations. First, the orientation of the upstream magnetic field is chosen to correspond to the different magnetic field regimes observed during the encounter: inbound and outbound of closest approach as well as upstream of the shock front (SF) Cassini encountered about 40 minutes before the flyby. The averaging intervals for the different magnetic field vectors are noted in Table 5.1. Second, the dynamic pressure of the incident solar wind is treated as a free parameter to achieve best possible agreement between simulation results and Cassini observations of magnetic field and electron density.

The solar wind in run #1 has the lowest dynamic pressure (0.24nPa), comparable to the pressure estimated from Cassini observations downstream of SF between 00:01 and 00:23 (Bertucci et al. 2015). The parameters of run #2 are identical to those of run #1 apart from a higher dynamic pressure of 0.64nPa, which was obtained by changing the density and velocity of the incoming solar wind protons. Runs #3, #4 and #5 apply an even more enhanced dynamic pressure (1.5nPa). The upstream magnetic field vector in runs #1– #3 has been calculated from the interval after the crossing of SF (00:01) and Cassini’s entry into the Titan interaction region (00:23). Run #4 applies a magnetic field vector obtained from the outbound segment of the Cassini encounter, but before the spacecraft crossed Saturn’s bow shock and left the supersonic solar wind (cf. figure 2 of Bertucci et al. (2015)). The outbound field has a north-south and east-west orientation and forms an angle of  $32^\circ$  with the inbound magnetic field, another piece of evidence for non-stationary behavior.

Run #5 represents the magnetic conditions of the pre-SF regime, where the interplanetary magnetic field pointed mostly in the west-east direction (time interval 23:35-23:55 on 30 November 2013). The pre-SF field was also about a factor of 2 weaker than the post-SF field. Cassini left the pre-SF regime about 40 minutes before closest approach and therefore, Titan was not directly exposed to these upstream conditions at the time of

the encounter. However, fossilized magnetic fields from the pre-SF regime may still have been trapped in Titan's ionosphere when Cassini passed by the moon (Neubauer et al. 2006). Due to computational constraints on the simulation run time, a hybrid code cannot resolve the real-time evolution of putative fossilized fields over 40 minutes (see also Müller et al. (2010)). Besides, any realistic inclusion of the magnetic field transition at SF in a local plasma simulation needs to fulfill the  $\nabla \cdot \underline{B} = 0$  condition across the discontinuity. This requires knowledge of the *three-dimensional* structure of the magnetic field on both sides of SF (Simon et al. 2009a), which could not be measured by a single spacecraft. However, run #5 will illustrate the stationary structure of Titan's induced magnetosphere in the pre-SF regime and can therefore facilitate the identification of fossilized field signatures in T96 data.

The high dynamic pressures and Mach numbers of the solar wind used for the simulations (see table 5.1) are motivated by the extreme upstream conditions during T96: the fact that Titan was located upstream of Saturn's bow shock for several hours indicates that the solar wind pressure was enhanced above usual levels. Very high Mach numbers of the solar wind have been observed during several Cassini crossings of Saturn's bow shock and the values used for our simulations are consistent with the observed values (Masters et al. 2011, Sulaiman et al. 2015).

Quantity	Run #1	Run #2	Run #3	Run #4	Run #5
Solar wind density $n_{0,H^+}$ [ $\text{cm}^{-3}$ ]	0.7	1.9	1.5	1.5	1.5
Solar wind velocity $U_0$ [km/s]	460	450	770	770	770
Dynamic pressure $p_0$ [nPa]	0.24	0.64	1.5	1.5	1.5
Magnetic field strength $B_0$ [nT]	0.85	0.85	0.85	1.13	0.42
Magnetic field vector $\underline{B}_0/B_0$	(0.3,0.36,-0.88)	(0.3,0.36,-0.88)	(0.3,0.36,-0.88)	(0.66,0.54,-0.51)	(0.15,-0.94,0.1)
Averaging Interval for $\underline{B}_0$	Dec 1 00:01-00:23	Dec 1 00:01-00:23	Dec 1 00:01-00:23	Dec 1 01:55-02:35	Nov 30 23:35-23:55
Upstream Proton Gyroradius [ $R_T$ ]	2.19	2.14	3.66	2.75	7.42
Alfvén Mach Number $M_A$	21	33	51	38	123
Magnetosonic Mach Number $M_{MS}$	13	19	31	27	37
Description	low pressure inbound field Green	intermediate pressure inbound field Orange	high pressure inbound field Red	high pressure outbound field Violet	high pressure pre-SF field Blue
Color					

**Table 5.1:** Plasma parameters of the simulation runs. The solar wind is assumed to consist of protons and electrons in all cases. An electron and proton temperature of 1eV is used for the solar wind plasma.

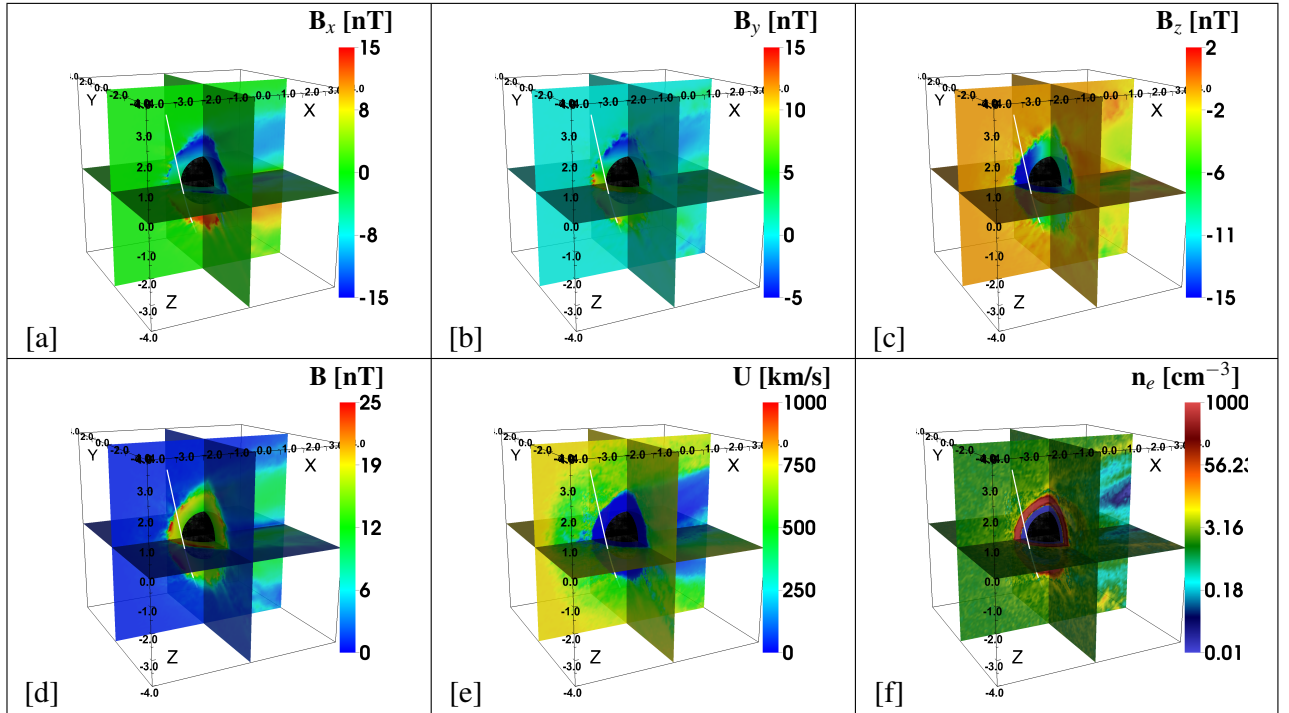


**Figure 5.6:** Plasma quantities of run #3 in the  $x = 0$ ,  $y = 0$  and  $z = 0$  planes. (a)-(d) Magnetic field components and magnitude, (e) plasma bulk velocity, (f) electron number density. The T96 trajectory is represented by the solid white line.

### 5.3 Model Results and Discussion

A three-dimensional overview of the magnetic field components, the plasma bulk velocity and the electron number density for run #3 is given in figure 5.6, where we also indicate the Cassini trajectory. The plasma quantities from run #3 are also plotted in figure 5.7 for two planes which are referred to as the *flyby plane* and the *gyro plane*. The flyby plane contains the center of Titan as well as the Cassini trajectory, while the gyro plane is defined by the center of Titan, the undisturbed upstream velocity vector  $\underline{U}_0$  and the convective electric field vector  $\underline{E}_0 = -\underline{U}_0 \times \underline{B}_0$ . Since the upstream magnetic field  $\underline{B}_0$  is mainly north-south oriented,  $\underline{E}_0$  is almost aligned with the  $-y$  axis.

Figures 5.6 and 5.7 show the general structure of Titan's induced magnetosphere, which includes a bow shock (e.g. figure 5.6(d)) and a magnetic barrier of enhanced field strength on the ramside. The plasma velocity is greatly reduced in the vicinity of Titan due to the mass loading with freshly produced ionospheric and exospheric ions (figures 5.7(e,k)). The location of Titan's bow shock overlaps with the extended mass loading region on the ramside. The filamented structure of the plasma quantities (e.g. figures 5.7(c,e,f)) on the upstream side of the bow shock is an indication of reflected solar wind particles (see also Bößwetter et al. (2004)). Runs #1, #2 and #4 yield qualitatively similar results as run #3, with mostly quantitative differences. Therefore, no two-dimensional cuts are displayed for these runs.

Figure 5.8 compares the modeled magnetic field components  $\underline{B} = (B_x, B_y, B_z)$  and the electron number density  $n_e$  from all 5 simulation runs against observations from the

Cassini magnetometer (Dougherty et al. 2004) and the electron number density, inferred from Langmuir Probe data and measurements of the upper hybrid frequency by the Radio and Plasma Wave Science Instrument (RPWS, Gurnett et al. (2004)). As can be seen, the magnitude and extension of the field perturbations in  $B_x$ ,  $B_z$  and  $|\underline{B}|$  are reasonably well reproduced by runs #2 to #4. The model also succeeds in reproducing the two maxima of the M-like perturbation signature seen in  $B_y$ . In addition, the location, magnitude and width of the electron density enhancement observed near closest approach are in excellent quantitative agreement with the output of model runs #3, #4 and #5.

Since the upstream magnetic field pointed mainly in the north-south direction, the draping pattern shows a negative  $B_x$  component in the northern ( $z > 0$ ) and a positive  $B_x$  component in the southern ( $z < 0$ ) hemisphere, as can be seen in figures 5.6(a) and 5.7(a). However, due to the non-zero  $B_{0,x}$  and  $B_{0,y}$  components of the upstream field the draping pattern is slightly asymmetric with respect to  $z = 0$  and also features a weak  $B_y$  perturbation. Cassini only grazed the outer regions of Titan's northern magnetic lobe in the inbound segment ( $B_x < 0$ , between 00:32-00:36), followed by an extended passage through Titan's southern magnetic lobe ( $B_x > 0$ , between 00:36-00:57). This bipolar feature in  $B_x$  is found in all simulation runs that use an upstream magnetic field from a time interval close to the encounter (runs #1 to #4, figure 5.8).

The spacecraft did not penetrate below the magnetic ionopause, since no dropout of the magnetic field strength was observed near closest approach. This is consistent with our simulations (see figures 5.7(d) and 5.8). Since the flyby took place in Titan's upstream region, Cassini did not intersect the wakeside plasma tail of Titan nor regions of enhanced ion outflow in the plane perpendicular to the upstream magnetic field (see figures 5.6 and 5.7(k,l)).

As can be seen in figure 5.8, the low pressure run #1 produces draping and pileup signatures that are *qualitatively* consistent with the observations. However, the magnitude of the modeled field enhancement is not large enough to explain the data ( $|\underline{B}| < 15\text{nT}$  in the model compared to the observed maximum value of  $|\underline{B}| \sim 25\text{nT}$  at 00:41). In addition, the modeled electron density enhancement in run #1 is too broad to be consistent with the observed density pattern. Only the peak density is of the same magnitude as observed. Thus, the low-pressure upstream conditions of run #1 are not able to quantitatively explain the data and indicate that a higher dynamic upstream pressure is needed.

Run #2 therefore applies a higher upstream pressure of 0.64nPa, which was proposed by Bertucci et al. (2015) based on pressure balance calculations for Titan's magnetic barrier. Figure 5.8 shows that this increased upstream pressure yields a much better agreement with the magnetic field observations. Yet, while the magnitude of the observed electron density enhancement is again well reproduced, the modeled electron density signature is still too broad. It should be noted as well that the chosen upstream magnetic field (from the segment after the SF) in general leads to a positive  $B_y$  perturbation along the Cassini trajectory that cannot explain the dip in the middle of the observed M-shaped  $B_y$  signature. The reasons for this discrepancy will be discussed later.

Another increase in the solar wind dynamic pressure to 1.5nPa in run #3 (also used in runs #4 and #5) is able to push the region of enhanced ionospheric electron density further towards the moon, thereby yielding excellent agreement with the observed box-like density enhancement. We note again that runs #1 to #3 use the upstream magnetic field obtained from the inbound part of the encounter, i.e., between the crossing of SF and closest ap-

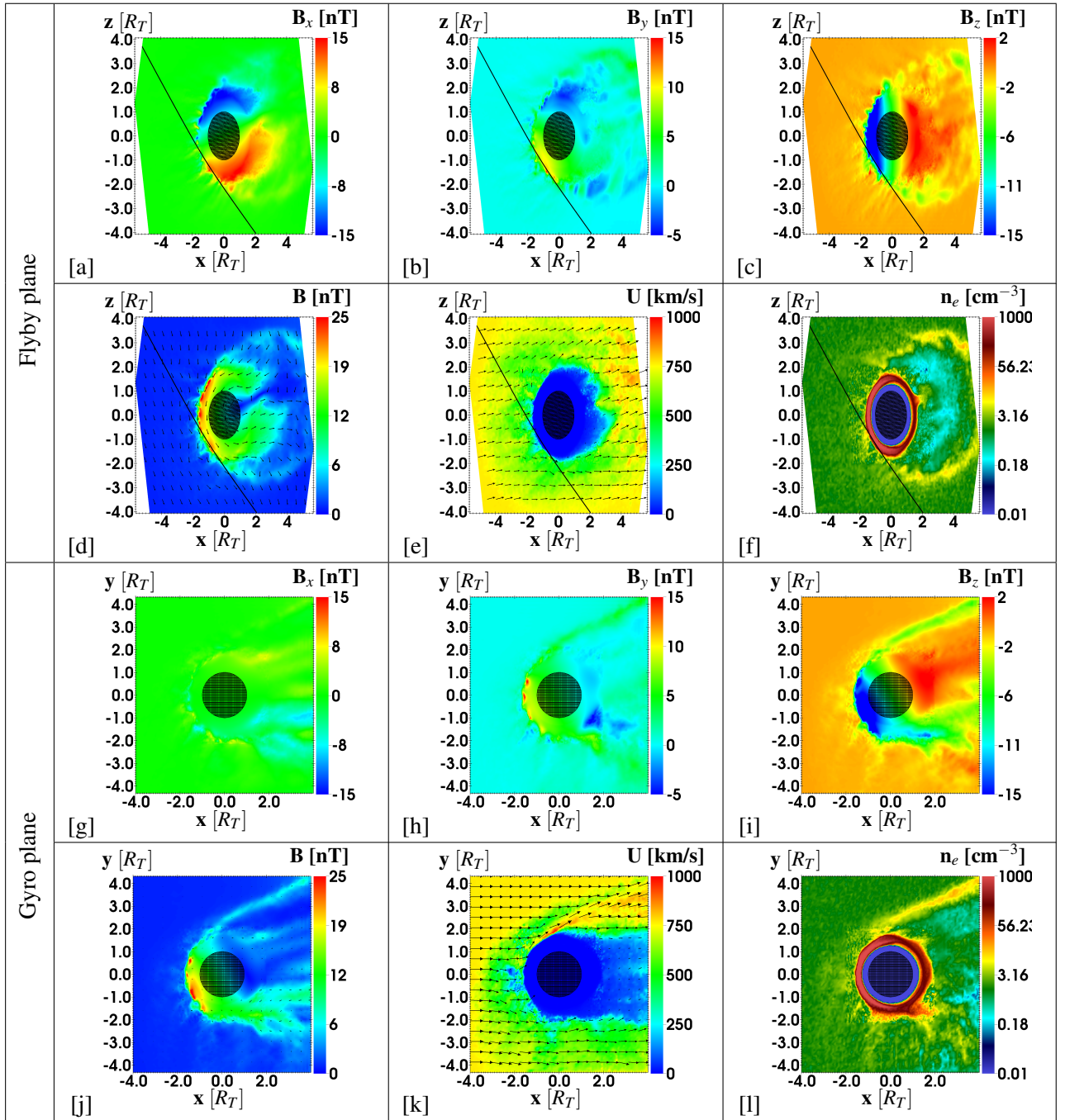


**Figure 5.7:** Plasma quantities of run #3 in the flyby and gyro plane. (a)-(d),(g)-(j) Magnetic field components and magnitude, (e),(k) plasma bulk velocity, (f),(l) electron number density. Arrows denote the projection of the respective vector field on the cutting plane. The non-rectangular shape of the flyby plane arises from its inclination against the coordinate axes in the cubic simulation domain.

proach.

To investigate the effects of the observed rotation of the ambient solar wind magnetic field during the encounter, in run #4 an upstream magnetic field obtained from the outbound segment was applied (cf. table 5.1). As can be seen in figure 5.8, this leads to only minor quantitative changes in the modeled magnetic field components. The modeled electron density is almost identical to run #3 as well. Using the outbound magnetic field yields slightly better agreement between modeled and measured  $|B|$  in the outbound segment of the flyby, whereas the inbound field in run #3 gives better agreement with the inbound draping pattern in  $B_x$  than run #4. Overall the magnetic and density features in both runs look very similar. Both, run #3 and #4 produce a plateau-like enhancement in  $B_y$ . The width of this plateau agrees well with the width of the observed perturbation region in  $B_y$ . The magnitude of the modeled  $B_y$  enhancement is consistent with that of the two spikes seen in  $B_y$  by the magnetometer.

Hence, runs with a high solar wind pressure and an upstream magnetic field obtained from a time interval *after* the SF are able to quantitatively reproduce numerous key features of the observed magnetic field signatures as well as the magnitude and width of the electron density enhancement around closest approach to Titan. Overall, the simulated interaction signatures along the T96 trajectory exhibit a high level of robustness against the observed changes of the incident flow conditions. Since we use the solar wind dynamic pressure as a free parameter to achieve best possible agreement between model and data, similar results could also be obtained by using a different combination of solar wind density and flow speed. The density value used in runs #3, #4 and #5 is consistent with LP data and differs by only about 20% from the electron density inferred from the upper hybrid frequency at the edges of Titan's ionosphere. The only feature of the observed magnetic field signature that could not yet be explained is the dip in the middle of the M-structure seen in  $B_y$  around closest approach between 00:38 and 00:44. In this region, the  $B_y$  component drops from positive values of about  $\sim 10$ nT at the two 'spikes' of the M to negative values with a minimum of  $-7$ nT at closest approach.

The draping of the north-south oriented solar wind magnetic fields from runs #1 to #4 generates a plateau-like positive  $B_y$  perturbation near closest approach. However, this plateau is only consistent with the observations at the two outer spikes of the M-signature between 00:33 and 00:38 as well as 00:44 and 00:50 where the observed  $B_y$  is also positive.

Since the previously used upstream magnetic field vectors give good agreement in all components except for the inner dip of the M-signature in  $B_y$ , it is unlikely that this feature could be caused by, e.g. short-scale fluctuations or a different geometry of the upstream magnetic field and plasma bulk velocity. Given that  $B_y$  drops by about 17nT in the center of the M-signature, one would then expect to see related perturbations in the other magnetic field components as well.

The extent of the dip in  $B_y$  is symmetric around closest approach at 00:41 and covers altitudes of 1800km to 1400km. Due to the combination of low plasma velocity and sufficiently large magnetic Reynolds number, this altitude regime of Titan's ionosphere may store fossilized magnetic field lines most efficiently (Neubauer et al. 2006). Bertucci et al. (2008) suggest the lifetimes of such fossilized field signatures to range between 20 minutes and up to 3 hours. Hence, we propose that remnants of a previously encountered upstream magnetic field configuration are responsible for the inner dip of the M-feature

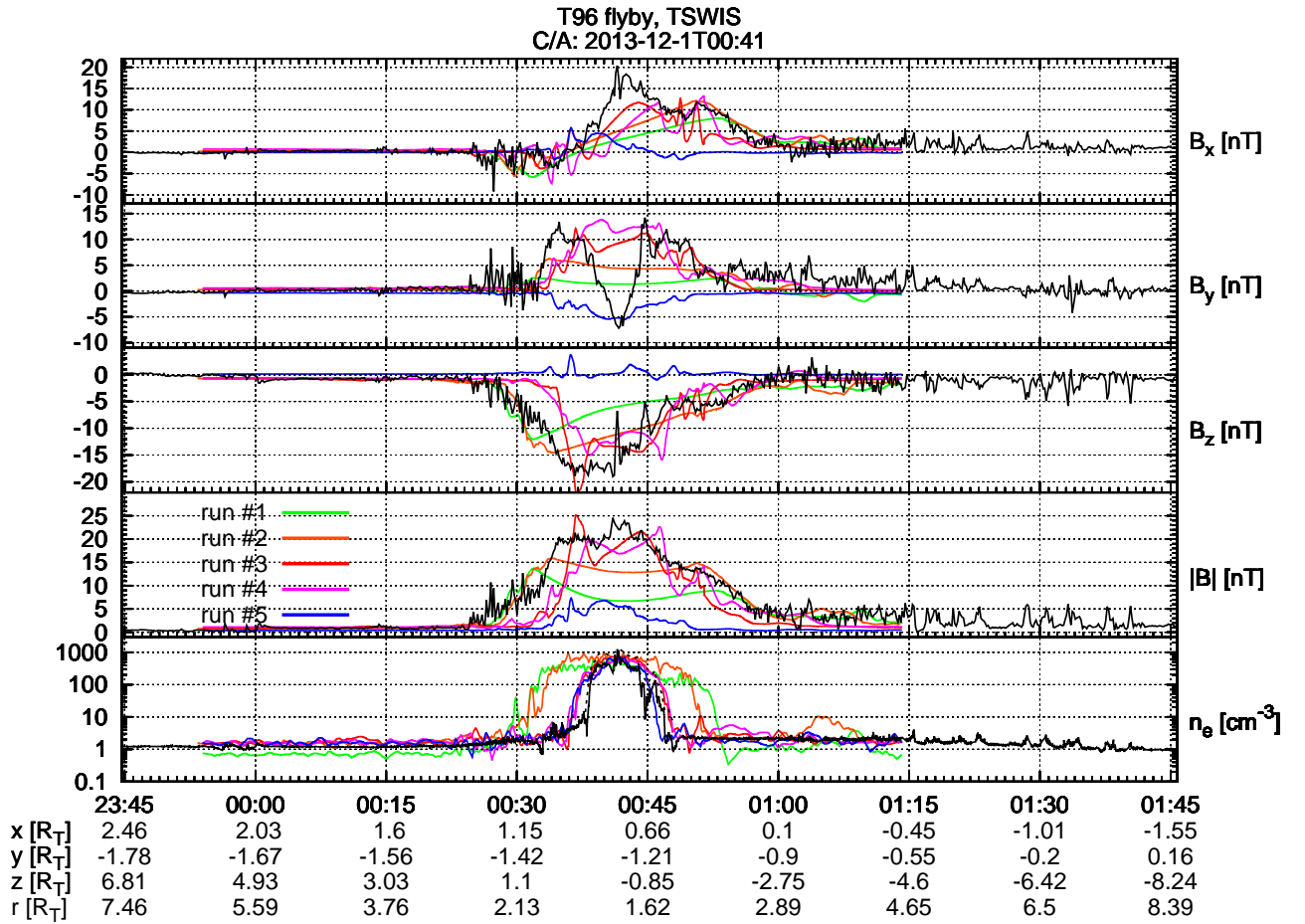


**Figure 5.8:** Modeled magnetic field components ( $B_x$ ,  $B_y$ ,  $B_z$ ) and electron number density  $n_e$  for all five runs compared against the T96 Cassini observations. Observations are displayed in black. For the electron density data, the solid black line refers to LP data while the dashed black line refers to densities obtained from the upper hybrid frequency. TSWIS coordinates and distance  $r$  to Titan's center of Cassini during the flyby are displayed for their respective time points.

in  $B_y$ .

To substantiate this hypothesis, the upstream magnetic field in run #5 was obtained from the interval immediately prior to Cassini's crossing of the SF (23:35-23:55 on 30 November 2013, cf. figure 2 in Bertucci et al. (2015)). In this regime the magnetic field vector possessed a strong west-east ( $-y$ ) component. Compared to runs #1 to #4, Titan's magnetic lobes in such an upstream field are rotated around the  $x$  axis by  $90^\circ$  and can now be found in the  $y < 0$  and  $y > 0$  half spaces. The ramside magnetic barrier is mainly visible in the  $B_y$  component. As can be seen in figure 5.8, this upstream field therefore results in a broad negative  $B_y$  perturbation along Cassini's trajectory with a minimum value of  $B_y \approx -5\text{nT}$  around closest approach. The strength and orientation of this negative  $B_y$  perturbation are in agreement with Cassini observations at the "bottom" of the M-like signature. The perturbations in the  $B_x$  and  $B_z$  components are much smaller than in runs #1 to #4. Especially, around closest approach the  $B_x$  and  $B_z$  components from run #5 are almost completely undisturbed. For this reason, we do not expect to see strong residual

fossilized field signatures from the pre-SF regime in  $B_x$  and  $B_z$ , which is consistent with the observations.

Above altitudes of 1800 km, Titan's induced magnetosphere can adapt to a change of the ambient magnetic field orientation from west-east (pre-SF) to north-south (post-SF) on time scales of only a few minutes (Simon et al. 2009a). Thus, the outer layers of the magnetic pile-up region are quickly eroded through convection and reconnection by such a rotation of the upstream field. However, the pre-SF pile-up at Titan's ramside (mainly visible in  $B_y$  and *not* in  $B_z$ ) may prevail at altitudes below 1800 km for several hours. We therefore propose that draped field lines from the pre-SF regime were still present in Titan's lower ionosphere at closest approach (i.e., 40 minutes after Cassini's crossing of SF) and gave rise to the inner dip of the M-like signature in  $B_y$ .

Although the reconfiguration of Titan's induced magnetosphere during a rotation of the upstream magnetic field is a highly non-linear process, the low convection speeds in the moon's deep ionosphere shield the magnetic draping pattern in that region to a certain degree against changes in the incident flow conditions (Neubauer et al. 2006, Bertucci et al. 2008, Simon et al. 2009a). We note that the "summit" of the observed  $B_x$  draping pattern (which we could not quantitatively reproduce, see figure 5.8) is located at the same position as the proposed fossilized magnetic field signature in  $B_y$ . It is very well possible that this overshoot in  $B_x$  arises from the deformation of the fossilized field lines between the time of their "capture" and the time of their subsequent detection by Cassini.

### 5.4 Concluding Remarks

Our simulations show that the outer part of Titan's induced magnetosphere at the time of T96 is consistent with the picture of a quasi-stationary interaction between the moon's ionosphere and a high-pressure solar wind flow. However, we also provide strong evidence that the fine structure of the magnetic field in Titan's deep ionosphere was governed by fossilized magnetic field lines. These field lines could have been "trapped" in Titan's ionosphere at least 40 minutes before the T96 encounter took place. A lifetime of 40 minutes agrees well with the time window inferred by Bertucci et al. (2008) from the first in-situ detection of fossilized magnetic fields during the T32 magnetosheath excursion.

## 6 Summary and Outlook

In this thesis, the plasma environment of Saturn's largest moon Titan has been studied by using a hybrid model that treats ions as kinetic particles and electrons as a massless charge-neutralizing fluid. The hybrid approach is exceptional suitable for the description of Titan's plasma interaction because it accounts for the effects of large ion gyro radii, which cannot be neglected near Titan. Titan's ionosphere model was significantly improved compared to earlier studies and is modeled by using a 7-species representation of the main observed ion species. The ionosphere is generated via a realistic description of the photoionization of the main neutral species that is based on a wavelength dependent model of the solar EUV radiation, as well as a phenomenological model of electron impact ionization. A network of the most important chemical reactions has been incorporated into the model which is responsible for the conversion of the photo generated species into the remaining ones of the 7-species model. Ion-neutral collisions of the impinging magnetospheric plasma with Titan's neutral atmosphere were also included in our model. For this thesis we focused on a set of unique Cassini Titan flybys which stand out due to their exceptional plasma environment or unexpected observations. In the following we will give a brief summary of our major findings.

In the first part we studied the physical processes that lead to the detection of split signatures in the ion density during several crossings of the Cassini spacecraft through Titan's mid-range plasma tail (T9, T63, and T75). During each of these flybys, the Cassini Plasma Spectrometer observed Titan's ionospheric ion population twice; i.e., the spacecraft passed through two spatially separated regions where cold ions were detected. The major results of this part are:

- The filamentation of Titan's tail that lead to the detection of split signatures during the T9, T63 and T75 flyby is an omnipresent feature of the moons plasma interaction that is closely tied to the upstream geometry of the magnetic field and bulk velocity.
- The filamented structure of the tail is most pronounced in planes that contain Titan's center and 1) which are perpendicular to the magnetic field or 2) contain the upstream magnetic field  $\underline{B}_0$  and bulk velocity  $\underline{u}_0$ .
- The physical processes that are associated with the formation of the filamented tail structure are the transport of ionospheric ions from the ramside to the moon's wakeside, as well as a radial outwards directed motion that is induced by the strong plasma pressure gradient in Titan's ionosphere.
- Ions of all species show a three dimensional cone-like structure in Titan's downstream region: the surface of the cone has a thickness of 1-2  $R_T$  and is formed by

filaments due to the transport of ions from the dayside to the wakeside. Inside the cone the density is reduced compared to its surface.

- Ions of light species (1-2 amu) are brought on trajectories along the draped magnetic lines in the outer layers of the ionosphere by the outwards pointing pressure gradient, which forms an outer filament structure in the tail for only these species.
- All tail structures show asymmetries towards the direction of the convective electric field in a plane perpendicular to the upstream magnetic field.
- The locations and densities of the filaments strongly depend on the upstream flow parameters and the orientation of the dayside ionosphere with respect to the incident flow. Due to their confinement to distinguished planes they are therefore easy to miss by spacecrafts.
- Without the pressure gradient, no filamented tail structure is formed apart from the pick-up tail due to the large ion gyro radii.
- The T9 observations can be qualitatively explained by a crossing of Cassini through the Saturn-facing filament of the cone structure in the first event, and a subsequent crossing through the Saturn-averted outer filament of the light species in the second event. The upstream magnetic field orientation during T9 was beneficial for the detection of these filaments, since the flyby plane nearly coincided with the plane where the light species' outer filament structure is most pronounced.
- The T63 observations are consistent with a crossing of Cassini through the cone region. The detection of heavy ions in both events of the split signature supports this further.
- For T75, a double-detection of the same tail filament is a possible explanation, due to rotations of the tail by the large fluctuations in the ambient magnetic field. Likewise, it is possible that those fluctuations simply rotated two separate filaments into the spacecraft trajectory.

In the second part, we were the first to model the plasma environment of Titan during Cassini's T96 flyby. The T96 encounter marks the only observed event of the entire Cassini mission where Titan was located in the supersonic solar wind in front of Saturn's bow shock. We investigated the possible contribution of fossilized fields to the observed magnetic field perturbations and studied the robustness of Titan's induced magnetosphere against the observed non-stationarities in the incident solar wind conditions. Our results were compared against the magnetic field and electron density measurements of this flyby. Our major results for this part are:

- The large scale features of Titan's induced magnetosphere during T96 are consistent with the interaction of Titan with a steady-state, high pressure ( $P_{sw} = 1.5$  nPa) solar wind that contains a mainly north-south oriented magnetic field. The modeled electron density for this run are in excellent quantitative agreement with Cassini observations.

- Simulations with a lower solar wind dynamic pressure that is comparable to that inferred from plasma observations (0.24 nPa, 0.64 nPa) fail to reproduce qualitatively both magnetic field and electron measurements.
- The modeled magnetic field results are also in quantitative agreement with key features of the observational data. A symmetric region around closest approach shows a large perturbation in the observed  $B_y$  component that is not in agreement with the induced draping pattern of a mainly north-south oriented upstream magnetic field.
- The modeled north-south oriented magnetic field induces a plateau-like structure in the  $B_y$  component, whereas the observations show a dip in  $B_y$  that goes to negative values, with the minimum location coinciding with closest approach. The magnitude of the induced  $B_y$  plateau from the simulations is comparable to the maximum observed  $B_y$  value.
- The upstream magnetic field experienced a change in orientation by about  $90^\circ$  approximately 40 min before the closest approach. Prior to that time the solar wind magnetic field had a mainly west-east orientation which then changed to a mainly north-south orientation.
- A simulation that uses the previously encountered west-east oriented upstream magnetic field as input parameter is able to qualitatively reproduce the negative minimum in the observed  $B_y$  component, while the other magnetic components do not show a significant perturbation.
- We conclude that fossilized magnetic field lines from the previously encountered west-east oriented magnetic field regime are responsible for the magnetic field perturbation around closest approach. The lifetime of these fossilized fields is on the order of 40 min, which is well within the accepted theoretical limit of up to 3 hours.

## 6.1 Outlook

Since the remaining Titan flybys of Cassini will all take place when Titan is located in Saturn's downstream magnetotail, it is unlikely to revisit Titan in the solar wind or Saturn's magnetosheath again, which are the only regions where fossilized magnetic fields have been observed at Titan. Also Cassini's main plasma spectrometer has ceased to operate in 2012, so that split-signature detections in its magnetotail are harder to observe. However, our results are not limited to the plasma interaction of Titan, but instead bear implications for other non-magnetized bodies in the solar system. The plasma interactions of Venus, Mars and active comets are very similar to that of Titan. It is therefore possible that split signatures in the tail region may also be detected by other or future spacecraft missions that visit these bodies. In particular Callisto, one of Jupiter's Galilean moons, is similar to Titan, as it also possesses an atmosphere and its plasma interaction is comparable to that of Titan with the relevant ion scales being comparable to the size of Callisto. In fact, a split tail similar to that of Titan has already been reported for Callisto (Liuzzo et al. 2015). Also, initial observations of the MAVEN spacecraft report of localized ion loss detections from Mars' atmosphere downstream of the planet (Halekas et al. 2016). The

objects that are embedded in the solar wind also seem to be more susceptible to the formation of fossilized magnetic fields, since the solar wind is able to change its direction on much shorter time-scales as the relative homogeneous flow inside one of the main planet's magnetospheres.

# Bibliography

- Ågren, K., Wahlund, J.-E., Garnier, P., Modolo, R., Cui, J., Galand, M., Müller-Wodarg, I., 2009, On the ionospheric structure of Titan, *Planet. Space Sci.*, 57, 1821–1827
- Achilleos, N., Arridge, C. S., Bertucci, C., Guio, P., Romanelli, N., Sergis, N., 2014, A combined model of pressure variations in Titan's plasma environment, *Geophys. Res. Lett.*, 41, 8730–8735
- Acuna, M. H., Connerney, J. E. P., Wasilewski, P., Lin, R. P., Anderson, K. A., Carlson, C. W., McFadden, J., Curtis, D. W., Mitchell, D., Reme, H., Mazelle, C., Sauvaud, J. A., D'Uston, C., Cros, A., Medale, J. L., Bauer, S. J., Cloutier, P., Mayhew, M., Winterhalter, D., Ness, N. F., 1998, Magnetic Field and Plasma Observations at Mars: Initial Results of, *Science*, 279, 1676
- Andrews, D., Cowley, S., Dougherty, M., Provan, G., 2010, Magnetic field oscillations near the planetary period in Saturn's equatorial magnetosphere: Variation of amplitude and phase with radial distance and local time, *J. Geophys. Res.*, 115, A04 212
- Andrews, D. J., Cowley, S. W. H., Dougherty, M. K., Lamy, L., Provan, G., Southwood, D. J., 2012, Planetary period oscillations in Saturn's magnetosphere: Evolution of magnetic oscillation properties from southern summer to post-equinox, *J. Geophys. Res.*, 117, A04224
- Arridge, C. S., Russell, C. T., Khurana, K. K., Achilleos, N., André, N., Rymer, A. M., Dougherty, M. K., Coates, A. J., 2007, Mass of Saturn's magnetodisc: Cassini observations, *Geophys. Res. Lett.*, 34, L09 108
- Arridge, C. S., André, N., Achilleos, N., Khurana, K. K., Bertucci, C. L., Gilbert, L. K., Lewis, G. R., Coates, A. J., Dougherty, M. K., 2008, Thermal electron periodicities at 20rs in saturn's magnetosphere, *Geophys. Res. Lett.*, 35, ISSN 1944-8007
- Arridge, C. S., Khurana, K. K., Russell, C. T., Southwood, D. J., Achilleos, N., Dougherty, M. K., Coates, A. J., Leinweber, H. K., 2008a, Warping of Saturn's magnetospheric and magnetotail current sheets, *J. Geophys. Res.*, 113, A08 217
- Arridge, C. S., Russell, C. T., Khurana, K. K., Achilleos, N., Cowley, S. W. H., Dougherty, M. K., Southwood, D. J., Bunce, E. J., 2008b, Saturn's magnetodisc current sheet, *J. Geophys. Res.*, 113, A04 214
- Arridge, C. S., Achilleos, N., Guio, P., 2011, Electric field variability and classifications of titan's magnetoplasma environment, *Annales Geophysicae*, 29, 1253–1258

- Arridge, C. S., André, N., Bertucci, C. L., Garnier, P., Jackman, C. M., Németh, Z., Rymer, A. M., Sergis, N., Szego, K., Coates, A. J., Crary, F. J., 2011a, Upstream of Saturn and Titan, *Space Science Rev.*, 162, 25–83
- Arridge, C. S., André, N., Khurana, K. K., Russell, C. T., Cowley, S. W. H., Provan, G., Andrews, D. J., Jackman, C. M., Coates, A. J., Sittler, E. C., Dougherty, M. K., Young, D. T., 2011b, Periodic motion of Saturn's nightside plasma sheet, *Journal of Geophysical Research (Space Physics)*, 116, A11 205
- Arridge, C. S., André, N., McAndrews, H. J., Bunce, E. J., Burger, M. H., Hansen, K. C., Hsu, H.-W., Johnson, R. E., Jones, G. H., Kempf, S., Khurana, K. K., Krupp, N., Kurth, W. S., Leisner, J. S., Paranicas, C., Roussos, E., Russell, C. T., Schippers, P., Sittler, E. C., Smith, H. T., Thomsen, M. F., Dougherty, M. K., 2011c, Mapping Magnetospheric Equatorial Regions at Saturn from Cassini Prime Mission Observations, *Space Science Rev.*, 164, 1–83
- Backes, H., Neubauer, F. M., Dougherty, M. K., Achilleos, N., André, N., Arridge, C. S., Bertucci, C., Jones, G. H., Khurana, K. K., Russell, C. T., Wennmacher, A., 2005, Titan's Magnetic Field Signature During the First Cassini Encounter, *Science*, 308, 992–995
- Bagdonat, T., 2005, Hybrid Simulation of Weak Comets, Ph.D. thesis, Technische Universität Braunschweig
- Béghin, C., Canu, P., Karkoschka, E., Sotin, C., Bertucci, C., Kurth, W. S., Berthelier, J. J., Grard, R., Hamelin, M., Schwingenschuh, K., Simões, F., 2009, New insights on Titan's plasma-driven Schumann resonance inferred from Huygens and Cassini data, *Planet. Space Sci.*, 57, 1872–1888
- Bertucci, C., 2009, Characteristics and variability of Titan's magnetic environment, *Royal Society of London Philosophical Transactions Series A*, 367, 789–798
- Bertucci, C., Mazelle, C., Slavin, J. A., Russell, C. T., Acuña, M. H., 2003, Magnetic field draping enhancement at Venus: Evidence for a magnetic pileup boundary, *Geophys. Res. Lett.*, 30, SSC 1 (1–4), CiteID: 1876, doi: 10.1029/2003GL017 271
- Bertucci, C., Neubauer, F. M., Szego, K., Wahlund, J.-E., Coates, A. J., Dougherty, M. K., Young, D. T., Kurth, W. S., 2007, Structure of Titan's mid-range magnetic tail: Cassini magnetometer observations during the T9 flyby, *Geophys. Res. Lett.*, 34, L24S02
- Bertucci, C., Achilleos, N., Dougherty, M. K., Modolo, R., Coates, A. J., Szego, K., Masters, A., Ma, Y., Neubauer, F. M., Garnier, P., Wahlund, J.-E., Young, D. T., 2008, The Magnetic Memory of Titan's Ionized Atmosphere, *Science*, 321, 1475–1478, doi: 10.1126/science.1159 780
- Bertucci, C., Sinclair, B., Achilleos, N., Hunt, P., Dougherty, M. K., Arridge, C. S., 2009, The variability of Titan's magnetic environment, *Planet. Space Sci.*, 57, 1813–1820

- Bertucci, C., Duru, F., Edberg, N., Fraenz, M., Martinecz, C., Szego, K., Vaisberg, O., 2011, The Induced Magnetospheres of Mars, Venus, and Titan, *Space Science Rev.*, 162, 113–171
- Bertucci, C., Hamilton, D. C., Kurth, W. S., Hospodarsky, G., Mitchell, D., Sergis, N., Edberg, N. J. T., Dougherty, M. K., 2015, Titan's interaction with the supersonic solar wind, *Geophys. Res. Lett.*, 42, 193–200
- Boesswetter, A., Auster, U., Richter, I., Fränz, M., Langlais, B., McKenna-Lawlor, S., Simon, S., Motschmann, U., Glassmeier, K. H., Edberg, N. J. T., Lundin, R., 2009, Rosetta swing-by at Mars - an analysis of the ROMAP measurements in comparison with results of 3-D multi-ion hybrid simulations and MEX/ASPERA-3 data, *Ann. Geophys.*, 27, 2383–2398
- Boesswetter, A., Lammer, H., Kulikov, Y., Motschmann, U., Simon, S., 2010, Non-thermal water loss of the early Mars: 3D multi-ion hybrid simulations, *Planet. Space Sci.*, 58, 2031–2043
- Böswetter, A., Bagdonat, T., Motschmann, U., Sauer, K., 2004, Plasma boundaries at Mars: a 3-D simulation study, *Annales Geophysicae*, 22, 4363–4379
- Böswetter, A., Simon, S., Bagdonat, T., Motschmann, U., Fränz, M., Roussos, E., Krupp, N., Woch, J., Schüle, J., Barabash, S., Lundin, R., 2007, Comparison of plasma data from ASPERA-3/Mars-Express with a 3D hybrid simulation, *Annales Geophysicae*, 25, 1851–1864
- Brecht, S. H., Luhmann, J. G., Larson, D. J., 2000, Simulation of the Saturnian magnetospheric interaction with Titan, *J. Geophys. Res.*, 105, 13,119–13,130
- Broadfoot, A. L., Sandel, B. R., Shemansky, D. E., Holberg, J. B., Smith, G. R., Strobel, D. F., McConnell, J. C., Kumar, S., Hunten, D. M., Atreya, S. K., Donahue, T. M., Moos, H. W., Bertaux, J. L., Blamont, J. E., Pomphrey, R. B., Linick, S., 1981, Extreme ultraviolet observations from Voyager 1 encounter with Saturn, *Science*, 212, 206–211
- Burton, M. E., Dougherty, M. K., Russell, C. T., 2010, Saturn's internal planetary magnetic field, *Geophys. Res. Lett.*, 37, L24 105
- Coates, A. J., Crary, F. J., Lewis, G. R., Young, D. T., Waite, J. H., Sittler, E. C., 2007a, Discovery of heavy negative ions in Titan's ionosphere, *Geophys. Res. Lett.*, 34, L22103
- Coates, A. J., Crary, F. J., Young, D. T., Szego, K., Arridge, C. S., Bebesi, Z., Sittler, E. C., Hartle, R. E., Hill, T. W., 2007b, Ionospheric electrons in Titan's tail: Plasma structure during the Cassini T9 encounter, *Geophys. Res. Lett.*, 34, L24S05
- Coates, A. J., Wellbrock, A., Lewis, G. R., Jones, G. H., Young, D. T., Crary, F. J., Waite, J. H., 2009, Heavy negative ions in Titan's ionosphere: Altitude and latitude dependence, *Planet. Space Sci.*, 57, 1866–1871

- Coates, A. J., Wahlund, J.-E., Ågren, K., Edberg, N., Cui, J., Wellbrock, A., Szego, K., 2011, Recent Results from Titan's Ionosphere, *Space Science Rev.*, 162, 85–111
- Coates, A. J., Wellbrock, A., Lewis, G. R., Arridge, C. S., Crary, F. J., Young, D. T., Thomsen, M. F., Reisenfeld, D. B., Sittler, Jr., E. C., Johnson, R. E., Szego, K., Bebesi, Z., Jones, G. H., 2012, Cassini in Titan's tail: CAPS observations of plasma escape, *Journal of Geophysical Research (Space Physics)*, 117, A05 324
- Cravens, T. E., Robertson, I. P., Waite, J. H., Yelle, R. V., Kasprzak, W. T., Keller, C. N., Ledvina, S. A., Niemann, H. B., Luhmann, J. G., McNutt, R. L., Ip, W.-H., De La Haye, V., Mueller-Wodarg, I., Wahlund, J.-E., Anicich, V. G., Vuitton, V., 2006, Composition of Titan's ionosphere, *Geophys. Res. Lett.*, 33, L07 105, 1–4 (doi:10.1029/2005GL025 575)
- Cravens, T. E., Robertson, I. P., Ledvina, S. A., Mitchell, D., Krimigis, S. M., Waite, J. H., 2008, Energetic ion precipitation at Titan, *Geophys. Res. Lett.*, 35, L03103
- Cravens, T. E., Richard, M., Ma, Y.-J., Bertucci, C., Luhmann, J. G., Ledvina, S., Robertson, I. P., Wahlund, J.-E., Ågren, K., Cui, J., Muller-Wodarg, I., Waite, J. H., Dougherty, M., Bell, J., Ulusen, D., 2010, Dynamical and magnetic field time constants for Titan's ionosphere: Empirical estimates and comparisons with Venus, *Journal of Geophysical Research (Space Physics)*, 115, A08 319
- Cui, J., Yelle, R., Vuitton, V., Jr., J. W., Kasprzak, W., Gell, D., Niemann, H., Müller-Wodarg, I., Borggren, N., Fletcher, G., Patrick, E., Raaen, E., Magee, B., 2009, Analysis of Titan's neutral upper atmosphere from Cassini ion neutral mass spectrometer measurements, *Icarus*, 200, 581 – 615, ISSN 0019-1035
- De La Haye, V., Waite, J. H., Cravens, T. E., Robertson, I. P., Lebonnois, S., 2008, Coupled ion and neutral rotating model of Titan's upper atmosphere, *Icarus*, 197, 110–136
- Dougherty, M. K., Kellock, S., Southwood, D. J., Balogh, A., Smith, E. J., Tsurutani, B. T., Gerlach, B., Glassmeier, K.-H., Gleim, F., Russell, C. T., Erdos, G., Neubauer, F. M., Cowley, S. W. H., 2004, The Cassini Magnetic Field Investigation, *Space Science Reviews*, 114, 331–383
- Dubinin, E., Fränz, M., Woch, J., Roussos, E., Barabash, S., Lundin, R., Winningham, J. D., Frahm, R. A., Acuña, M., 2006, Plasma Morphology at Mars. Aspera-3 Observations, *Space Science Rev.*, 126, 209–238
- Edberg, N. J. T., Wahlund, J.-E., Ågren, K., Morooka, M. W., Modolo, R., Bertucci, C., Dougherty, M. K., 2010, Electron density and temperature measurements in the cold plasma environment of Titan: Implications for atmospheric escape, *Geophys. Res. Lett.*, 37, L20105
- Edberg, N. J. T., Andrews, D. J., Shebanits, O., Ågren, K., Wahlund, J.-E., Opgenoorth, H. J., Roussos, E., Garnier, P., Cravens, T. E., Badman, S. V., Modolo, R., Bertucci, C., Dougherty, M. K., 2013, Extreme densities in Titan's ionosphere during the T85 magnetosheath encounter, *Geophys. Res. Lett.*, 40, 2879–2883

- Garnier, P., Dandouras, I., Toubanc, D., Roelof, E. C., Brandt, P. C., Mitchell, D. G., Krimigis, S. M., Krupp, N., Hamilton, D. C., Wahlund, J.-E., 2010, Statistical analysis of the energetic ion and ENA data for the Titan environment, *Planet. Space Sci.*, 58, 1811–1822
- Gurnett, D. A., Kurth, W. S., Kirchner, D. L., Hospodarsky, G. B., Averkamp, T. F., Zarka, P., Lecacheux, A., Manning, R., Roux, A., Canu, P., Cornilleau-Wehrlin, N., Galopeau, P., Meyer, A., Boström, R., Gustafsson, G., Wahlund, J.-E., Åhlen, L., Rucker, H. O., Ladreiter, H. P., Macher, W., Woolliscroft, L. J. C., Alleyne, H., Kaiser, M. L., Desch, M. D., Farrell, W. M., Harvey, C. C., Louarn, P., Kellogg, P. J., Goetz, K., Pedersen, A., 2004, The Cassini Radio and Plasma Wave Investigation, *Space Science Rev.*, 114, 395–463
- Halekas, J. S., Brain, D. A., Ruhunusiri, S., McFadden, J. P., Mitchell, D. L., Mazelle, C., Connerney, J. E. P., Harada, Y., Hara, T., Espley, J. R., DiBraccio, G. A., Jakosky, B. M., 2016, Plasma clouds and snowplows: Bulk plasma escape from Mars observed by MAVEN, *Geophys. Res. Lett.*, 43, 1426–1434
- Hansen, C. J., Esposito, L., Stewart, A. I. F., Colwell, J., Hendrix, A., Pryor, W., Shemansky, D., West, R., 2006, Enceladus' Water Vapor Plume, *Science*, 311, 1422–1425
- Hill, T. W., 1979, Inertial limit on corotation, *J. Geophys. Res.*, 84, 6554–6558
- Kallio, E., Sillanpää, I., Janhunen, P., 2004, Titan in subsonic and supersonic flow, *Geophys. Res. Lett.*, 31, L15 703
- Kallio, E., Sillanpää, I., Jarvinen, R., Janhunen, P., Dougherty, M., Bertucci, C., Neubauer, F., 2007, Morphology of the magnetic field near Titan: Hybrid model study of the Cassini T9 flyby, *Geophys. Res. Lett.*, 34, L24S09
- Khurana, K. K., Mitchell, D. G., Arridge, C. S., Dougherty, M. K., Russell, C. T., Paranicas, C., Krupp, N., Coates, A. J., 2009, Sources of rotational signals in Saturn's magnetosphere, *J. Geophys. Res.*, 114, A02 211
- Kliore, A. J., Nagy, A. F., Marouf, E. A., French, R. G., Flasar, F. M., Rappaport, N. J., Anabtawi, A., Asmar, S. W., Kahann, D. S., Barbinis, E., Goltz, G. L., Fleischman, D. U., Rochblatt, D. J., 2008, First results from the Cassini radio occultations of the Titan ionosphere, *J. Geophys. Res.*, 113, A09317
- Knudsen, W. C., Miller, K. L., Spenser, K., 1982, Improved Venus ionopause altitude calculation and comparison with measurement, *J. Geophys. Res.*, 87, 2246–2254
- Krasnopolsky, V. A., 2009, A photochemical model of titan's atmosphere and ionosphere, *Icarus*, 201, 226 – 256, ISSN 0019-1035
- Kriegel, H., 2014, The plasma environments of Saturn's moons Enceladus and Rhea : modeling of Cassini magnetic field data, Ph.D. thesis, Technische Universität Braunschweig

- Kriegel, H., Simon, S., Motschmann, U., Saur, J., Neubauer, F. M., Persoon, A. M., Dougherty, M. K., Gurnett, D. A., 2011, Influence of negatively charged plume grains on the structure of Enceladus' Alfvén wings: hybrid simulations versus Cassini MAG data, *J. Geophys. Res.*, 116(A10), A10 223
- Kriegel, H., Simon, S., Meier, P., Motschmann, U., Saur, J., Wennmacher, A., Strobel, D. F., Dougherty, M. K., 2014, Ion densities and magnetic signatures of dust pick-up at Enceladus, *Journal of Geophysical Research (Space Physics)*, 119, 2740–2774
- Krimigis, S. M., Mitchell, D. G., Hamilton, D. C., Livi, S., Dandouras, J., Jaskulek, S., Armstrong, T. P., Boldt, J. D., Cheng, A. F., Gloeckler, G., Hayes, J. R., Hsieh, K. C., Ip, W.-H., Keath, E. P., Kirsch, E., Krupp, N., Lanzerotti, L. J., Lundgren, R., Mauk, B. H., McEntire, R. W., Roelof, E. C., Schlemm, C. E., Tossman, B. E., Wilken, B., Williams, D. J., 2004, Magnetosphere Imaging Instrument (MIMI) on the Cassini Mission to Saturn/Titan, *Space Science Rev.*, 114, 233–329
- Krupp, N., Roussos, E., Kriegel, H., Kollmann, P., Kivelson, M. G., Kotova, A., Paranicas, C., Mitchell, D. G., Krimigis, S. M., Khurana, K. K., 2013, Energetic particle measurements in the vicinity of Dione during the three Cassini encounters 2005-2011, *Icarus*, 226, 617–628
- Kurth, W. S., Averkamp, T. F., Gurnett, D. A., Groene, J. B., Lecacheux, A., 2008, An update to a Saturnian longitude system based on kilometric radio emissions, *J. Geophys. Res.*, 113, A05 222
- Ledvina, S. A., Brecht, S. H., 2012, Consequences of negative ions for Titan's plasma interaction, *Geophys. Res. Lett.*, 39, L20103
- Ledvina, S. A., Brecht, S. H., Cravens, T. E., 2012, The orientation of titan's dayside ionosphere and its effects on titan's plasma interaction, *Earth, Planets and Space*, 64, 207–230, ISSN 1343-8832
- Lipatov, A., Jr., E. S., Hartle, R., Cooper, J., Simpson, D., 2012, Saturn's magnetosphere interaction with titan for t9 encounter: 3d hybrid modeling and comparison with caps observations, *Planet. Space Sci.*, 61, 66 – 78, ISSN 0032-0633
- Lipatov, A. S., Sittler, E. C., Hartle, R. E., Cooper, J. F., Simpson, D. G., 2014, Titan's plasma environment: 3D hybrid kinetic modeling of the TA flyby and comparison with CAPS-ELS and RPWS LP observations, *Planet. Space Sci.*, 93, 119–128
- Liuzzo, L., Feyerabend, M., Simon, S., Motschmann, U., 2015, The impact of Callisto's atmosphere on its plasma interaction with the Jovian magnetosphere, *J. Geophys. Res.*, 120, 9401–9427
- López-Moreno, J. J., Molina-Cuberos, G. J., Hamelin, M., Grard, R., Simões, F., Godard, R., Schwingenschuh, K., Béghin, C., Berthelier, J. J., Brown, V. J. G., Falkner, P., Ferri, F., Fulchignoni, M., Jernej, I., Jerónimo, J. M., Rodrigo, R., Trautner, R., 2008, Structure of Titan's low altitude ionized layer from the Relaxation Probe onboard HUYGENS, *Geophys. Res. Lett.*, 35, L22104

- Luhmann, J. G., 1996, Titan's ion exosphere wake: A natural ion mass spectrometer?, *J. Geophys. Res.*, 101, 29,387–29,393
- Ma, Y.-J., Nagy, A. F., Cravens, T. E., Sokolov, I. V., Clark, J., Hansen, K. C., 2004, 3-D global MHD prediction for the first close flyby of Titan by Cassini, *Geophys. Res. Lett.*, 31, 1–4
- Ma, Y.-J., Nagy, A. F., Cravens, T. E., Sokolov, I. V., Hansen, K. C., Wahlund, J.-E., Crary, F. J., Coates, A. J., Dougherty, M. K., 2006, Comparisons between MHD model calculations and observations of Cassini flybys of Titan, *J. Geophys. Res.*, 111, A05 207
- Ma, Y.-J., Nagy, A. F., Toth, G., Cravens, T. E., Russell, C. T., Gombosi, T. I., Wahlund, J.-E., Crary, F. J., Coates, A. J., Bertucci, C. L., Neubauer, F. M., 2007, 3D global multi-species Hall-MHD simulation of the Cassini T9 flyby, *Geophys. Res. Lett.*, 34, L24S10
- Ma, Y.-J., Nagy, A. F., Toth, G., Cravens, T. E., Russell, C. T., Gombosi, T. I., Wahlund, J.-E., Crary, F. J., Coates, A. J., Bertucci, C. L., Neubauer, F. M., 2007, 3D global multi-species Hall-MHD simulation of the Cassini T9 flyby, *Geophys. Res. Lett.*, 34, L24S10
- Ma, Y.-J., Russell, C. T., Nagy, A. F., Toth, G., Bertucci, C., Dougherty, M. K., Neubauer, F. M., Wellbrock, A., Coates, A. J., Garnier, P., Wahlund, J.-E., Cravens, T. E., Crary, F. J., 2009, Time-dependent global MHD simulations of Cassini T32 flyby: From magnetosphere to magnetosheath, *J. Geophys. Res.*, 114, A03 204
- Ma, Y. J., Russell, C. T., Nagy, A. F., Toth, G., Dougherty, M. K., Wellbrock, A., Coates, A. J., Garnier, P., Wahlund, J.-E., Cravens, T. E., Richard, M. S., Crary, F. J., 2011, The importance of thermal electron heating in Titan's ionosphere: Comparison with Cassini T34 flyby, *J. Geophys. Res.*, 116, A10213
- Masters, A., Schwartz, S. J., Henley, E. M., Thomsen, M. F., Zieger, B., Coates, A. J., Achilleos, N., Mitchell, J., Hansen, K. C., Dougherty, M. K., 2011, Electron heating at Saturn's bow shock, *Journal of Geophysical Research (Space Physics)*, 116, A10107
- Matthews, A. P., 1994, Current Advance Method and Cyclic Leapfrog for 2D Multispecies Hybrid Plasma Simulations, *J. of Computational Physics*, 112, 102–116
- Modolo, R., Chanteur, G. M., 2008, A global hybrid model for Titan's interaction with the Kronian plasma: Application to the Cassini Ta flyby, *Journal of Geophysical Research (Space Physics)*, 113, A01 317
- Modolo, R., Chanteur, G. M., Wahlund, J.-E., Canu, P., Kurth, W. S., Gurnett, D., Matthews, A. P., Bertucci, C., 2007a, Plasma environment in the wake of Titan from hybrid simulation: A case study, *Geophys. Res. Lett.*, 34, doi:10.1029/2007GL030489
- Modolo, R., Wahlund, J.-E., Boström, R., Canu, P., Kurth, W. S., Gurnett, D., Lewis, G. R., Coates, A. J., 2007b, Far plasma wake of Titan from the RPWS observations: A case study, *Geophys. Res. Lett.*, 34, L24S04, doi:10.1029/2007GL030482

- Müller, J., Simon, S., Motschmann, U., Glassmeier, K. H., Saur, J., Schuele, J., Pringle, G. J., 2010, Magnetic field fossilization and tail reconfiguration in Titan's plasma environment during a magnetopause passage: 3D adaptive hybrid code simulations, *Planet. Space Sci.*, 58, 1526–1546, doi: 10.1016/j.pss.2010.07.018
- Müller, J., Simon, S., Motschmann, U., Schüle, J., Glassmeier, K., Pringle, G. J., 2011, A.I.K.E.F.: Adaptive hybrid model for space plasma simulations, *Computer Physics Communications*, 182, 946–966, doi: 10.1016/j.cpc.2010.12.033
- Müller, J., Simon, S., Wang, Y.-C., Motschmann, U., Heyner, D., Schüle, J., Ip, W.-H., Kleindienst, G., Pringle, G. J., 2012, Origin of Mercury's double magnetopause: 3D hybrid simulation study with A.I.K.E.F., *Icarus*, 218, 666–687
- Németh, Z., Szego, K., Bebesi, Z., Erdős, G., Foldy, L., Rymer, A., Sittler, E. C., Coates, A. J., Wellbrock, A., 2011, Ion distributions of different Kronian plasma regions, *Journal of Geophysical Research (Space Physics)*, 116, A09212
- Neubauer, F. M., Gurnett, D. A., Scudder, J. D., Hartle, R. E., 1984, Titan's magnetospheric interaction, in *Saturn*, (Eds.) T. Gehrels, M. S. Matthews, pp. 760–787, University of Arizona Press, Tucson, Arizona
- Neubauer, F. M., Backes, H., Dougherty, M. K., Wennmacher, A., Russell, C. T., Coates, A., Young, D., Achilleos, N., Andre, N., Arridge, C. S., Bertucci, C., Jones, G. H., Khurana, K. K., Knetter, T., Law, A., Lewis, G. R., Saur, J., 2006, Titan's near magnetotail from magnetic field and plasma observations and modelling: Cassini flybys TA, TB and T3, *J. Geophys. Res.*, 111, A10220
- Niemann, H. B., Atreya, S. K., Demick, J. E., Gautier, D., Haberman, J. A., Harpold, D. N., Kasprzak, W. T., Lunine, J. I., Owen, T. C., Raulin, F., 2010, Composition of titan's lower atmosphere and simple surface volatiles as measured by the cassini-huygens probe gas chromatograph mass spectrometer experiment, *J. Geophys. Res.*, 115, ISSN 2156-2202
- Regoli, L., Roussos, E., Feyerabend, M., Jones, G., Krupp, N., Coates, A., Simon, S., Motschmann, U., Dougherty, M., 2015, Access of energetic particles to titan's exobase: A study of cassini's t9 flyby, *Planet. Space Sci.*, pp. –, ISSN 0032-0633
- Richards, P. G., Fennelly, J. A., Torr, D. G., 1994, EUVAC: A solar EUV flux model for aeronomic calculations, *J. Geophys. Res.*, 99, 8981–8992
- Rosenqvist, L., Wahlund, J.-E., Ågren, K., Modolo, R., Opgenoorth, H. J., Strobel, D., Müller-Wodarg, I., Garnier, P., Bertucci, C., 2009, Titan ionospheric conductivities from Cassini measurements, *Planet. Space Sci.*, 57, 1828–1833
- Roussos, E., Mueller, J., Simon, S., Boesswetter, A., Motschmann, U., Krupp, N., Fraenz, M., Woch, J., Khurana, K. K., Dougherty, M. K., 2008, Plasma and fields in the wake of Rhea: 3-D hybrid simulation and comparison with Cassini data, *Annales Geophysicae*, 26, 619–637

- Russell, C. T., Elphic, R. C., Slavin, J. A., 1979, Initial Pioneer Venus magnetic field results - Nightside observations, *Science*, 205, 114–116
- Rymer, A. M., Smith, H. T., Wellbrock, A., Coates, A. J., Young, D. T., 2009, Discrete classification and electron energy spectra of Titan's varied magnetospheric environment, *Geophys. Res. Lett.*, 36, L15 109, doi: 10.1029/2009GL039 427
- Schunk, R., Nagy, A., 2009, *Ionospheres*, Cambridge University Press, second edn., ISBN 9780511635342
- Sillanpää, I., Kallio, E., Jarvinen, R., Janhunen, P., 2007, Oxygen ions at Titan's exobase in a Voyager 1-type interaction from a hybrid simulation, *J. Geophys. Res.*, 112, A12205
- Simon, S., 2007, Titan's highly variable plasma environment: A 3D hybrid simulation study, Ph.D. thesis, Technische Universität Braunschweig
- Simon, S., 2009, Real-time 3D hybrid simulation of Titan's plasma interaction during a solar wind excursion, *Annales Geophysicae*, 27, 3349–3365
- Simon, S., Motschmann, U., 2009, Titan's induced magnetosphere under non-ideal upstream conditions: 3D multi-species hybrid simulations, *Planet. Space Sci.*, 57, 2001–2015, doi: 10.1016/j.pss.2009.08.010
- Simon, S., Bagdonat, T., Motschmann, U., Glassmeier, K.-H., 2006a, Plasma environment of magnetized asteroids: A 3D hybrid simulation study, *Annales Geophysicae*, 24, 407–414
- Simon, S., Boesswetter, A., Bagdonat, T., Motschmann, U., Glassmeier, K.-H., 2006b, Plasma environment of Titan: a 3-d hybrid simulation study, *Ann. Geophys.*, 24, 1113–1135
- Simon, S., Boesswetter, A., Bagdonat, T., Motschmann, U., 2007a, Physics of the Ion Composition Boundary: A comparative 3D hybrid simulation study of Mars and Titan, *Ann. Geophys.*, 25, 99–115
- Simon, S., Boesswetter, A., Bagdonat, T., Motschmann, U., Schuele, J., 2007b, Three-dimensional multispecies hybrid simulation of Titan's highly variable plasma environment, *Ann. Geophys.*, 25, 117–144
- Simon, S., Kleindienst, G., Boesswetter, A., Bagdonat, T., Motschmann, U., Glassmeier, K.-H., Schuele, J., Bertucci, C., Dougherty, M. K., 2007c, Hybrid simulation of Titan's magnetic field signature during the Cassini T9 flyby, *Geophys. Res. Lett.*, 34
- Simon, S., Motschmann, U., Glassmeier, K.-H., 2008a, Influence of non-stationary electromagnetic field conditions on ion pick-up at Titan: 3-D multispecies hybrid simulations, *Ann. Geophys.*, 26, 599–617
- Simon, S., Motschmann, U., Kleindienst, G., Glassmeier, K.-H., Bertucci, C., Dougherty, M. K., 2008b, Titan's magnetic field signature during the Cassini T34 flyby: Comparison between hybrid simulations and MAG data, *Geophys. Res. Lett.*, 35, L04107

- Simon, S., Motschmann, U., Kleindienst, G., Saur, J., Bertucci, C., Dougherty, M., Aridge, C., Coates, A., 2009a, Titan's plasma environment during a magnetosheath excursion: Real-time scenarios for Cassini's T32 flyby from a hybrid simulation, *Annales Geophysicae*, 27(2), 669–685
- Simon, S., Saur, J., Neubauer, F., Motschmann, U., Dougherty, M., 2009b, Plasma wake of Tethys: Hybrid simulations versus Cassini MAG data, *Geophys. Res. Lett.*, 36, L04 108
- Simon, S., Wennmacher, A., Neubauer, F., Bertucci, C., Kriegel, H., Saur, J., Russell, C., Dougherty, M., 2010, Titan's highly dynamic magnetic environment: A systematic survey of Cassini magnetometer observations from flybys TA–T62, *Planet. Space Sci.*, 58, 1230–1251, doi: 10.1016/j.pss.2010.04.021
- Simon, S., Kriegel, H., Saur, J., Wennmacher, A., Neubauer, F. M., Roussos, E., Motschmann, U., Dougherty, M. K., 2012, Analysis of Cassini magnetic field observations over the poles of Rhea, *Journal of Geophysical Research (Space Physics)*, 117, A07211
- Simon, S., Treeck, S. C., Wennmacher, A., Saur, J., Neubauer, F. M., Bertucci, C. L., Dougherty, M. K., 2013, Structure of Titan's induced magnetosphere under varying background magnetic field conditions: Survey of Cassini magnetometer data from flybys TA–T85, *Journal of Geophysical Research (Space Physics)*, 118, 1679–1699
- Simon, S., Neubauer, F. M., Wennmacher, A., Dougherty, M. K., 2014, Variability of titan's induced magnetotail: Cassini magnetometer observations, *Journal of Geophysical Research: Space Physics*, 119, 2024–2037, ISSN 2169-9402
- Simon, S., Roussos, E., Paty, C. S., 2015, The interaction between Saturn's moons and their plasma environments, *PHR*, 602, 1–65
- Sittler, E. C., Hartle, R. E., Johnson, R. E., Cooper, J. F., Lipatov, A. S., Bertucci, C., Coates, A. J., Szego, K., Shappirio, M., Simpson, D. G., Wahlund, J.-E., 2010, Saturn's magnetospheric interaction with Titan as defined by Cassini encounters T9 and T18: New results, *Planet. Space Sci.*, 58, 327–350
- Smith, H. T., Rymer, A. M., 2014, An empirical model for the plasma environment along titan's orbit based on cassini plasma observations, *J. Geophys. Res.*, 119, 5674–5684
- Snowden, D., 2010, Titan's Interaction with Saturn's Dynamic Magnetosphere: Three-Dimensional Multi-fluid Simulations, Ph.D. thesis, University of Washington
- Snowden, D., Winglee, R., 2013, Three-dimensional multi-fluid simulations of Titan's interaction with Saturn's magnetosphere: Comparisons with Cassini's T55 flyby, *J. Geophys. Res.*, 118, 4852–4863
- Snowden, D., Winglee, R., Bertucci, C., Dougherty, M., 2007, Three-dimensional multi-fluid simulation of the plasma interaction at Titan, *Journal of Geophysical Research (Space Physics)*, 112, A12 221

- Snowden, D., Winglee, R., Kidder, A., 2011a, Titan at the edge Part I: Titan's interaction with Saturn's magnetosphere in the pre-noon sector, *J. Geophys. Res.*, 116, A08 229
- Snowden, D., Winglee, R., Kidder, A., 2011b, Titan at the edge Part II: a global simulation of Titan exiting and re-entering Saturn's magnetosphere at 13.6 SLT, *J. Geophys. Res.*, 116, A08 230
- Snowden, D., Yelle, R. V., Galand, M., Coates, A. J., Wellbrock, A., Jones, G. H., Lavvas, P., 2013, Auroral electron precipitation and flux tube erosion in Titan's upper atmosphere, *Icarus*, 226, 186–204
- Southwood, D. J., Cowley, S. W. H., 2014, The origin of Saturn's magnetic periodicities: Northern and southern current systems, *J. Geophys. Res.*, 119, 1563–1571
- Sulaiman, A. H., Masters, A., Dougherty, M. K., Burgess, D., Fujimoto, M., Hospodarsky, G. B., 2015, Quasiperpendicular high mach number shocks, *Phys. Rev. Lett.*, 115, 125 001
- Szego, K., Bebesi, Z., Bertucci, C., Coates, A. J., Crary, F., Erdos, G., Hartle, R., Sittler, E. C., Young, D. T., 2007, Charged particle environment of Titan during the T9 flyby, *Geophys. Res. Lett.*, 34, L24S03
- Thomsen, M. F., Reisenfeld, D. B., Delapp, D. M., Tokar, R. L., Young, D. T., Crary, F. J., Sittler, E. C., McGraw, M. A., Williams, J. D., 2010, Survey of ion plasma parameters in Saturn's magnetosphere, *J. Geophys. Res.*, 115, A10220
- Trafton, L., 1972a, The Bulk Composition of Titan's Atmosphere, *Astrophys. J.*, 175, 295
- Trafton, L., 1972b, On the Possible Detection of H<sub>2</sub> in Titan's Atmosphere, *Astrophys. J.*, 175, 285
- Ulusen, D., Luhmann, J. G., Ma, Y. J., Mandt, K. E., Waite, J. H., Dougherty, M. K., Wahlund, J. E., Russell, C. T., Cravens, T. E., Edberg, N. J. T., Agren, K., 2012, Comparisons of Cassini flybys of the Titan magnetospheric interaction with an MHD model: Evidence for organized behavior at high altitudes, *Icarus*, 217, 43–54
- Vuitton, V., Yelle, R. V., McEwan, M. J., 2007, Ion chemistry and N-containing molecules in Titan's upper atmosphere, *Icarus*, 191, 722–742
- Waite, J. H., Young, D. T., Cravens, T. E., Coates, A. J., Crary, F. J., Magee, B., Westlake, J., 2007, The Process of Tholin Formation in Titan's Upper Atmosphere, *Science*, 316, 870
- Wei, H. Y., Russell, C. T., Wellbrock, A., Dougherty, M. K., Coates, A. J., 2009, Plasma environment at Titan's orbit with Titan present and absent, *Geophys. Res. Lett.*, 36, L23 202
- Wei, H. Y., Russell, C. T., Dougherty, M. K., Neubauer, F. M., Ma, Y. J., 2010, Upper limits on Titan's magnetic moment and implications for its interior, *Journal of Geophysical Research (Planets)*, 115, E10 007, doi: 10.1029/2009JE003 538

- Wei, H. Y., Russell, C. T., Dougherty, M. K., Ma, Y. J., Hansen, K. C., McAndrews, H. J., Wellbrock, A., Coates, A. J., Thomsen, M. F., Young, D. T., 2011, Unusually strong magnetic fields in Titan's ionosphere: T42 case study, *ASR*, 48, 314–322
- Wellbrock, A., Coates, A. J., Jones, G. H., Lewis, G. R., Waite, J. H., 2013, Cassini CAPS-ELS observations of negative ions in Titan's ionosphere: Trends of density with altitude, *Geophys. Res. Lett.*, 40, 4481–4485
- Westlake, J. H., Paranicas, C. P., Cravens, T. E., Luhmann, J. G., Mandt, K. E., Smith, H. T., Mitchell, D. G., Rymer, A. M., Perry, M. E., Waite, Jr., J. H., Wahlund, J.-E., 2012, The observed composition of ions outflowing from Titan, *Geophys. Res. Lett.*, 39, L19104
- Wilson, R. J., Tokar, R. L., Kurth, W. S., Persoon, A. M., 2010, Properties of the thermal ion plasma near Rhea as measured by the Cassini plasma spectrometer, *Journal of Geophysical Research (Space Physics)*, 115, A05 201

# Acknowledgements

Mein herzlichster Dank geht an Sven Simon für seine tolle Betreuung in den letzten 4 Jahren. Ich habe wirklich viel gelernt bei ihm und sein unerschütterlicherer Optimismus hat mir über viele Steine hinweggeholfen. Er war zu jeder Tag und Nachtzeit zu allen möglichen Problemen erreichbar. Ich denke ich kann behaupten, dass ohne ihn diese Arbeit nicht möglich gewesen wäre

Desweiteren möchte ich den Mitgliedern der Georgia Tech danken, bei denen ich wundervolle 9 Monate verbringen durfte und bei denen ich viele freundliche Gesichter und neue Freunde gefunden habe. An erster Stelle ist hier sicher Lucas Liuzzo zu nennen, der mir mit seiner frühmorgendlichen Kaffeeversorgung jedes Mal den Tag rettete und mir auch sonst ein guter Freund wurde.

Mein Dank für 4 schöne Jahre geht natürlich auch an die Kölner Gruppe, allen voran Joachim Saur, der jederzeit bereit war für wissenschaftliche Diskussionen und der begleitend die Betreuung meiner Arbeit durchführte. Für die ertragreichen Diskussionen zum T96 Paper danke ich ausserdem Fritz Neubauer, der immer wieder bewiesen hat welch erstaunlicher Quell an Wissen in ihm schlummert. Weiterhin danke ich meinen Freunden und Kollegen, Oliver, Aljona, Fabrizio, Anne, Mitch, Slawa. Ohne euch hätte es alles keinen Spass gemacht und ich werde euch definitiv vermissen. Schönen Dank auch für nichts an meine besten Freunde Niclas, Enno, Fruhni und Jessi :D. Unsere Wege haben sich zwar getrennt nach Jena, aber ihr wart immer im Geiste dabei. Schlussendlich gebührt Olf der letzte Dank, denn ohne ihn wäre ich überhaupt nicht in die Situation gekommen promovieren zu können. :)



# Erklärung

Ich versichere, dass ich die von mir vorgelegte Dissertation selbständig angefertigt, die benutzten Quellen und Hilfsmittel vollständig angegeben und die Stellen der Arbeit - einschliesslich Tabellen, Karten und Abbildungen -, die anderen Werken im Wortlaut oder dem Sinn nach entnommen sind, in jedem Einzelfall als Entlehnung kenntlich gemacht habe; dass diese Dissertation noch keiner anderen Fakultät oder Universität zur Prüfung vorgelegen hat; dass sie - abgesehen von unten angegebenen Teilpublikationen - noch nicht veröffentlicht worden ist sowie, dass ich eine solche Veröffentlichung vor Abschluss des Promotionsverfahrens nicht vornehmen werde. Die Bestimmungen der Promotionsordnung sind mir bekannt. Die von mir vorgelegte Dissertation ist von Dr. habil. Sven Simon betreut worden.

Teilpublikationen:

**Feyerabend, M.**, Simon, S., Motschmann, U., Liuzzo, L., 2015, Filamented ion tail structures at titan: A hybrid simulation study, *Planetary and Space Science*, 117, 362-376, ISSN 0032-0633, <http://dx.doi.org/10.1016/j.pss.2015.07.008>

**Feyerabend, M.**, S. Simon, F. M. Neubauer, U. Motschmann, C. Bertucci, N. J. T. Edberg, G. B. Hospodarsky, and W. S. Kurth (2016), Hybrid simulation of Titan's interaction with the supersonic solar wind during Cassini's T96 flyby, *Geophys. Res. Lett.*, 43, 35-42, <http://dx.doi:10.1002/2015GL066848>

Liuzzo, L., **Feyerabend, M.**, Simon, S., Motschmann, U., 2015, The impact of Callisto's atmosphere on its plasma interaction with the Jovian magnetosphere, *J. Geophys. Res.*, 120, 9401-9427

Regoli, L., Roussos, E., **Feyerabend, M.**, Jones, G., Krupp, N., Coates, A., Simon, S., Motschmann, U., Dougherty, M., 2015, Access of energetic particles to titan's exobase: A study of cassini's T9 flyby, *Planet. Space Sci.*, pp. -, ISSN 0032-0633